Laser-Induced Thermal Acoustic Velocimetry

Thesis by

Stefan Schlamp

In Partial Fulfillment of the Requirements

for the Degree of

Doctor of Philosophy

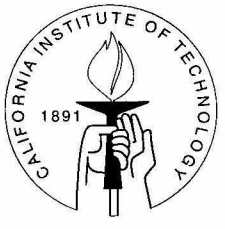

California Institute of Technology

Pasadena, California

2000

(Submitted May 17, 2000)

Acknowledgements

My deepest gratitude goes to my advisor, Prof. Hans G. Hornung, for his support, friendship and encouragement throughout the past five years. He gave me a lot of leeway to follow my academic and scientific interests but at the same time provided help, guidance, and advice when needed.

Eric B. Cummings taught me everything on LITA I know today. I was very fortunate to have him as my mentor. He provided me with ideas, guidance, and assistance. During a single day of working together with Eric I learned more than during weeks of self-study.

Thomas H. Sobota from Advanced Projects Research, Inc., is the third key-player during my time at Caltech. Discussions with him gave me insight into the engineering aspects and practical considerations of my work. Having him as a source of motivation proved pivotal in times when nothing seemed to work.

Thanks also go out to all the people who made my stay possible and an enjoyable time: my wife Andrea, my parents, the students, staff, and faculty of GACLIT, and the entire Caltech community. Caltech provided a perfect environment for fostering creativity.

Eunice Allen-Bradley and Emanuele Camera both spent a summer at Caltech working together with me as part of the SURF program which was supported by the office for Student-Faculty Programs. Sam Roweis and Eric Winfree as teaching assistants provided me with the knowledge, understanding, and source code of artificial neural networks.

This research was funded by the NASA Langley Research Center under NASA contract NAS1-99016 and by the United States Air Force Research Laboratory at Edwards Air Force Base.

Abstract

Laser-Induced Thermal Acoustics (LITA) is a non-intrusive, remote, four-wave mixing laser diagnostic technique for measurements of the speed of sound and of the thermal diffusivity in gases. If the gas composition is known, then its temperature and density can be inferred.

Beam misalignments and bulk fluid velocities can influence the time history and intensity of LITA signals. A closed-form analytic expression for LITA signals incorporating these effects is derived. The magnitude of beam misalignment and the flow velocity can be inferred from the signal shape using a least-squares fit of this model to the experimental data. High-speed velocimetry using homodyne detection is demonstrated with NO_2-seeded air in a supersonic blow-down nozzle. The measured speed of sound deviates less than 2% from the theoretical value assuming isentropic quasi-1D flow. Boundary layer effects degrade the velocity measurements to errors of 20%. Heterodyne detection is used for low-speed velocimetry up to Mach number $M = 0.1$. The uncertainty of the velocity measurements was ~ 0.2 m/s. The sound speed measurements were repeatable to 0.5%. The agreement between theory and experiments is very good.

A one-hidden-layer feed-forward neural network is trained using back-propagation learning and a steepest descent learning rule to extract the speed of sound and flow velocity from a heterodyne LITA signal. The effect of the network size on the performance is demonstrated. The accuracy is determined with a second set of LITA signals that were not used during the training phase. The accuracy is found to be better than that of a conventional frequency decomposition technique while being computationally as efficient. This data analysis method is robust with respect to noise, numerically stable, and fast enough for real-time data analysis.

The accuracy and uncertainty of non-resonant LITA measurements is investigated. The error in measurements of the speed of sound and of the thermal diffusivity initially decreases with increasing signal intensity (excitation beam pulse energy) and increases again after passing a minimum. The location of the minimum error for the speed of sound and for the thermal diffusivity coincide. The errors at the minimum are 0.03% and 1%, respectively. The uncertainties for the speed of sound and the thermal diffusivity decrease monotonically to 0.25% and 5%, respectively. The increased error for high excitation beam pulse energies results from finite-strength waves that cannot be treated using the linearized equations of motion.

Contents

List of Figures

Nomenclature

English Symbols

A	relative intensity of reference beam, see Eqn. 5.2b
$A_{\{P,T,D\}}$	amplitude of acoustic waves, thermal grating and finite-driving-time terms respectively, defined by Eqn. 2.15
c_s	speed of sound
D	$= A_D \Sigma_D$
D_S	diffusivity of excited-state target molecules through fluid
D_T	thermal diffusivity
D_V	longitudinal kinematic diffusivity of fluid $(1/\rho(\nu_v + (4/3)\nu_s))$
$\hat{e}$	unit vector in direction of laser beam
E	error measure, defined by Eqn. 5.10
E	electric field vector
E_d	energy per driver laser pulse
f	frequency or focal length
G	acoustic damping per cycle
h	number of units in hidden layer of neural network
H_θ, H_e	defined by Eqn. 2.6a and 2.6b respectively
H_{eP}, H_{eT}	defined by Eqn. 2.6d
i	$= \sqrt{-1}$
I	normalized spatial electric field distribution
k_d	wave vector magnitude of driver lasers
$\mathcal{L}$	detected LITA signal intensity
m	number of units in output layer of neural network
M	Mach number

$\mathcal{M}$	molar mass
n	number of units in input layer of neural network
N	number of signals in training and validation sets
$N_{\{P,T,D\}}$	defined by Eqn. 2.14b
$P_{1,2}$	$= A_{P1,2}\Sigma_{P1,2}$
$P(t)$	normalized time history of laser beam field amplitudes
$\vec{q}, q, q_x, q_y, q_z$	spatial Fourier transform vector, magnitude, Cartesian components
q_ψ	grating/phase-matched scattering vector
$\vec{r}, x, y, z$	position vector, Cartesian components
$\vec{r}_1, \vec{r}_2$	misalignment of driver beams
$\vec{R}, R$	position vector of detector element, magnitude
$\mathcal{R}$	universal gas constant
SNR	signal-to-noise ratio with respect to peak signal intensity
t	time
T	$= A_T\Sigma_T$
T_t	total or reservoir temperature
$\vec{u}, u, v, w$	fluid velocity vector, Cartesian components
u_y	velocity component in y-direction (same as v)
$\mathcal{U}_e, \mathcal{U}_\theta$	electrostrictive and thermal grating parameter
v_{kj}	connection weight from hidden unit j to output unit k
w_{ji}	conncetion weight from input unit i to hidden unit j
x_i	output of input unit i
X, Y, Z	length scales defined by Eqn. 2.3b
y_k	output of output unit k
z_j	output of hidden unit j

Greek Symbols

γ	ratio of specific heats
$\gamma_{n\theta}$	rate of excited-state energy decay not caused by thermalization
γ_θ	rate of excited-state energy decay caused by thermalization
Γ	acoustic damping rate, $\Gamma = [(\gamma - 1)D_T + D_V]/2$
Δ	thermal grating damping over a period of acoustic motion
$\mathcal{E}$	slowly varying electric field envelope
ζ, $\overline{\zeta}$	misalignment length scales, defined by Eqn. 2.3b
η, $\overline{\eta}$	misalignment length scales, defined by Eqn. 2.3b
η_k	target value for output unit k
η_s	shear viscosity
η_v	bulk viscosity
2θ	driver beam crossing angle
λ	wavelength
$\vec{\mu}, \mu$	dipole density vector, magnitude
μ_i	threshold for unit i, defined in Eqn. 1.1
ξ, $\overline{\xi}$	misalignment length scales, defined by Eqn. 2.3b
Π	ratio of acoustic wave frequency to thermalization rate
ρ	mass density
σ	Gaussian half-width of source laser
$\sigma(\cdot)$	activation function, defined in Eqn. 5.9
σ_c	uncertainty of sound speed measurement
σ_D	uncertainty of thermal diffusivity measurement
σ_y, σ_z	length scales defined by Eqn. 5.3f
$\Sigma_{\{P,T,D\}}$	defined by Eqn. 2.14d
τ	fitting parameter for exact time of driver laser pulse
ϕ	angular misalignment, angle of driver beams with x-y-plane, see Fig. 2.1

$\tilde{\phi}$	random phase shift between Doppler and Brillouin frequencies
$\Phi_{P,T,D}$	defined by Eqn. 2.6c
$\Phi^{(d)}_{P,T,D}$	defined by Eqn. 2.9a-c
$\Phi^{(d,0)}_{P,T,D}$	defined by Eqn. 2.14a
χ	dielectric susceptibility
ψ	angle of source laser to x-z-plane, see Fig. 2.1
$\Psi_{\{P,T,D\}}$	defined by Eqn. 2.14c
ω	Gaussian half-width of driver beams

Superscripts

(d)	including driver beam spatial effects
(0)	including source beam spatial effects
$(\cdot)\prime$	small perturbation
μ	training/validation signal μ

Subscripts

D	related to the creation of the thermal grating
P	related to first acoustic wave
P^*	related to second acoustic wave
T	related to the thermal grating
d	related to the driver beams
e	related to electrostriction
het	related to heterodyne detection
hom	related to homodyne detection
$n\theta$	not related to thermalization
ref	related to reference beam
0	related to the source beam
s	related to the signal beam

θ	related to thermalization
i	related to input unit number i
j	related to hidden unit j
k	related to output unit k

Miscellaneous Symbols

$\mathcal{FT}(\cdot)$	Fourier transform
$H(\cdot)$	Heaviside step function
$\Re(\cdot)$	Real part of complex number
$\mathcal{O}(\cdot)$	Order of magnitude
$(\cdot)^*$	complex conjugate
$\otimes$	vector cross product
$\vec{x} \cdot \vec{y}$	dot product
$f(t) \circ g(t)$	Laplace convolution, *i.e.*, $\int_0^\infty f(\tau)g(t-\tau)d\tau$
$\propto$, $\sim$	proportional to, scales like

Chapter 1

Introduction

1.1 Motivation

The original idea in the development of Laser-Induced Thermal Acoustics (LITA) was to use it as a flow diagnostic tool for Caltech's T5 hypervelocity shock tunnel.[1] Test times in this facility are approximately 2 ms and some flow regions reach temperatures up to 10,000 K. High levels of luminosity are present in these regions as well as particulates from various sources. Turnaround times between experiments are 2 hours and the costs of operating and maintaining this facility are substantial. Current data collection uses shadowgraphs and Schlieren images for qualitative flow visualization, holographic interferograms for quantitative measurements of the density field, and surface-mounted pressure and temperature transducers for quantitative measurements. Hence, at present, quantitative thermal measurements are limited to the surface of the test body. A non-intrusive technique for the outer flow is very desirable. The aggressive flow environment, slow turnaround and high costs, however, make T5 unsuitable for technique developments. Hence, a special rig was built to develop and test LITA.

This thesis looks at two points of possible improvement of LITA, namely the user-friendliness and the amount of data that can be extracted per laser-shot. For other, more common laser diagnostic techniques such as Particle Image Velocimetry (PIV) and Laser Doppler Velocimetry/Anemometry (LDV/LDA), there are commercial turn-key systems available that are aligned and calibrated by the manufacturer. To reach a similar point of sophistication with Laser-Induced Thermal Acoustics, we

require a system that is capable of autonomous alignment and is adaptable to a wide range of applications. The data analysis has to be fast, robust and be an integral component of the system. As for the yield of data per LITA measurement, Cummings[2] already proposes the use of LITA for velocimetry. A proper theoretical treatment of this proposition, and its experimental confirmation, can allow simultaneous measurements of the speed of sound and the flow velocity.

1.2 Background on Laser-Diagnostic Techniques

The development of powerful lasers has enabled a variety of flow measurements such as concentration, temperature, flow velocity, or combinations thereof. Some of these are point-measurements, others can be applied along lines, grids, in a plane or in a three-dimensional sample volume. Velocimetry techniques differ by how many velocity components are measured simultaneously, by their time-resolution, and by the time it takes to take a measurement. Another important aspect are their signal levels. Typically, nonlinear optical techniques provide stronger signals, making short measurement times in hostile environments possible (see Section 1.1). Their disadvantage is the complexity of the data analysis, for which linear techniques are easier to analyze. In the next paragraphs Laser-Induced Thermal Acoustics is compared to these techniques and its advantages and disadvantages are noted. The following list is not complete. For some widely used techniques, attention is restricted to super- and hypersonic flows, and to combustion where luminosity and particles are of importance.

- In planar **Laser-Induced Fluorescence** (PLIF) one uses a laser sheet to excite certain species in a flow and to look at their fluorescence either immediately or at later times. The intensity of the fluorescence is a function of the local species concentration and temperature. To achieve quantitative results one must model a large number of these molecular energy transfer processes correctly. Typically, O_2, OH and NO are used as fluorescing molecules which makes this technique

very useful for flows where these species occur naturally such as in combustions[3] or in shock tunnels.[4] In its pure form only species concentrations are measured. These can then be compared to CFD simulations,[4] and to measurements with other flow diagnostic techniques.[5] The molecular energy transfer rates also depend on the excitation wavelength and the temperature. Hence, by scanning through a variety of excitation laser frequencies, *i.e.*, by a spectroscopic application, one can use PLIF for thermometry.[6] By applying image correlation techniques,[7] velocity measurements might become feasible in the near future. This technique has been used successfully in T3 at the Australian National University.[6] T3 is a predecessor of T5 which suggests the applicability to T5. But due to luminosity, the previous experiments were limited to flow enthalpies of less than 4.1 MJ/kg. This value represents the lowest achievable flow enthalpy in T5 where values reach as high as 32 MJ/kg for some test conditions. Fluorescence is an incoherent phenomenon. This means that the fluorescent light is radiated equally in all spatial directions. Hence, only part of the total emitted light fall on the detector. Furthermore, this makes spatial filtering impossible. Luminosity thus poses a significant challenge for this technique, as it does for other linear laser-diagnostics (see below).

- Miles *et al.*[8] use **Flow tagging** in sonic air jets. A UV laser transforms the air's oxygen into ozone along its path. At later times, the convection and deformation of the line can be detected by laser induced fluorescence (LIF). Diffusion can be neglected for many instances. This provides velocity information during the lifetime of the ozone for particles that were located on the tagged line by comparing two subsequent LIF images. The time resolution is only limited by the time separation between two images. Instead of the O_2/O_3 reaction, hydroxyl (OH) radicals can be created by photo-dissociation of vibrationally excited H_2O molecules.[9] Also, NO_2 (seeded[10] or as combustion product[11]) can be reduced to NO. A stereoscopic camera setup measures all three velocity

components.[11] Recent experiments in supersonic flows[12] and in shock tubes[13] use excimer lasers to ionize sodium atoms, and look for a depletion of sodium in the read-out phase. Due to dissociation, seeding with H_2O or NO_2 is not possible in T5. Sodium seeding, however, has been demonstrated.[14] The laser pulse energy dictates if one can create multiple lines or a grid of lines. Multiple velocity components can be measured for tagged lines in a grid pattern. At high flow enthalpies in T5, the lifetime of the tagging species will not be sufficient. LIF constitutes the read-out phase and all limitations of LIF apply for flow tagging.

- For **Particle Image Velocimetry** (PIV), the flow is seeded with solid, neutrally-buoyant particles which are are a few μm in diameter. Light from a laser sheet is scattered by the particles, making them visible on a camera system. The comparison of two subsequent pictures yields the displacement vector of each particle and thus the velocity vector. PIV is predominantly applied to low-speed flows, but some authors use PIV in supersonic flows[15,16] and with a stereoscopic setup,[17] yielding three velocity components. PIV requires a suitable particle density in the flow field. Artificial seeding in T5 has to be excluded due to the high flow temperatures and the difficulty of achieving uniform particle number densities. In high-speed compressible flows the assumption that the particles follow the flow breaks down. PIV yields in-plane velocity components for particles illuminated by the laser sheets. The time delay between pictures is chosen according to the flow velocities and the camera resolution. For the study of hypersonic boundary layers, the wide range of flow velocities poses a challenge, as does luminosity. Due to out-of-plane velocity components, some particles that are present in the first picture are not visible in the second picture, and *vice versa*. This complicates the pairing of corresponding particle images on the two pictures and introduces erroneous velocity vector. Data processing is too slow for real-time applications.

- A dipole moment is induced into molecules if they are excited by light. With a small likelihood, the oscillating dipole will re-radiate light at the excitation frequency (plus a Doppler shift). This effect is called **Rayleigh scattering**. The intensity of the scattered light from a collection of molecules is proportional to their number (*i.e.*, density) and their scattering cross section. The scattering cross section is small for all "simple" molecules and, as a result, the signal levels are low. Filtered Rayleigh scattering employs a tunable, narrow-band excitation laser and a notch filter in front of the detector. It measures flow velocities over a wide field of view.[18,19] Alternatively, using a Fabry-Perot etalon in front of the detector allows simultaneous velocity and temperature measurements at a single point.[20,21]

  Rayleigh scattering is an incoherent scattering phenomena which makes it very susceptible to luminosity. The scattering frequency is identical to the excitation frequency which makes it subject to interference with light from the excitation light source (*e.g.*, off windows, particles, *etc.*). Rayleigh scattering is related to LIF. For LIF, however, the excitation laser frequency is chosen to be in resonance with the absorption lines of the target molecules. Rayleigh scattering shows the same limitations as LIF but its signal levels are even lower than in LIF.

- **Coherent Anti-Stokes Raman Scattering** (CARS): Raman scattering is similar to Rayleigh scattering except that the re-radiated photons have a different wavelength than the excitation photon. The energy difference between the absorbed and emitted photon is equal to the energy difference of the vibrational quantum which depends on the species and the rotational temperature. The spectrum of the Raman scattered light hence contains information on species concentrations and the rotational temperature which, in most applications, is close to the static temperature. Wavelength above and below the excitation

wavelengths are refered to as Stokes and anti-Stokes Raman scattering. Raman scattering is a linear technique and two to three orders of magnitude weaker than Rayleigh scattering.

For coherent anti-Stokes Raman scattering (CARS) two pulsed excitation beams are used. One is at a fixed wavelength, the second is tunable and at a slightly lower frequency than the first laser. Both laser beams are focussed collinearly on the point of interest. If the frequency difference between the two laser beams is equal to the vibration frequency of the species at the focus, the vibrations of the molecules are driven coherently, thus generating a coherent phase grating in the gas that scatters the excitation beams into two collinear and coherent signal beams, the Stokes and the anti-Stokes branch. The latter is preferred in experiments.[22] The intensity of the scattered beam from this nonlinear technique is proportional to the square of the species concentration. As with incoherent Raman scattering, the rotational temperature can be obtained from the spectrum of the scattered beams. CARS combines the advantages of the species selectivity of Raman scattering with strong signals typical for nonlinear (coherent) techniques. Scanning of the laser wavelength is necessary, but single-shot measurements are required in shock tunnels. Multiplex CARS avoids the necessity of scanning by using a broadband excitation laser, which decreases the sensitivity significantly.[23] Dual-line CARS combines the single-shot feature of multiplex CARS with the sensitivity of CARS.[24] Applications to supersonic, hypersonic and chemically reacting flows have been demonstrated (*e.g.*, Anderson *et al.*[25]).

- A particle's motion through a fringe pattern, created by a pair of crossed laser beams, is observed in **Laser Doppler Velocimetry** (LDV). The light scattered by particles crossing the fringe spacing is modulated at the Doppler frequency. Commercial systems for this point-measurement technique are widely available.

The fringe pattern only illuminates the particles crossing it. It does not create a response in the fluid as is the case for LITA. The required laser power is thus low. Compact and affordable laser diodes are used resulting in small system size and good mobility.[26] Several approaches exist to measure multiple velocity components. Using two perpendicular fringe patterns with different wavelength is one. Alternately pulsing lasers[27] avoid the need for multiple photodetectors and data acquisition chains, and lasers of the same wavelength can be used. LDV depends on a suitable particle number density in the flow. The concentration has to be such that one particle is passing through the fringe pattern at any time. The requirement of seeding and the susceptibility to luminosity limit the applications of PIV.

Of the techniques discussed above, only CARS shows promise for high-enthalpy shock tube applications. While it allows the measurement of species concentrations and temperatures, it does not yield velocity information and it requires substantial data analysis. Laser-Induced Thermal Acoustics (see Section 1.3) can complement CARS with velocimetry data.

1.3 Introduction to Laser-Induced Thermal Acoustics

The creation of a LITA signal involves two steps: opto-acoustic forcing, and acousto-optical scattering. In the first step, a powerful, pulsed laser beam is split into two phase-coherent halves which intersect at a shallow angle in the test fluid (Fig. 1.1). Interference results in an electric field intensity grating.

Two effects dominate the fluid's response to the electric field grating: thermalization and electrostriction. Thermalization refers to energy absorption by means of inelastic intermolecular collisions. The temperature increases in regions with high

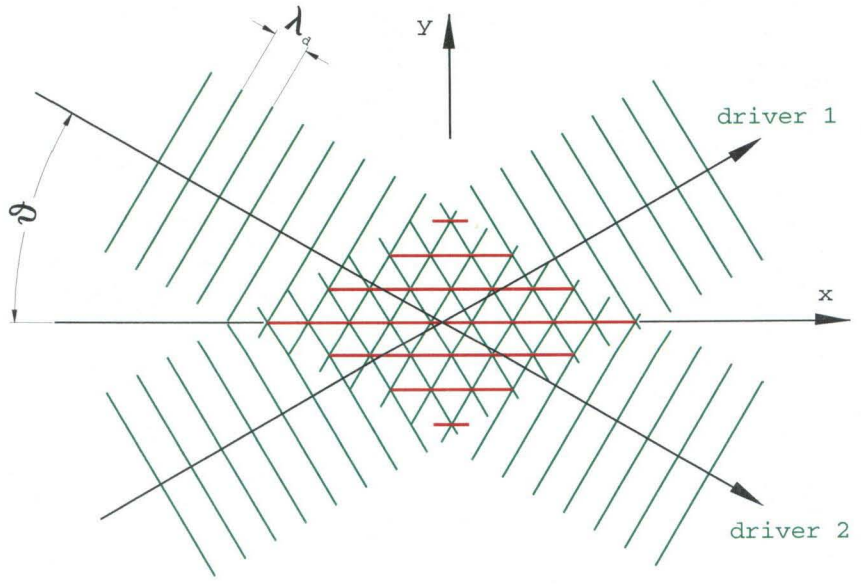

Figure 1.1: Two driver laser beams of wavelength λ_d intersect at angle θ. In the intersection region, they create an interference grating with fringe spacing $q_\psi = \lambda_d / \sin\theta$.

electric field intensity but remains unchanged elsewhere. The temperature fluctuations are $\mathcal{O}(0.1\text{ K})$. The temperature increase is almost instantaneous compared to other LITA time scales. Fig. 1.2 shows the creation of the temperature grating schematically. The fluid expands with increasing temperature, and if the expansion speed is comparable to the sound speed, sound waves are generated. The effect of polarizable molecules which are accelerated in the direction of electric field gradients is refered to as electrostriction. It induces a velocity grating into the fluid. Mathematically, thermalization represents a forcing term in the energy equation while electrostriction is a forcing term in the momentum equation.

Due to the short duration of the laser pulse ($\mathcal{O}(10\text{ ns})$), there cannot be a density grating at $t = 0^+$ for either mechanism. Acoustic waves are generated that cancel the steady-state solution at $t = 0$. Fig. 1.3 shows the decomposition of the density fields for the cases of thermalization (left) and electrostriction (right). The evolution of the density grating is observed in the second step, the acousto-optical scattering. A third, continuous laser beam (interrogation beam) is directed at the Bragg angle onto

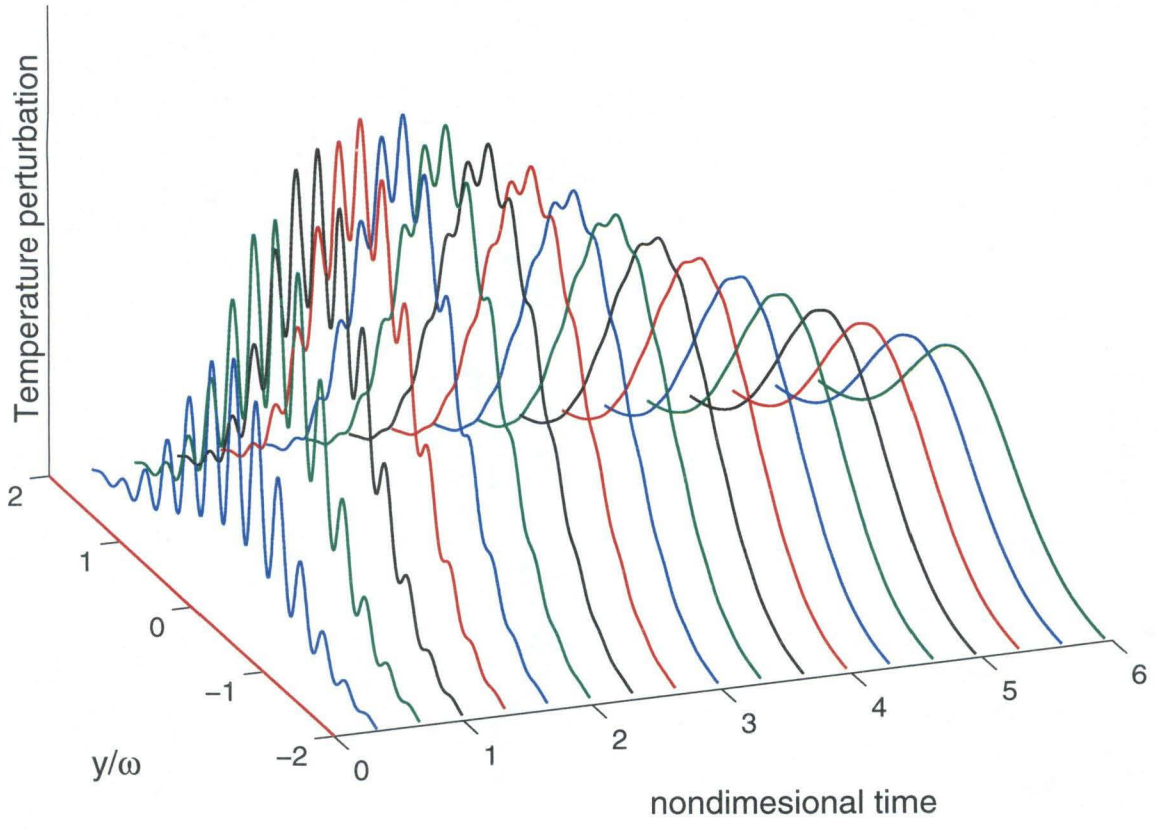

Figure 1.2: Creation of temperature grating by pulsed driver beams at $t = 0$ assuming finite-rate thermalization. The creation in early times is governed by the finite thermalization rate. Thermal diffusion governs behavior at later times. After Eichler *et al.*[28]

the grating (Fig. 1.4). The index of refraction is a function of the density. Hence, the grating acts like a diffraction grating and scatters a small fraction (typically $\approx 0.01\%$) of the interrogation beam coherently into a signal beam. The instantaneous intensity of the signal beam depends on the modulation depths of the density grating. Due to constructive and destructive interference of the acoustic waves with each other as well as with the thermal grating (for the case of thermalization), the signal will be modulated at the Brillouin frequency.

The time history of the signal beam is recorded using one of two techniques. Homodyne detection measures the intensity history of the signal beam. Fig. B.1

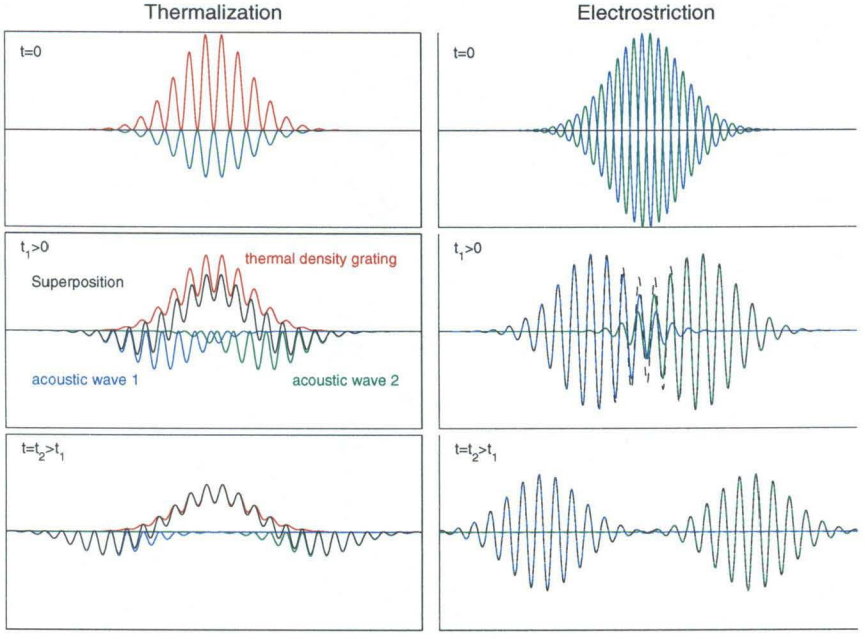

Figure 1.3: Decomposition of density gratings for thermalization (left) and electrostriction (right) along a cross section of the grating. For the case of thermalization, two identical acoustic waves cancel the thermal density grating initially. At $t > 0$ they travel at the local speed of sound in opposite directions. They decay at the acoustic damping rate. Meanwhile, the stationary thermal grating decays due to the effects of diffusion. In the case of electrostriction, two acoustic waves of opposite sign are created at $t = 0$, which travel in opposite directions at later times.

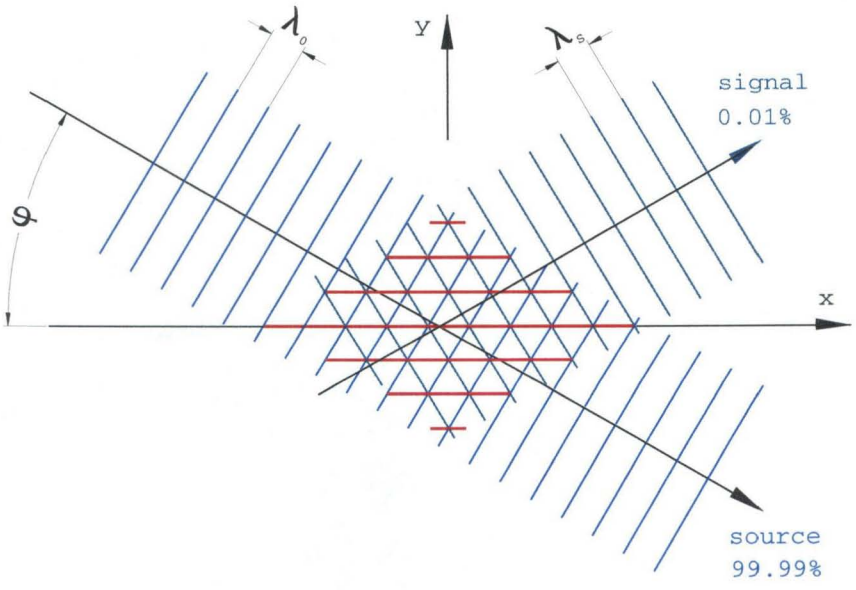

Figure 1.4: The source beam (wave length λ_0) incident at the Bragg angle ψ is scattered into a coherent signal beam by the density grating. The signal beam will be Doppler-shifted if the grating is convected in the y-direction.

gives an example of a typical LITA signal obtained with homodyne detection. The speed of sound is encoded as the Brillouin frequency (oscillations in the early part of the signal). The Brillouin frequency is equal to the speed of sound divided by the fringe spacing. Thermal diffusion governs the signal decay. The profiles at late times in Fig. 1.2 depict the diffusive decay of the thermal grating after the acoustic waves have traveled out of the region of interest.

Heterodyne detection records the superposition of the signal beam with a reference beam. The signal beam frequency is Doppler-shifted if the density grating is convecting in a direction along the grating normal vector. By mixing the signal beam with a reference beam at the interrogation laser frequency, the Doppler shift becomes visible in the recorded trace. Fig. 5.2 is an example for a LITA signal recorded using heterodyne detection. Again, the Brillouin frequency and the signal decay are governed by the speed of sound and by thermal diffusion, respectively. The low frequency component is the Doppler shift which is proportional to the flow velocity. The ratio of the Doppler frequency to the Brillouin frequency is the local Mach number.

If only the speed of sound and the flow velocity are to be measured, a frequency decomposition technique can be used for data analysis. To also find the thermal diffusivity (and the flow velocity using homodyne detection, see Chapter 3), a fitting technique has to be employed. A theoretical model is fitted to the experimental data where the speed of sound, thermal diffusivity, and flow velocity are fitting parameters. Cummings *et al.*[29] derived such a model which is generalized in Chapters 2 and 5. Frequency decomposition methods are fast ($\mathcal{O}(0.01$ s) per signal) compared with the fitting routine ($\mathcal{O}(1$ s) per signal).* The fitting method requires good initial guesses for the algorithm to converge to the correct solution. A new approach for LITA data analysis is introduced in Chapter 5, using artificial neural networks. This technique combines the accuracy and generality of the fitting technique with the speed and robustness of the frequency decomposition techniques (see Section 1.4).

LITA is highly accurate ($\mathcal{O}(0.01\%)$ error for the speed of sound, $\mathcal{O}(1\%)$ for the thermal diffusivity, and $\mathcal{O}(0.5\%)$ for the flow velocity). Its applications so far have been limited to high-accuracy static measurements and to thermometry in flames. Each LITA measurement takes $\mathcal{O}(1\ \mu$s) which makes LITA suitable for high-speed applications. Spatial and frequency filtering removes ambient incoherent luminosity originating from the coherent signal beam. This and the short test time make LITA applicable to T5.

1.4 Introduction to Neural Networks

Current methods for analyzing LITA signals require user input and expertise. This is unacceptable for packaged LITA systems. In Chapter 5 a neural network (NNs) is trained to perform the data analysis. This section gives an introduction to the background and concepts of neural networks. The theoretical treatment in Section 5.3 is more detailed and mathematically more rigorous.

c.f. typical Nd:YAG laser repetition rates of 10 Hz

The human brain contains approx. 10^{11} nerve cells (neurons).[†] Each neuron receives inputs through a tree-like network of nerve fiber (dendrites) and passes its output through a single long nerve fiber, called axon. The axon branches out and connects to approx. 1,000 other neurons by forming junctions (synapses) with their dendrites or the cell body directly. Each input has the effect of raising or lowering the electrical potential of the neuron relative to its surrounding through complex chemical processes. If the potential increases beyond a threshold, a pulse-like signal, called action potential, is produced which travels along the axon, changing the potential in the connected neurons. The amplitude of the action potential is fixed, *i.e.*, not a function of the inputs. The lower limit for the time between action potentials is approx. 1 ms which corresponds to a "clock speed" of the brain at less than 1,000 Hz.[‡] The computational power of a single neuron is very small, but their number and their connectivity make the brain superior in some tasks to the fastest computers.

Driven by the desire to understand how data is processed and stored in the human brain, the field of neural computation goes back to a paper by McCulloch and Pitts in 1943.[30] It introduces a simple circuit of idealized "brain cells," not unlike the neural network being used in Chapter 5. The output of each computational neuron, which is called call "unit" to distinguish it from the biological term, is unity if the weighted sum of all its inputs is greater than a certain threshold and zero otherwise, *i.e.*,

$$y_i = H\left(\sum_j w_{ij}x_j - \mu_i\right), \tag{1.1}$$

where y_i is the output of the neuron i, H is the Heaviside step function, w_{ij} is the weight between unit j and unit i and μ_i is the threshold of this unit. The biological analog to the weights is the strength of a synapse. The weights can be positive or negative just as synapses can be excitatory or inhibitory, *i.e.*, they can raise or lower the cell's potential. Minsky[31] showed that a circuit of these simple units is capable of

[†] *c.f.* $2.8 \cdot 10^7$ for Intel Pentium III processor, $7.5 \cdot 10^6$ for Intel Pentium II processor.

[‡] *c.f.* hundreds of MHz for computer processors.

universal computation. Units with other properties as in Eqn. 1.1 are used today, each with its advantages and disadvantages. One can use linear and nonlinear, continuous-valued or probabilistic units where the Heaviside step function in Eqn. 1.1 is replaced by a probability density function.

A few standard architectures, however, have crystallized. *E.g.*, the so-called Hopfield network where every unit is connected to every other unit can be used for image storage and recollection, and simple implementations to solve the traveling salesman and similar problems exist.[§] The most popular standardized circuit architecture is the feed-forward neural network where units are arranged in layers (Fig. 5.1). Each unit passes information only to units in the next higher layer. These kind of networks can be "trained" to learn tasks such as data compression by means of principal component analysis (PCA) and function approximation/curve fitting. This latter application is utilized for the LITA data analysis.

All feed-forward networks have at least one input layer and one output layer. In Chapter 5 a LITA signal is used as input for the units in the input layer and the units in the output layer represent the speed of sound and the flow velocity. Between the input and the output layer there can be additional layers (hidden layers). It can be shown that with one hidden layer, any continuous function on a bounded domain can be approximated to arbitrary accuracy given a sufficient number of units in the hidden layer.[¶] The question of what the term "sufficient" means is discussed in more detail in Chapter 5. With the theoretical results derived in Chapters 2 and 4 we conclude that a continuous function exists between the inputs and the outputs.

The training algorithm back-propagation was invented several times independently.[32–35] It requires that a training set is available, *i.e.*, a number of example inputs where the desired output is known. For this training set, an error measure can be defined which is zero if and only if the actual network outputs are equal to

[§]But not more efficient than other algorithms for this NP-complete problem.

[¶]Similarly, it can be shown that with two hidden layers any function can be approximated to arbitrary accuracy given a sufficient number of units in each of the two hidden layers.

the desired outputs. Since the network outputs can be expressed in terms of the weights and the input values, the error measure can also be expressed in terms of these parameters. By simple differentiation of the error measure w.r.t. the weights, the weights can be updated as to minimize the error measure iteratively. The details are given in Chapter 5. This iterative scheme constitutes the training as the error decreases continuously. The name back-propagation comes from the fact that first the weights between the output layer and the last hidden layer are updated, then the weights between the two preceding layers, *etc.* The convergence behavior of the training depends on a the numerical minimization routine and the number of hidden units. Two kinds of errors are observed: bias and variance. Bias is the error that is due to the network architecture, in particular to an insufficient number of hidden units. Variance is the error that is due to the fact that the training set does not cover the entire parameter space evenly or densely enough.

Theoretically, one could use a large number of hidden units to minimize the bias. But this increases the computational cost which scales approximately linearly with the number of hidden units. More importantly, for a fixed number of samples in the training set, an effect called over-training is observed. The reason for over-training is that the network has enough degrees of freedom to "memorize" the entire training set. This can be compared with fitting data by a polynomial with too many degrees of freedom. *E.g.*, if the number of degrees of freedom is equal to the number of data points, the function will pass exactly through all data points. But if we obtain an additional data point, it will most likely be far off the fitted curve. In the context of neural networks, this is refered to as poor generalization. A solution is to increase the size of the training set, but this adds again to the computational cost. In Chapter 5, a different approach is taken in addition to limiting the number of hidden units to a small value.

Feed-forward neural networks are compelling for several reasons

- Once trained, they are computationally very efficient and stable.

- They lend themselves to hardware implementations for parallel processing (neural network VLSI chips).

- Neural networks are capable of generalization. This means from a finite sample out of an infinite number of possible input-output combinations, they can interpolate and extrapolate the correct solution for inputs they were not trained on.

1.5 Outline

Chapters 2-5 and Appendix B represent conference papers and published or submitted papers. They are included mostly unchanged from their published (or submitted) version. If additional results have been obtained since their submission, however, they are added. Furthermore, some explanations and comments are more detailed than in the published versions where space is very limited and color reproduction is not possible. Each of these chapters is self-contained. Unfortunately this also results in some overlap in the material in different chapters. A comprehensive bibliography at the end of this thesis replaces the individual bibliographies for each chapter.

Chapter 2[36] lays the theoretical foundations for Chapters 3 and 4. It includes the effect of beam misalignments and bulk fluid velocities to the LITA theory, originally derived by Cummings,[2] and verifies some of the results experimentally. Chapter 3[37] tries to verify some more theoretical results from Chapter 2 experimentally. Where previous experiments examined different kinds and degrees of beam misalignment, we investigate utilizing beam misalignments for velocity measurements. Chapter 4[38] generalizes the model further by allowing for different detection methods: homodyne detection and heterodyne detection. Due to length constraints, the theoretical derivation on which the work is based is not given. Instead, the derivation is part of Chapter 5. Chapter 5[39] introduces the concept of neural networks and presents a neural network implementation to perform the data analysis on LITA signals. Section

7.2 represents ongoing work on multi-point LITA measurements and results will be presented in Schlamp *et al.*[40] Chapter 6 summarizes the main results. Finally, Chapter 7 gives some starting points for further improvements and shows the next steps towards making LITA a usable system for T5. Appendix B[41] demonstrates aspects regarding the accuracy of LITA experimentally.

Chapter 2
Beam Misalignments and Fluid Velocities in Laser-Induced Thermal Acoustics (LITA)

2.1 Introduction

The four-wave mixing technique laser-induced thermal acoustics (LITA) is used in various laboratories to measure the sound speed and thermal diffusivity[42–44] as well as fluid velocities.[45] A grating-shaped pressure and temperature perturbation is created in a fluid by two coherent intersecting pulsed laser beams. These perturbations evolve hydrodynamically in time and space. This evolution can be examined by focusing a third continuous laser beam on the associated density gratings at its Bragg angle. Depending on the modulation depth of the density grating, a fraction of this source beam is coherently scattered into a weak signal beam. The induced acoustic waves move outwards, modulating the density field and hence the signal at the grating Brillouin frequency, or the frequency of sound waves with the grating wavelength. Hence, one approach to measure the sound speed is to measure the frequency of the signal modulation by means of a frequency decomposition method. However, finite signal lifetime and sampling resolution limits the accuracy of this technique.

Another approach is to model the physics of the interactions that produce the LITA signal and derive an analytic expression for the signal as a function of experimental parameters, fluid properties including the sound speed and thermal diffusivity, and fluid velocity. A least-squares fit of this expression to experimental signals

then provides best estimates of the signal parameters and hence fluid properties. Cummings *et al.*[29] derived such an expression that includes thermalization and electrostriction as the two main mechanisms for the creation of the grating. However, the assumption was made that the system was in perfect optical alignment and that the fluid was at rest. Obviously this approach breaks down when these assumptions are grossly violated. In these cases, the theory is not a valid representation of the experiment and the fitting procedure returns erroneous values.

The work presented here extends the earlier theory to include the effects of a convection velocity and finite beam misalignment. These may then be measured through the least-squares fitting procedure, simplifying LITA velocimetry. Present velocimetry techniques using LITA rely on the measurement of a small Doppler shift of the signal beam using heterodyne detection. Now, only from the recorded signal and using the simpler homodyne detection, sound speed, velocities and transport properties of the fluid can be extracted simultaneously. In addition we can extract beam misalignment measurements from the signal and either realign the optics with this information or take them into account in the data analysis.

In Sections 2.2-2.6 we extend the LITA analysis of Cummings *et al.*[29] using nomenclature mostly adapted from that derivation. First, the grating creation due to the opto-acoustic forcing is modeled. The functional form of the electric field grating in the sample volume is derived. Next, the fluid response to the electric field is examined. Since the underlying physics have not changed, the fluid response to electric fields has been left unchanged from Cummings *et al.*,[29] only the results are given, and the interested reader is referred to there and to Eichler *et al.*[28] Finally, the scattering of the source beam into the signal beam is modeled using the linearized equation of light scattering. In Sections 2.7-2.9, experimental results are presented that validate the theory.

2.2 Frame of Reference

We define our frame of reference so that the origin of our fixed Cartesian coordinate system is at the focus of the source beam as shown in Fig. 2.1. The source beam lies in the $x-y$-plane and forms an angle ψ with the x-axis. The $x-z$-plane bisects the two driver beams so that each one intersects this plane at an angle θ. They intersect the $x-y$-plane at angles ϕ_1 and ϕ_2 (angular misalignment). Their foci are at $\vec{r}_1$ and $\vec{r}_2$, respectively (spatial misalignment). We denote the time of the short driver pulse as $t = 0$. A perfectly aligned LITA setup would have $\vec{r}_1 = \vec{r}_2 = \phi_1 = \phi_2 = 0$ but *not* $\theta = 0$.

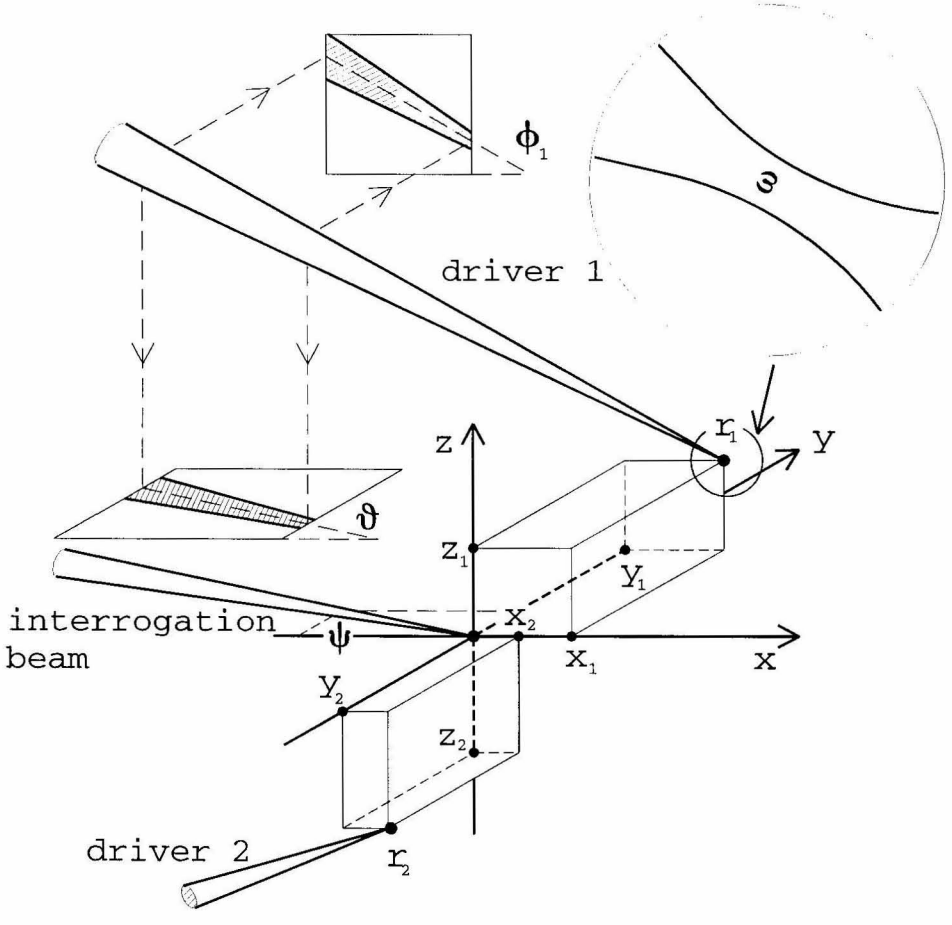

Figure 2.1: Frame of reference for LITA analysis. The beams' diameters at their foci are ω and σ for the driver beams and interrogation beam, respectively.

2.3 Optoacoustic Forcing

We first model the electric field grating in the sample volume defined by the shallow-angle intersection of the two driver beams. Assume each driver laser beam has a Gaussian profile with Gaussian half-width ω and denote the normalized electric fields of the two driver lasers by $\mathsf{E}_{d1}(\vec{r},t)$ and $\mathsf{E}_{d2}(\vec{r},t)$ respectively so that

$$\mathsf{E}_{d1} = \mathsf{E}_1 + \mathsf{E}_1^* \qquad \mathsf{E}_{d2} = \mathsf{E}_2 + \mathsf{E}_2^*, \tag{2.1a}$$

where $()^*$ denotes the complex conjugate. Then

$$\mathsf{E}_1 = \frac{\mathcal{E}(t)}{2}\sqrt{\frac{2}{\pi\omega^2}}\exp\left\{ik_d\hat{e}_1\cdot(\vec{r}-\vec{r}_1)-if_dt\right\}\exp\left\{-\left|\frac{\hat{e}_1\otimes(\vec{r}-\vec{r}_1)}{\omega}\right|^2\right\}, \tag{2.1b}$$

$$\mathsf{E}_2 = \frac{\mathcal{E}(t)}{2}\sqrt{\frac{2}{\pi\omega^2}}\exp\left\{ik_d\hat{e}_2\cdot(\vec{r}-\vec{r}_2)-if_dt\right\}\exp\left\{-\left|\frac{\hat{e}_2\otimes(\vec{r}-\vec{r}_2)}{\omega}\right|^2\right\}, \tag{2.1c}$$

where $\mathcal{E}(t)$ is the temporal electric field envelope, $\otimes$ denotes the vector cross product, f_d is the driver laser frequency, k_d is the wave vector magnitude, $\vec{r}_1 = (x_1, y_1, z_1)$ and $\vec{r}_2 = (x_2, y_2, z_2)$ are the Cartesian coordinates of the foci of the two beams respectively, and

$$\hat{e}_1 = (\cos\theta\cos\phi_1, \sin\theta, \sin\phi_1), \tag{2.1d}$$

$$\hat{e}_2 = (\cos\theta\cos\phi_2, -\sin\theta, \sin\phi_2) \tag{2.1e}$$

are unit vectors in the direction of the driver beams, where θ is the driver beam crossing half-angle and ϕ_1 and ϕ_2 are the angular misalignments of the driver beams. One assumption that is made is that the driver beams are of equal strength and geometry. This will be impossible to achieve experimentally. Deviations from this condition result in an otherwise equivalent grating with a Gaussian background intensity[28,46,47] (Fig. 2.2b) which will cause no significant scattering of the source beam

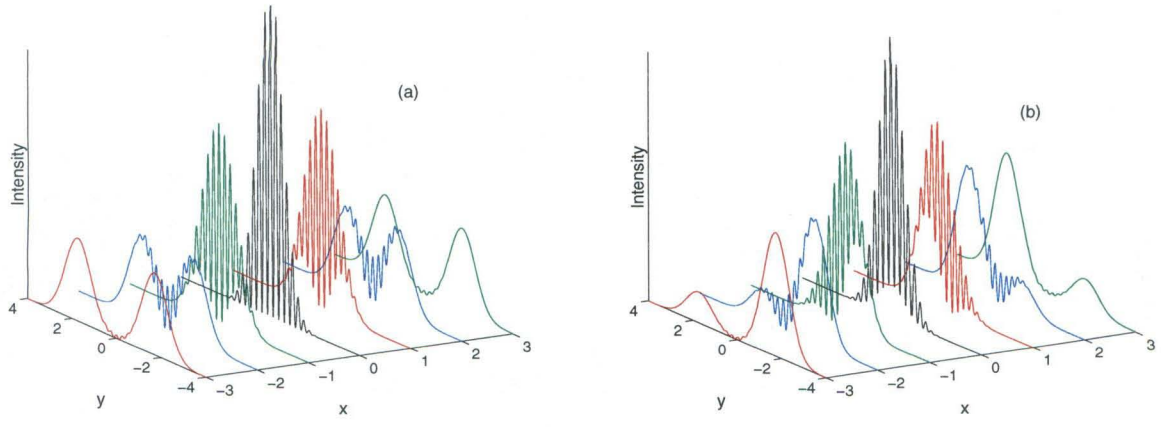

Figure 2.2: Electric field intensity for two intersecting laser beams of equal strength (a) and for the case where one beam only has 1/4 the intensity of the other one (b). We see the low frequency (Gaussian) background contributions in the electric field grating that are dropped in Eqn. 2.2. After Eichler *et al.*[28]

at the grating Bragg angle so that this assumption can safely be made. To keep the algebra as compact as possible, angular misalignments will be dropped at this point, *i.e.*, $\phi_1 = \phi_2 = 0$. Also note that since the driver pulse is short compared to all other relevant time scales, we assume the fluid does not move during the pulse and so any velocity terms (not shown in Eqns. 2.1b and c) can be safely neglected for the opto-acoustic forcing process. They have to be included, however, for the grating evolution which takes several orders of magnitude longer. Now, calculate the electric field grating intensity to be

$$\begin{aligned} I &= |\mathsf{E}_{d1} + \mathsf{E}_{d2}|^2 = (\mathsf{E}_{d1} + \mathsf{E}_{d2})(\mathsf{E}_{d1} + \mathsf{E}_{d2})^* \\ &\cong 2\,(\mathsf{E}_1^*\mathsf{E}_2 + \mathsf{E}_1\mathsf{E}_2^*) = E_d I_d P_d(t) \end{aligned} \tag{2.2}$$

where only the cross terms were retained in the first step as the other terms do not add spatially oscillating contributions but only a slowly spatially varying background (see Appendix A), similar to the case of not equally strong driver beams mentioned above. In the second step we decompose the intensity into the total driver laser energy E_d, the normalized spatial grating intensity distribution I_d, and the normalized driver

laser temporal profile P_d which we will approximate by a Dirac delta function at a later point. The result for I_d is

$$I_d = \frac{2}{\pi\omega^2}\cos\left\{2k_d\left[-\xi\cos\theta + (y-\overline{\eta})\sin\theta\right]\right\} \times \exp\left\{-\frac{2}{X^2}\left[x-\left(\overline{\xi}-\frac{X}{Y}\eta\right)\right]^2 - \frac{2}{Y^2}\left[y-\left(\overline{\eta}-\frac{Y}{X}\xi\right)\right]^2 - \frac{2}{Z^2}\left[\left(z-\overline{\zeta}\right)^2+\zeta^2\right]\right\}, \tag{2.3a}$$

where

$$\begin{aligned} X &= \frac{\omega}{\sin\theta} & Y &= \frac{\omega}{\cos\theta} & Z &= \omega \\ \overline{\xi} &= (x_1+x_2)/2 & \overline{\eta} &= (y_1+y_2)/2 & \overline{\zeta} &= (z_1+z_2)/2 \\ \xi &= (x_1-x_2)/2 & \eta &= (y_1-y_2)/2 & \zeta &= (z_1-z_2)/2. \end{aligned} \tag{2.3b}$$

At this point we use the fact the the beam crossing angle is small and that hence the $X \gg Y, Z$. Consequently, we neglect all variations in the x-direction including the misalignments. The side effect of this assumption together with the assumption of no angular misalignments is that we exclude any rotation of the grating, *i.e.*, it is always perpendicular to the y-direction. The proper limit of Eqn. 2.3a is then

$$I_d = \frac{2}{\pi\omega^2}\exp\left\{-\frac{2}{Y^2}\left[(y-\overline{\eta})^2+\eta^2\right] - \frac{2}{Z^2}\left[\left(z-\overline{\zeta}\right)^2+\zeta^2\right]\right\}\cos\left\{q_\psi(y-\overline{\eta})\right\} \tag{2.4}$$

with $q_\psi = 2k_d\sin\theta$. Eqn. 2.4 represents a fringe pattern perpendicular to the y-direction with a Gaussian intensity profile centered at $(0, \overline{\eta}, \overline{\zeta})$.

At a later point we will have to take the three-dimensional convolution of I_d with Green's function of the fluid response to the electric field. This operation will be performed by multiplying the expressions in Fourier space. The spatial Fourier

transform of Eqn. 2.4 is

$$I_d(\vec{q}) = \frac{YZ}{2\omega^2} \exp\left\{-\frac{2}{Y^2}\eta^2 - \frac{2}{Z^2}\zeta^2 - \frac{Z^2}{8}q_z^2 + i\bar{\eta}q_y + i\bar{\zeta}q_z\right\} \times \left[\exp\left\{-\frac{Y^2}{8}(q_y - q_\psi)^2\right\} + \exp\left\{-\frac{Y^2}{8}(q_y + q_\psi)^2\right\}\right]. \quad (2.5)$$

2.4 Grating Evolution

Here one invokes an analysis of optoacoustic effects and the evolution of the resulting hydrodynamic disturbances in order to model how the fluid responds to the electric field grating.

Two such effects have been observed in LITA. Thermalization is the process of absorption of driver laser energy by the fluid. The fluid temperature increases locally where the electric field grating intensity is high. The temperature perturbations are typically fractions of 1 K. This heating process due to super-elastic collisions typically occurs quickly compared to the Brillouin period of the grating. In the short duration of the driver pulse, no bulk fluid displacement can occur. Therefore, the density field cannot change during this time frame. Linear hydrodynamics shows that this field may be decomposed into the superposition of three density perturbation gratings that cancel at $t = 0$. One grating is due to the temperature grating and represents the equilibrium solution. It is offset by two density gratings of opposite sign and half the amplitude. For $t > 0$ these propagate in opposite directions at the local speed of sound. The second effect is electrostriction, which describes the effect that polarizable molecules accelerate along or against an electric field gradient. As with thermalization, the driver pulse is too short for bulk fluid displacement. As a result two acoustic waves of opposite sign are created at $t = 0$. For $t > 0$, they propagate in opposite directions. If we briefly assume our frame of reference to move with the fluid, we can adopt the analysis of the opto-acoustic response of the fluid to the electric field from Cummings *et al.*[29] and, to switch back to our original fixed coordinate

system, superimpose a (constant) external fluid velocity $\vec{u} = (0, v, w)$.

Starting from the linearized equations of motion with forcing terms for electrostriction (in the momentum equation) and for thermalization (in the energy equation), the Green's functions H_θ and H_e for the opto-acoustic response of the fluid to thermalization and electrostriction, respectively, are

$$H_\theta(q,t) = H_{\theta P1}\Phi_{P1} + H_{\theta P2}\Phi_{P2} + H_{\theta T}\Phi_T + H_{\theta D}\Phi_D \tag{2.6a}$$

$$H_e(q,t) = H_{eP1}\Phi_{P1} + H_{eP2}\Phi_{P2} + H_{eT}\Phi_T, \tag{2.6b}$$

where

$$\begin{aligned}
\Phi_{P1,2}(q,t) &= \exp\left\{-\Gamma q^2 t \pm i c_s q t + i v t q_y + i w t q_z\right\} \\
\Phi_T(q,t) &= \exp\left\{-D_T q^2 t + i v t q_y + i w t q_z\right\} \\
\Phi_D(q,t) &= \exp\left\{-(\gamma_\theta + \gamma_{n\theta})t - D_s q^2 t + i v t q_y + i w t q_z\right\}
\end{aligned} \tag{2.6c}$$

$$\begin{aligned}
H_{\theta P1} &= \frac{[1 + i(\Delta - G)][1 - G\Pi - i\Pi]}{2[1 + (\Delta - G)^2][(1 - G\Pi)^2 + \Pi^2]} = H^*_{\theta P2} \\
H_{\theta T} &= -\frac{1}{[1 + (\Delta - G)^2][1 - \Delta\Pi]} \qquad H_{\theta D} = \frac{\Pi^2}{[(1 - G\Pi)^2 + \Pi^2][1 - \Delta\Pi]} \\
H_{eP1} &= i\frac{[1 - i(\gamma\Delta - G)][1 + i(\Delta - G)]}{2[1 + (\Delta - G)^2]} = H^*_{eP2} \qquad H_{eT} = \frac{(\gamma - 1)\Delta}{[1 + (\Delta - G)^2]},
\end{aligned} \tag{2.6d}$$

and

$$\Pi = c_s q/(\gamma_\theta + \gamma_{n\theta} + D_s q^2). \tag{2.6e}$$

Δ is the thermal grating damping over a period of acoustic motion, and Γ is the acoustic damping rate ($\Gamma = 1/2[(\gamma - 1)D_T + D_V]$). Π is the ratio of the sound wave frequency with the wave vector q_y to the excited state energy decay rate. γ is the ratio

of specific heats, D_T the thermal diffusivity, D_V the longitudinal kinematic diffusivity of the fluid, and D_S the diffusivity of excited-state target molecules. γ_θ is the rate of excited-state energy decay caused by thermalization while $\gamma_{n\theta}$ is the energy decay rate not due to thermalization.

Φ_{P1} and Φ_{P2} are associated with the acoustic waves traveling in opposite directions, Φ_T is related to the density perturbations caused by the thermal grating, and Φ_D is due to the finite thermalization rate. A single-rate thermalization process is assumed. The density-time behavior is then

$$\frac{\rho\prime(\vec{q},t)}{\rho} = -\omega^2 I_d P_d(t) \circ [H_\theta U_\theta + H_e U_e] \tag{2.7}$$

where U_θ and U_e are the approximate modulation depths of the thermalization and the electrostriction grating respectively, and $\circ$ denotes a temporal convolution.

$I_d(\vec{q})$ is peaked at $\vec{q} = (0, q_\psi, 0)$. So, assume that $H_{\theta P1,P2,T,D}$ and $H_{eP1,P2,T}$ are equal to their values at $q = q_\psi$. Also, approximate to first order, $q \approx q_y$. This implies the assumption of plane wave fronts which is a good approximation if the waves have not traveled too far from their point of origin and if the fringe spacing is small. Also note that $q_z = 0$ implies a constant intensity in q_y-direction when, in fact, the intensity has a Gaussian profile in this direction. But the error is only a multiplicative factor, since all grating cross sections perpendicular to q_z are self-similar.

Taking the inverse Fourier transform of the products

$$\Phi^{(d)}_{\{P1,P2,T,D\}} = I_d(\vec{q})\Phi_{\{P1,P2,T,D\}}(\vec{q},t), \tag{2.8}$$

we obtain:

$$\Phi^{(d)}_{P1,2}(\vec{r},t) = \frac{2}{\pi\omega^2}\exp\left\{-\frac{2}{Y^2}\eta^2 - \frac{2}{Z^2}\zeta^2\right\}\exp\left\{-\Gamma q_\psi^2 t\right\}\cos\left\{(y-(v\pm c_s)t)\,q_\psi\right\}$$
$$\times\exp\left\{-\frac{2}{Y^2}\left[y-(\overline{\eta}+(v\pm c_s)t)\right]^2 - \frac{2}{Z^2}\left[z-\left(\overline{\zeta}+wt\right)\right]^2\right\} \tag{2.9a}$$

$$\Phi^{(d)}_{T}(\vec{r},t) = \frac{2}{\pi\omega^2}\exp\left\{-\frac{2}{Y^2}\eta^2 - \frac{2}{Z^2}\zeta^2\right\}\exp\left\{-D_T q_\psi^2 t\right\}\cos\left\{(y-vt)\,q_\psi\right\}$$
$$\times\exp\left\{-\frac{2}{Y^2}\left[y-(\overline{\eta}+vt)\right]^2 - \frac{2}{Z^2}\left[z-\left(\overline{\zeta}+wt\right)\right]^2\right\} \tag{2.9b}$$

$$\Phi^{(d)}_{D}(\vec{r},t) = \frac{2}{\pi\omega^2}\exp\left\{-\frac{2}{Y^2}\eta^2 - \frac{2}{Z^2}\zeta^2\right\}\exp\left\{-D_S q_\psi^2 t-(\gamma_\theta+\gamma_{n\theta})t\right\}\cos\left\{(y-vt)\,q_\psi\right\}$$
$$\times\exp\left\{-\frac{2}{Y^2}\left[y-(\overline{\eta}+vt)\right]^2 - \frac{2}{Z^2}\left[z-\left(\overline{\zeta}+wt\right)\right]^2\right\}. \tag{2.9c}$$

In Eqns. 2.9a-c, the assumption is made that the length scales do not change due to diffusion over the LITA time scales. Also, a phase shift of $\overline{\eta}q_\psi$ has been dropped in all three cosine terms.

2.5 Acousto-Optical Scattering

After describing the creation and time evolution of the density grating in the sample volume, the next step is to model how a continuous source beam focused at the origin and incident on the grating at the phase-matched angle ψ scatters off the grating into the coherent signal beam.

If we assume the density variations $\rho\prime$ to be small, we can use the linearized equation of light scattering.[48] A narrow-band source beam $\mathsf{E}_0(\vec{r},t)\cos(f_0 t)$ scatters into the electric field E_s by a small disturbance in the susceptibility $\chi(\vec{r},t;f)$. In the far field:

$$\mathsf{E}_s(\vec{R},t;\vec{q}) = -\frac{k_s^2}{4\pi R}\cos(\vec{k}_s\cdot\vec{R}-f_0 t)\mu(\vec{q},t), \tag{2.10}$$

where k_s is the wave vector of the scattered beam, f_0 is the frequency of the source

beam, $\vec{R}$ is the position vector relative to the scatterer, and $\mu(\vec{q},t)$ is the Fourier transform of the overlap of the susceptibility grating and the source laser field

$$\mu(\vec{r},t) = \chi\prime(\vec{r},t;f_0)\mathsf{E}_0(\vec{r},t). \tag{2.11}$$

Just as with the driver beams, we assume the source beam to have a spatial Gaussian intensity profile. Hence,

$$\mathsf{E}_S = \mathsf{E}_0 + \mathsf{E}_0^* \tag{2.12a}$$

$$\mathsf{E}_0 = \frac{1}{2}\exp\{ik_0\hat{e}_0\cdot\vec{r} - if_0t\}\exp\left\{-\left|\frac{\hat{e}_0\otimes\vec{r}}{\sigma}\right|^2\right\} \tag{2.12b}$$

$$\hat{e}_0 = (\cos\psi, \sin\psi, 0). \tag{2.12c}$$

Proceeding as before with the driver lasers, the electric field of the source laser is $\mathsf{E}_S(\vec{r},t) = P_0(t)I_0(\vec{r})\cos(f_0t)$ with

$$I_0 = \sqrt{\frac{2}{\pi\sigma^2}}\exp\left\{-\left(\frac{y}{\sigma_y}\right)^2 - \left(\frac{z}{\sigma_z}\right)^2\right\}, \tag{2.13a}$$

where σ is the Gaussian half-width of the source laser and

$$\sigma_y = \frac{\sigma}{\sin\psi} \qquad \sigma_z = \sigma. \tag{2.13b}$$

In Eqns. 2.13a,b variations in x-direction have been neglected by assuming $\sigma_x = \sigma/\sin\psi \gg \sigma_y, \sigma_z$. Define $\Phi^{(d,0)}_{\{P1,P2,T,D\}}(\vec{r},t) = I_0(\vec{r})\Phi^{(d)}_{\{P1,P2,T,D\}}$, the field of the overlap of the source beam and the evolving density grating. Taking the Fourier transform of these products, we can write

$$\Phi^{(d,0)}_{\{P1,P2,T,D\}}(\vec{q},t) = N\Psi_{\{P1,P2,T,D\}}(\vec{q},t)\Sigma_{\{P1,P2,T,D\}}(t) \tag{2.14a}$$

where

$$N = \frac{\sqrt{2/\pi}}{\sigma\omega^2}\left(\frac{Y^2\sigma_y^2}{Y^2+2\sigma_y^2}\right)^{1/2}\left(\frac{Z^2\sigma_z^2}{Z^2+2\sigma_z^2}\right)^{1/2}\exp\left\{-\frac{2}{Y^2}\eta^2-\frac{2}{Z^2}\zeta^2\right\} \tag{2.14b}$$

$$\begin{aligned}\Psi_{P1,2} =& \exp\left\{-\frac{1}{4}\frac{Y^2\sigma_y^2}{Y^2+2\sigma_y^2}\left(q_y-q_\psi\right)^2+i\frac{2\sigma_y^2}{Y^2+2\sigma_y^2}\left(\overline{\eta}+(v\pm c_s)t\right)\left(q_y-q_\psi\right)\right\}\\ &\times\exp\left\{-\frac{1}{4}\frac{Z^2\sigma_z^2}{Z^2+2\sigma_z^2}q_z^2+i\frac{2\sigma_z^2}{Z^2+2\sigma_z^2}\left(\overline{\zeta}+wt\right)q_z\right\}\\ \Psi_T =& \exp\left\{-\frac{1}{4}\frac{Y^2\sigma_y^2}{Y^2+2\sigma_y^2}\left(q_y-q_\psi\right)^2+i\frac{2\sigma_y^2}{Y^2+2\sigma_y^2}\left(\overline{\eta}+vt\right)\left(q_y-q_\psi\right)\right\}\\ &\times\exp\left\{-\frac{1}{4}\frac{Z^2\sigma_z^2}{Z^2+2\sigma_z^2}q_z^2+i\frac{2\sigma_z^2}{Z^2+2\sigma_z^2}\left(\overline{\zeta}+wt\right)q_z\right\}=\Psi_D\end{aligned} \tag{2.14c}$$

$$\begin{aligned}\Sigma_{P1,2} =& \exp\left\{-\Gamma q_\psi^2 t-\frac{2\left(\overline{\eta}+(v\pm c_s)t\right)^2}{Y^2+2\sigma_y^2}-\frac{2}{Z^2+2\sigma_z^2}\left(\overline{\zeta}+wt\right)^2+iq_\psi(v\pm c_s)t\right\}\\ \Sigma_T =& \exp\left\{-D_T q_\psi^2 t-\frac{2\left(\overline{\eta}+vt\right)^2}{Y^2+2\sigma_y^2}-\frac{2\left(\overline{\zeta}+wt\right)^2}{Z^2+2\sigma_z^2}+iq_\psi vt\right\}\\ \Sigma_D =& \exp\left\{-D_s q_\psi^2 t-(\gamma_\theta+\gamma_{n\theta})t-\frac{2\left(\overline{\eta}+vt\right)^2}{Y^2+2\sigma_y^2}-\frac{2\left(\overline{\zeta}+wt\right)^2}{Z^2+2\sigma_z^2}+iq_\psi vt\right\}\end{aligned} \tag{2.14d}$$

In Eqn. 2.14c, the contributions from a similar lobe centered at $q_y=-q_\psi$ have been neglected. Using this result in Eqn. 2.10 yields the electric field of the signal beam,

$$\begin{aligned}\frac{\mathsf{E}_s(\vec{q},\vec{R},t)}{P_0(t)} =& -\frac{k_s^2\omega^2}{4\pi R}\chi(f_0)\exp\left\{i\left(\vec{k}_s\cdot\vec{R}-f_0t\right)\right\}P_d(t)\\ &\circ\Re\left[A_{P1}\Phi_{P1}^{(d,0)}+A_{P2}\Phi_{P2}^{(d,0)}+A_T\Phi_T^{(d,0)}+A_D\Phi_D^{(d,0)}\right],\end{aligned} \tag{2.15a}$$

where we used

$$A_{P1,2}=U_\theta H_{\theta P1,2}+U_e H_{eP1,2}\qquad A_T=U_\theta H_{\theta T}+U_e H_{eT}\qquad A_D=U_\theta H_{\theta D} \tag{2.15b}$$

and where $\Re(\cdot)$ denotes the real part.

2.6 Detected LITA Signal

The detected LITA signal using heterodyne detection is then simply the integral of Eqn. 2.15 over the detection angle where the detector is centered at $\vec{q} = (0, q_\psi, 0)$. In the limit for a small detector, Eqn. 2.15 multiplied by the detection angle is the LITA signal. In the experiments presented here, homodyne detection is used. The detector measures the intensity of the electric field, *i.e.*, the square of the modulus of Eqn. 2.15.

$$\begin{aligned}\frac{\mathcal{L}_{hom}}{P_0^2(t)} =& \frac{k_0\omega^4}{16\pi^2\cos^2\psi}\,|\chi(f_0)|^2 \\ &\times \left(A_{P1}\Phi_{P1}^{(d,0)} + A_{P1}\Phi_{P2}^{(d,0)} + A_T\Phi_T^{(d,0)} + A_D\Phi_D^{(d,0)}\right) \\ &\times \left(A_{P1}^*\Phi_{P1}^{(d,0)*} + A_{P1}^*\Phi_{P2}^{(d,0)*} + A_T\Phi_T^{(d,0)*} + A_D\Phi_D^{(d,0)*}\right) \qquad (2.16)\end{aligned}$$

In Eqn. 2.16 we used the fact that the driver pulse (≈ 7 ns) is short compared to the inverse Brillouin frequency and it was approximated by a Dirac delta function which eliminated the double temporal convolution over the driver pulse time history.

In the large detector limit the integration over the detection angle can be approximated by infinite integrals. The final result is then

$$\begin{aligned}\frac{\mathcal{L}_{hom}}{P_0^2(t)} =& \frac{k_0^2}{4\pi^2\cos^2\psi}\,|\chi(f_0)|^2 \exp\left\{-\frac{2}{Y^2}\eta^2 - \frac{2}{Z^2}\zeta^2\right\} \\ &\times \left[\exp\left\{-\frac{8\sigma_y^2}{Y^2\left(Y^2+2\sigma_y^2\right)}\left(\frac{c_s t}{2}\right)^2\right\}\left[(P_1+P_2)(T^*+D^*) + (P_1^*+P_2^*)(T+D)\right]\right. \\ &\quad + \exp\left\{-\frac{8\sigma_y^2}{Y^2\left(Y^2+2\sigma_y^2\right)}(c_s t)^2\right\}(P_1P_2^* + P_1^*P_2) \\ &\quad \left. + (P_1P_1^* + P_2P_2^* + TT^* + TD^* + T^*D + DD^*)\right] \qquad (2.17)\end{aligned}$$

where $P_1 = A_{P1}\Sigma_{P1}$, $T^* = A_T^*\Sigma_T^*$, *etc.* , and where the symbols $A_{P1,P2,T,D}$ and $\Sigma_{P1,P2,T,D}$ are defined in Eqn. 2.15b and Eqn. 2.14d, respectively.

In the absence of beam misalignments and fluid velocities, Eqn. 2.17 collapses to the solution in Cummings *et al.*[29] with the exception of a multiplicative constant. This difference is due to the fact that variations in the x-direction were dropped much earlier than in Cummings *et al.*[29]

In the absence of bulk fluid velocities, only the misalignment $\overline{\eta}$ changes the time history of the LITA signal whereas η, ζ, and $\overline{\zeta}$ simply decrease the signal intensity. Also, Eqn. 2.17 is symmetric w.r.t. all possible misalignments. In the absence of beam misalignments, both fluid velocities have a similar influence on the signal that resembles additional acoustic damping and thermal diffusion. Among all misalignment and velocity components, $\overline{\eta}$ and v are the most interesting. In particular by introducing a known $\overline{\eta}$ it is possible to measure the time it takes the density grating to travel to the interrogation beam, thereby obtaining the velocity component v more precisely than by means of an enhanced decay rate. Fig. 2.3 shows how intentionally misaligning the beams can produce a dependence of the signal on velocity that is more orthogonal to other parameters and therefore more accurately inferred from signals. Note that oscillations are still present in the signal so that the sound speed can also be measured. Depending on the range of velocities to be measured, suitable values for $\overline{\eta}$, ω, and θ can be chosen.

2.7 Experimental Setup

Figure 2.4 depicts a schematic diagram of the experimental setup. A Q-switched, frequency-doubled Nd:YAG laser (Spectra Physics, GCR-150-10) drives a dye laser emitting $\sim$ 10-mJ, 7-ns pulses at 589 nm with a repetition rate of 10 Hz. Behind iris $i2$, beam splitter bs splits the beam in approximately equal-intensity halves. Beam splitter bs and mirrors $m3$, $m4$, $m5$ are placed to match the path length of the two beams within $\sim$ 1 mm. Lens $l2$ with focal length of 750 mm focuses both beams onto the sample volume in the test section. Lens $l2$ and mirror $m6$ are mounted on

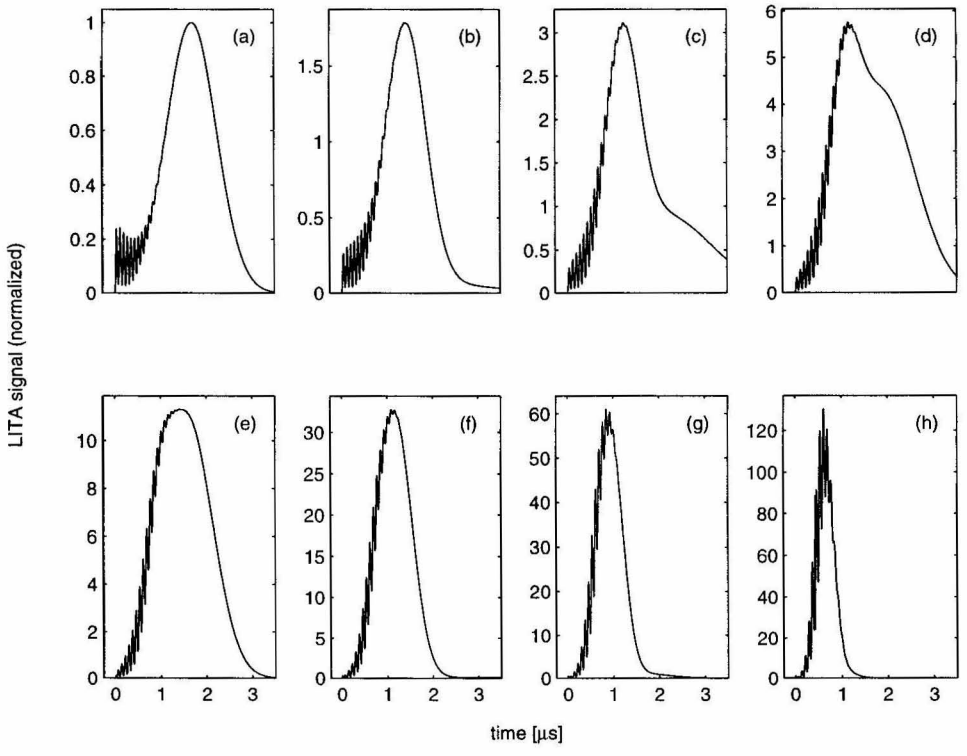

Figure 2.3: Theoretical LITA signals for atmospheric air from Eqn. 2.17 with $\theta = 1.23°$, $\omega = 370$ μm, $\sigma = 700$ μm, misalignment $\overline{\eta} = -2\omega$ and with fluid flow in +y-direction with different Mach numbers; a) $M = 0$, b) $M = 0.25$, c) $M = 0.5$, d) $M = 0.75$, e) $M = 1.0$, f) $M = 1.5$, g) $M = 2.0$, h) $M = 3.0$; *c.f.* Fig. 3.1.

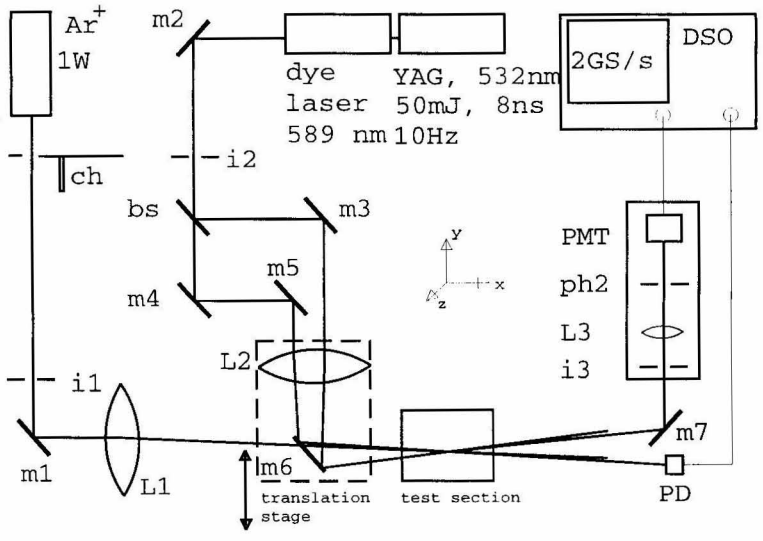

Figure 2.4: Schematic diagram of experimental LITA setup.

a translation stage with a 10-μm-resolution micrometer drive. The test section is a high-pressure bomb with optical access via anti-reflective coated BK7 windows on opposite sides.

A CW Argon-ion laser (Spectra Physics, Model 165) at 488 nm provides 0.5 W for the source beam. A chopper wheel *ch* (Scitech Instruments, Optical Chopper) blocks the beam except for pulses of 1-ms duration which are synchronized (LabSmith LC880) with the Q-switch trigger of the Nd:YAG laser. As with the driver laser, iris $i1$ partially removes unwanted beam modes, and lens $l1$ (f=1 m) focuses the beam onto the sample volume. The beam passes just over mirror $m6$ which directs the driver beams into the test section. Note that this optical setup introduces a small angular beam misalignment with $\phi_1 = \phi_2$. Mirror $m7$ directs the scattered beam through iris $i3$ into the receiver unit where lens $l3$ focuses it on d onto pinhole *ph* with a diameter of 400 μm.

The signal beam is detected by a photomultiplier tube (Hammamatsu model OPTO-8) and recorded on a digital storage oscilloscope (Tektronix, TDS 640A) from which it is transferred over an IEEE 488 bus to a personal computer for data analysis.

The transmitted part of the source (interrogation) beam is blocked as is one of the two driver beams exiting the test section. The other is detected by photo detector *PD* (Thor Labs, DET-2SI) and used to trigger the data acquisition. Each signal contains 2,000 data points taken at a sampling rate of $5 \cdot 10^8$ samples per second.

2.8 Procedure

For all experiments presented here, the test section was filled with atmospheric air seeded with NO_2 at concentrations on the order of parts per million. The low level of seeding enhances the signal level by typically two orders of magnitude without changing the results of the measurements. Also, this seeding makes thermalization predominant over electrostriction which can therefore be ignored.

For the data analysis, a standard personal computer (Pentium, 150MHz) is used to find the least-squares fit of a theoretical signal (Eqn. 2.17) to an experimental trace. To keep the number of floating fitting parameters as low as possible, values for the beam diameters ω and σ, beam crossing angle θ, *etc.* , are obtained from a set of calibration measurements. A Levenberg-Marquardt scheme is used for the least-squares fit, which is a combination of the inverse Hessian (multi-dimensional form of Newton's method) scheme and the method of steepest descent.[49]

Eqn. 2.17 was validated by moving the translation stage with lens $l2$ and mirror $m6$ in the y-direction, thus creating a known misalignment $\overline{\eta}$. The measurement started at a value of $\overline{\eta} = -2$ mm and a trace was recorded every 10 μm until reaching $\overline{\eta} = +2$ mm. Every trace was averaged over 64 driver-laser shots to reduce the noise levels at larger misalignments.

For these measurements in which the correct beam misalignment was to be inferred from the signal shape, only the misalignment component in question and U_θ, the thermal grating modulation depth, were adjusted during the numerical fit. The latter parameter had to be included to serve as a multiplicative factor since Eqn. 2.17

cannot accurately give the absolute signal but rather a relative time history whose total amplitude depends additionally on the characteristics of the detector and other factors.

In a second set of measurements, we wanted to find whether small beam misalignments affect the repeatability and/or accuracy of LITA measurements. This was of particular interest since it did not seem possible to detect such misalignments by the fitting procedure. Hence, at a number of fixed beam misalignments $\overline{\eta}$, 500 64-shot averages were obtained as data for a statistical analysis. Here, only the sound speed, thermal diffusivity, and U_θ where adjusted during the fitting procedure. These data sets were analyzed three different ways: first, with all misalignments (wrongly) set to zero, secondly with the misalignments held fixed at their correct values, and finally with the misalignment $\overline{\eta}$ set as a fitting parameter during the data analysis.

2.9 Results, Discussion

Fig. 2.5 shows LITA signals recorded with various misalignments together with the final results of the fitting routine for the theoretical traces. The theoretical results are shifted above the experimental signals for better comparison.

For large values of $\overline{\eta}$ (Fig. 2.5a & b), the only visible signal is due to an isolated acoustic wave passing through the source beam. We see that the onset of the signal has a steeper slope than the tail, a result of acoustic damping. Beam diameters can be inferred accurately from these traces. The width of the hump in the signal gives a good measure of the driver beam width ω. In the absence of acoustic damping, the deviation of the exact shape of the signal from a Gaussian profile gives information about the source beam diameter σ. But, since Γ is known in these experiments, this information can still be determined using the least-squares fit to Eqn. 2.17.

In Fig. 2.5c we see the first oscillations in the signal. This indicates that at this location there is a sizable overlap of the source beam with both the thermal grating

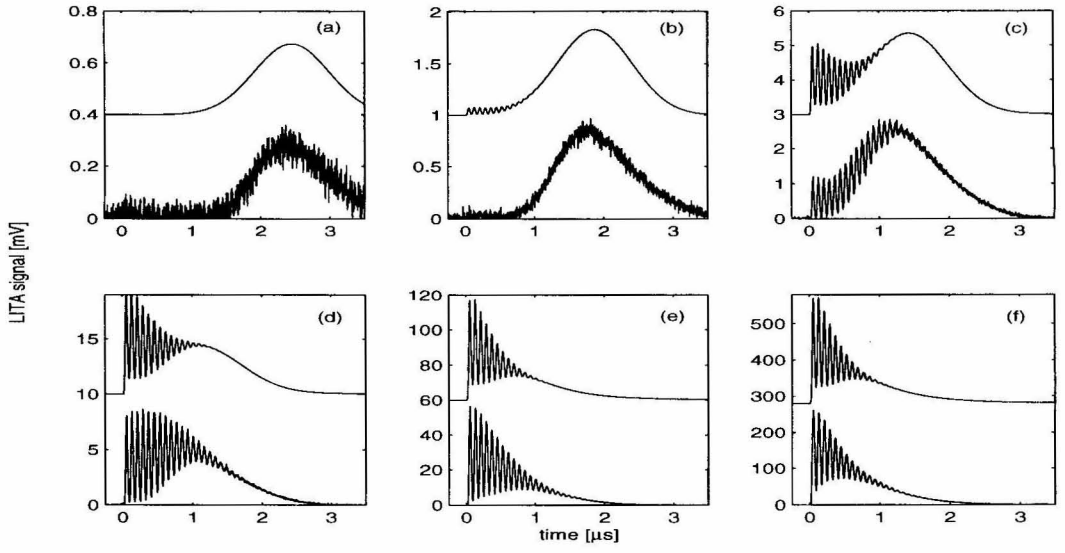

Figure 2.5: Experimental and theoretical LITA signals of atmospheric air, σ = 700 μm, ω = 370 μm, θ = 1.23°, and: a) $\overline{\eta}$ = −1100 μm, b) $\overline{\eta}$ = −900 μm, c) $\overline{\eta}$ = −700 μm, d) $\overline{\eta}$ = −600 μm, e) $\overline{\eta}$ = −500 μm, f) $\overline{\eta}$ = 0 μm. The top trace in each graph is the fitted theoretical signal, shifted for clarity.

and the acoustic waves. As $\overline{\eta}$ is decreased further, the hump moves to earlier times and the oscillations become stronger. Note the subtle change in signal shape between Figs. 2.5e and 2.5f considering the large change in $\overline{\eta}$.

Fig. 2.6 shows an experimental LITA signal together with the result of the fitting procedure. For clarity, they are plotted separately. We see how precise Eqn. 2.17 captures the features of a misaligned signal.

Fig. 2.7 shows the beam misalignment inferred by the fitting routine *vs.* the actual misalignment set by the translation stage. The dashed lines with a slope of ±1 correspond to the ideal case. For $\overline{\eta} > 550$ μm, the extracted values for $\overline{\eta}$ had the correct slope but were generally too small by about 200 μm. For large values of $\overline{\eta}$, the larger scatter in the measurements is due to the increased noise level in the signals. A linear regression for the region $|\overline{\eta}| > 600$ μm gives slopes in these regions of $m = -.946$ and $m = 0.995$, respectively, with a coefficient of determination,r^2, greater than 0.98. The standard error for the measured $\overline{\eta}$ is 22 μm. The labeled data

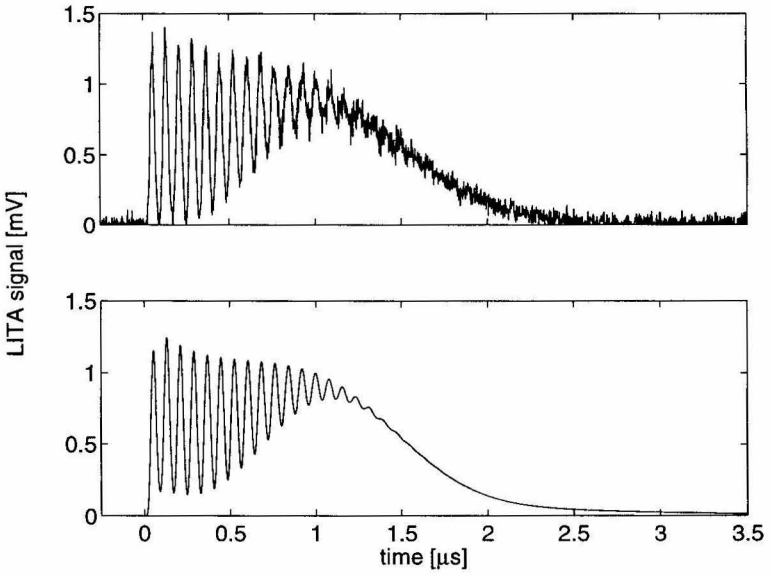

Figure 2.6: Experimental signal (top) and fitted theoretical signal (bottom) for $\overline{\eta} = -1000$ μm with $\omega = 370$ μm, $\sigma = 700$ μm, $\theta = 1.23°$ in atmospheric air.

points A through F correspond to the traces shown in Fig. 2.5a-f.

In the center region, the detected misalignment forms a plateau at 300 μm. The reason for this behavior is probably that the intensity profiles of the beams in the experiments are not well represented by Gaussians. Fig. 2.8, which shows the peak signal intensity *vs.* $\overline{\eta}$, also provides evidence that this assumption is not satisfied. If we give the fitting routine the option of an additional fitting parameter whose effect on the signal depends strongly on the beam profiles, *e.g.*, misalignment, while not accurately modeling the beam profiles, it is unlikely that the fitting routine will return the proper value of the parameter.

The dashed line in Fig. 2.8 represents the theoretical value of the (visible) peak intensity. The intensities are normalized with the intensity at $\overline{\eta} = 0$. First, consider the theoretical curve in which we can distinguish three regimes.

For $|\overline{\eta}| < 575$ μm (regime I) we find a Gaussian behavior for the signal intensity w.r.t. $\overline{\eta}$. Here, the peak value occurs early on in the LITA signal (Figs. 2.5e & f)

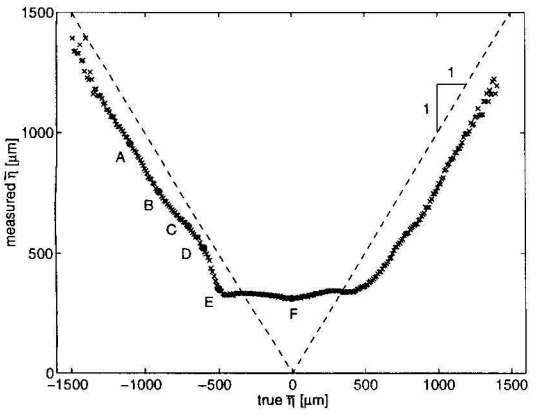

Figure 2.7: Measured *vs.* true misalignment $\overline{\eta}$. The dashed lines have a slope of ± 1 respectively. Traces shown in Fig. 2.5a-f correspond to data points labeled A-F. The experimental conditions are the same as in Fig. 2.5.

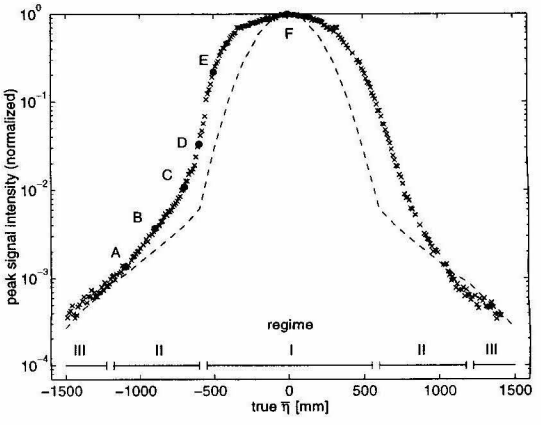

Figure 2.8: Normalized peak signal intensity *vs.* $\overline{\eta}$. Traces shown in Fig. 2.5a-f correspond to data points labeled A-F. The experimental conditions are the same as in Fig. 2.5.

due to constructive interference of the thermal grating with the acoustic waves. Both gratings have a Gaussian profile so the peak intensity scales the same way.

In regime II (575 μm $\leq |\overline{\eta}| \leq$ 1200 μm) the peak intensity occurs at later times in the signal when an isolated acoustic wave passes the interrogation beam (Figs. 2.5a & b). The travel time of the wave scales linearly with the misalignment. The wave's amplitude decreases exponentially with the acoustic damping rate Γ. This explains the linear behavior on a logarithmic plot for large misalignments in Fig. 2.8. Figs. 2.5c & d mark the transition between these two regimes.

For $|\overline{\eta}| >$ 1200 μm (regime III) the theoretical signal intensity decreases again faster than in region II. This is an artifact of the limited duration of the data acquisition. In this regime, the peak of the hump visible in Figs. 2.5a & b occurs after the end of the recording time.

The measured peak intensities are higher than predicted over a range of misalignments near perfect alignment before they approach the theoretical values at larger $\overline{\eta}$. The most likely explanation is the presence of laser modes other than TEM_{00}. A non-Gaussian beam profile could also be the explanation for fact that the oscilla-

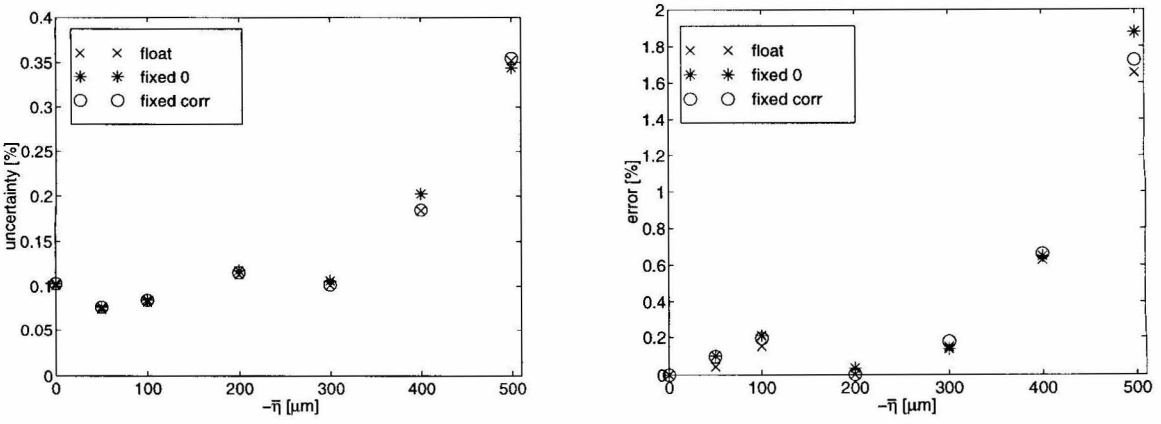

Figure 2.9: Uncertainty (left) and error (right) of sound speed *vs.* $\overline{\eta}$. The sound speed for $\overline{\eta} = 0$ is taken as reference. Three different fitting strategies were used. In the strategy denoted by "float," $\overline{\eta}$ is a floating fitting parameter, in "fixed 0," $\overline{\eta}$ is fixed at zero, and in "fixed corr," $\overline{\eta}$ was held constant at the correct preset value. The experimental conditions are the same as in Fig. 2.5.

tions decay more slowly than the theory predicts for the given (fixed) beam diameters (Fig. 2.5c-e).

We can see the transition from regime I to regime II in Fig. 2.8. The transition to III is less pronounced as at this point signals are very weak. We can see the effect of noise from the large amount of scatter in the intensities in Fig. 2.8.

As evidenced by Fig. 2.7 it was not possible to extract accurate measurements of small misalignments from the signal shape. This finding prompts the question of whether small misalignments have an impact on the accuracy and uncertainty of other LITA measurements. Figs. 2.9a & b respectively show the uncertainty and the accuracy of LITA measurements of sound speed *vs.* $\overline{\eta}$ for the three different fitting strategies.

All three fitting strategies yield almost identical results. For $|\overline{\eta}| \leq 300$ μm the uncertainty remains approximately constant at 0.1% as does the error of 0.2%, where the measured sound speed from the data set with $\overline{\eta} = 0$ has been taken as reference value. Only for $|\overline{\eta}| > 300$ μm do the uncertainty and error increase significantly.

Other types of misalignments that have been carried out experimentally include

measurements where only one driver beam was displaced in y-direction, thus inducing a simultaneous misalignment in $\overline{\eta}$ and η, movement of both beams in opposite directions (only η), and measurements with misalignments in the z-direction, *i.e.*, sweeps through $\overline{\zeta}$ and ζ. Misalignments in the y-direction produced similar results to those explained in detail above. For nonzero values of ζ or $\overline{\zeta}$, no change in signal shape has been observed as Eqn. 2.17 predicts.

When a small-diameter, 40 μm pinhole *ph* was used in the receiver unit, another form of misalignment was observed that is not included in Eqn. 2.17. Changes in signal shape did not appear to be symmetric w.r.t. $\overline{\eta}$. The most likely explanation for this asymmetry is that part of the signal beam was occluded by the pinhole. An illustration of this effect is shown in Fig. 2.10. In the upper half we see the intensity of the overlap of the density grating with the source beam in physical space along the y-axis as it develops over time. The bright and dark stripes correspond to the oscillations in the early stages of the signal whereas the bright tail reflects the exponentially decaying tail of the LITA signal.

In the large detector limit we assume that the detector integrates over the entire horizontal range in Fig. 2.10 (and beyond). Imagine that half of the signal beam is blocked so the receiver sees only the left or right half of the signal beam (receiver misalignment). The resulting LITA signals are given in the lower half of Fig. 2.10. We see that for $\overline{\eta} = 0$ this has no influence on the signal shape. In fact, we could take any region along the y-axis and would end up with the same signal shape, meaning that this kind of misalignment cannot be detected if the optics are otherwise perfectly aligned.

However, if $\overline{\eta} \neq 0$ then the time histories at different positions y are no longer self similar, resulting in different signals depending on which part of the signal beam the detector sees.

Figure 2.11 provides evidence that detector misalignment produces asymmetry in beam-misalignment effects. Here, two traces taken at $\overline{\eta} = \pm 650$ μm are shown from

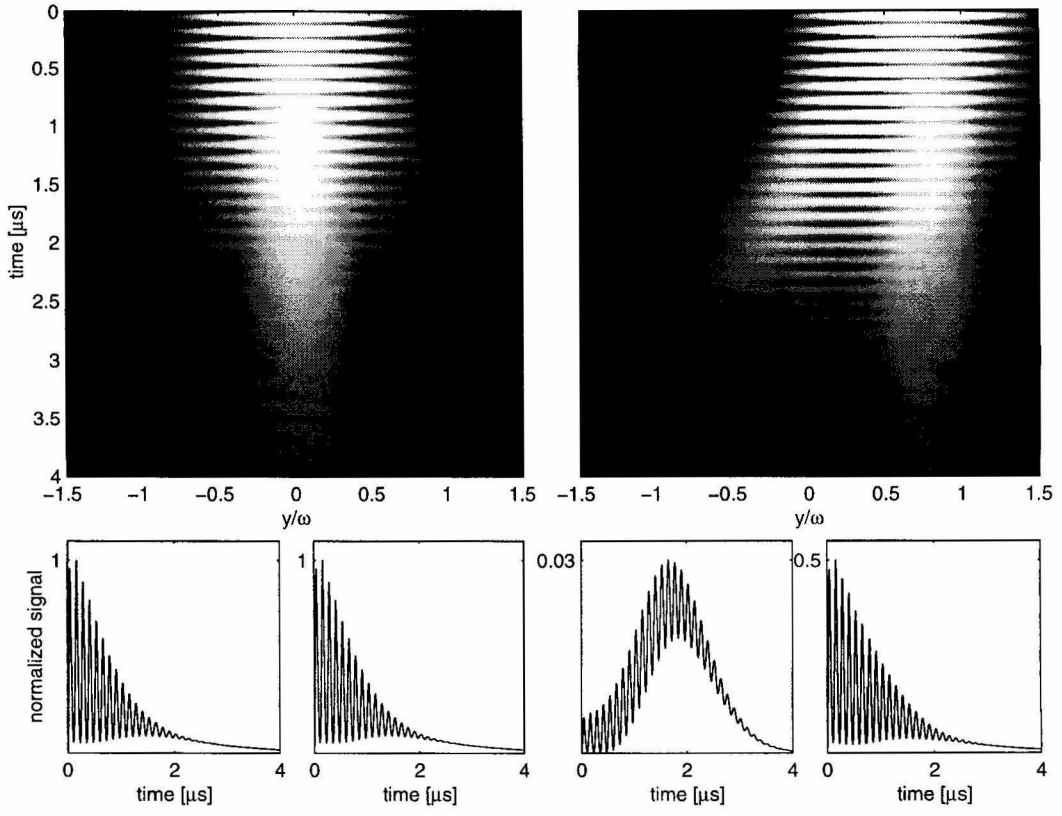

Figure 2.10: Intensity of overlap of density grating with source beam from the inverse Fourier Transform of Eqn. 2.14 for atmospheric air and at $z = 0$, *i.e.*, along the grating center line. On the top, the time history as a function of y-position is plotted - on the left for perfect beam alignment, on the right with $\overline{\eta} = \omega$. The experimental parameters are: $\sigma = \omega = 500$ μm, $\lambda_d = 589$ nm, $\theta = 0.8°$. White corresponds to high intensities, black to low intensities. In the lower portion, the resulting LITA signals are shown if the receiver only detects the range $y < 0$ or only $y > 0$, respectively.

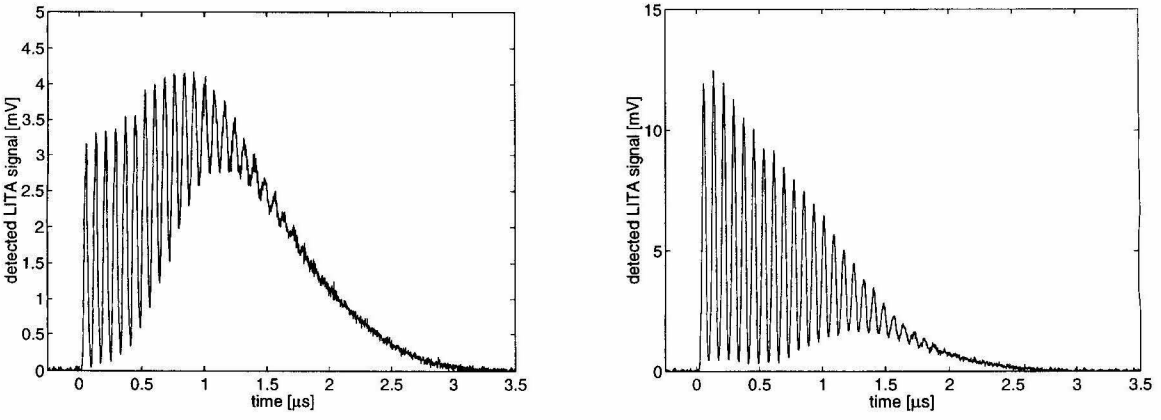

Figure 2.11: Two traces from a sweep through values of $\overline{\eta}$. Left trace: $\overline{\eta} = -650$ μm; right trace: $\overline{\eta} = +650$ μm. A small pinhole ph with a diameter of only 40 μm in the receiver unit blocked portions of the signal beam. Compare with theoretical results in Fig. 2.10.

earlier measurements with the 40 μm pinhole. We clearly see the difference in the signal shape. Compare Fig. 2.11 with the two traces in the lower right of Fig. 2.10.

To fully verify the origin of the asymmetry, we performed a series of measurements using the 40 μm pinhole in which, for several values of $\overline{\eta}$, the mirror $m7$ was translated to block different regions of the signal beam. The influence of receiver misalignment on the signal shape was demonstrated, but since this form of misalignment is not included in Fig. 2.17, no quantitative data can be given. Subsequently, the use of a larger size pinhole eliminated the asymmetry at the cost of increased sensitivity to incoherently scattered light and luminosity.

Finally, consider the case of angular beam misalignments and misalignments in the x-direction. Both can produce a rotation of the principal axes of the grating structure. As a consequence, the phase matching condition for the source beam may no longer be satisfied resulting in a weaker signal beam that may even be scattered into a different direction than anticipated. This alone, however, does not change the shape of the signal as long as the entire signal beam falls on the detector.

2.10 Conclusions

An analytical expression for the magnitude and time history of LITA signals from finite Gaussian beams in the presence of fluid velocities and the most common forms of beam misalignment has been derived. In experiments, some deviations from this expression were observed that were due to non-Gaussian laser beam profiles. In regions where this assumption was satisfied, however, the experiments showed very good agreement with the theory.

It has been demonstrated how beam misalignments can be detected quantitatively only from the shape of the signal. Small misalignments that could not be accurately measured were shown not to influence the accuracy or repeatability of sound speed measurements, even when the data analysis incorrectly assumed that no misalignments were present during the measurement.

Beam misalignment information provided by this technique can be used in the initial optical setup and to correct in real-time for slow occurring misalignments, *e.g.*, due to thermal expansion. The time-scale at which misalignments can be corrected is limited by the repetition rate of the driver laser so that a real-time alignment is not possible for turbulent flows where refractive index gradients may introduce random, non-stationary beam misalignments. In these situations it will be necessary to allow for beam misalignments in the data analysis.

Controlled beam misalignments may be advantageous for optimizing the accuracy of measurements of a particular parameter. For example, beam misalignments can improve the accuracy of homodyne LITA velocimetry.

Chapter 3

Homodyne Detection LITA Velocimetry

3.1 Introduction

LITA is a four-wave mixing technique that can be used to measure the speed of sound,[29,42] thermal diffusivity,[42] and flow velocity[38,45] of fluids remotely, non-intrusively, and instantaneously. If the gas composition is known, thermometry is possible.[44,50,51]

Two pulsed laser beams (driver beams) of equal strength intersect at a shallow angle in a test fluid. In the intersection region (sample volume) they create an electric field grating which, by the molecular mechanisms thermalization and electrostriction, results in a density and hence in a refractive index grating. The evolution of this grating can be examined by a continuous interrogation beam (source beam) which is directed at the Bragg angle at the grating. A small fraction of the source beam ($< 0.01\%$) is scattered into a coherent signal beam. The intensity of the signal beam depends on the instantaneous modulation depth of the refractive index grating. The time history of the signal beam intensity is recorded and the speed of sound, thermal diffusivity, and flow velocity can be extracted from the signal shape either by a frequency decomposition technique,[42,50,51] or by a nonlinear fitting technique that fits the experimental signal to a theoretical model.[29,36,38,52]

Previous applications of LITA for velocimetry purposes employed heterodyne detection.[38,45,51] Here one records the superposition of the signal beam and a reference beam. The convective motion of the grating produces a Doppler shift between the signal and reference beam that is proportional to the flow velocity and which is made visible by this detection method. Since heterodyne detection requires the alignment

and intensity adjustment of an additional laser beam, setting up and aligning such a system is more complex than for a LITA setup using homodyne detection where only the signal beam is recorded.

Using an extension of Cummings' *et al.*original model,[29,36] we demonstrate the possibility of simultaneous measurements of fluid velocities and the speed of sound with homodyne detection for high-speed flows (sub- and supersonic) with single laser pulses.

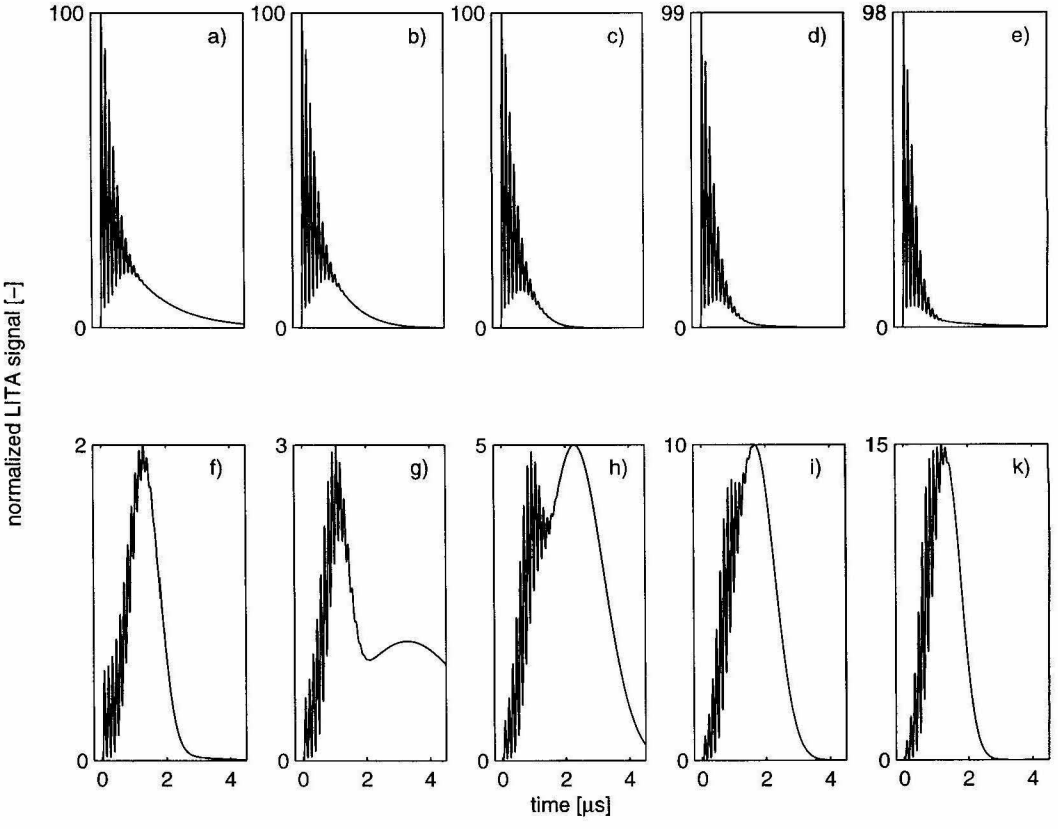

Figure 3.1: Computed LITA signals in the presence of fluid velocities for NO_2-seeded atmospheric air, and driver beam crossing angle $\theta = 0.8°$, driver beam half-width $\omega = 500$ μm, source beam half-width $\sigma = \omega$. Upper row (a-e) without beam misalignments, lower row (f-k) with $\overline{\eta} = -\omega$. Amplitudes are normalized such that the peak amplitude of trace a) equals 100. Fluid velocities: a & f: $M = 0$; b & g: $M = 0.25$; c & h: $M = 0.5$; d & i: $M = 0.75$; e & k: $M = 1$.

The presence of a bulk fluid velocity causes a change of the shape of the LITA signal. With an extended theoretical model that includes the effects of fluid veloc-

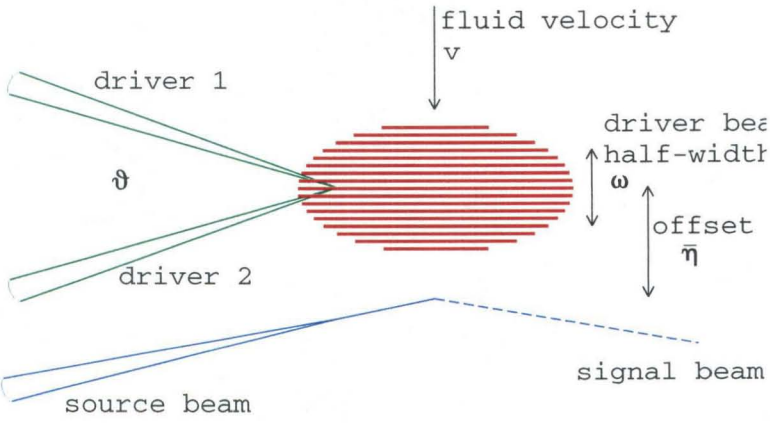

Figure 3.2: Schematic drawing of beam offset geometry. The essential parameters are the beam crossing angle θ and the driver laser wavelength which together determine the fringe spacing. Furthermore, the velocity u along the grating normal, the beam half-width ω and the source beam offset $\overline{\eta}$.

ities and beam misalignments[36] and using a nonlinear fitting technique such as the Levenberg-Marquardt scheme,[49] the flow velocity can be obtained by letting the velocity be a floating fitting parameter. A frequency decomposition technique is not capable of detecting these changes in signal shape. We show how introducing a beam misalignment (offset) can potentially improve the accuracy of this technique.

In the following section we will present a summary of the derivation of the theoretical model. The complete closed-form analytic solution can be found in Schlamp *et al.*[36] There, the main focus is on the effects of beam misalignments. Here, we will derive some conclusions with respect to homodyne LITA velocimetry. Afterwards, preliminary experimental results are presented from homodyne LITA velocimetry measurements in sub- and supersonic flow of NO_2-seeded nitrogen in a converging-diverging 2D nozzle.

3.2 Theory

The theoretical treatment of LITA starts from the linearized equations of motion with forcing terms in the momentum equation to account for the effect of electrostriction

and in the energy equation to model thermalization. This assumes that the fluctuations are small. Order of magnitude estimates indicate that the temperature perturbations due to thermalization are below 1 K. Thermalization is the process in which driver laser energy is converted into thermal energy in the fluid by means of inelastic collisions. Electrostriction describes the tendency of polarizable molecules to move in the presence of an electric field. The importance of these effects relative to each other depends on the test gas and the test conditions. We use NO_2 to seed the test gas which makes thermalization the predominant grating excitation mechanism. By using these equations we require that the grating Knudsen number (ratio of the mean-free path to the fringe spacing) is much less than unity so that the continuum approximation holds. In practical applications the extent of the grating is in the order of $.3 \times .3 \times 6$ mm^3 and we assume that the fluid velocity is constant within the sample volume. We do allow for all three velocity components. It will turn out, however, that only the velocity component along the grating normal has practical importance.

The next step is to model the opto-acoustic forcing, *i.e.*, the response of the fluid to the electric field grating generated by the driver beams. Assuming single-rate thermalization and quasi-steady electrostriction, Green's functions for the density perturbation created by thermalization and electrostriction can be derived analytically.[53]

The driver beams are assumed to be of equal strength, Gaussian in profile, with plane wavefronts where they intersect, and their pulse duration is short compared to the inverse Brillouin frequency so that their time history can be modeled by the Dirac delta function. It is also assumed that the beam crossing angle is small so that the grating is much longer than high or wide. Thus, variations in the lengthwise direction of the grating can be neglected. Furthermore, while allowing the driver beams to be misaligned spatially, we assume their angular alignment is perfect, *i.e.*, all three laser beams are co-planar. The effect of the latter two assumptions is that the orientation of the grating normal does not change. With these simplifications, one can find an

analytic expression for the electric field grating.[28,46,47] The convolution of the electric field with the Green's functions for the fluid response gives an expression for density perturbations as a function of time.

Next, using the linear equation of light scattering,[48] we find how a Gaussian source beam directed at the Bragg angle on this density grating is scattered into a coherent signal beam. Finally, integrating the modulus of the signal beam intensity over the detector area gives the LITA signal. In most experiments, the detector is large so that one integrates over the entire signal beam.

The final result is a rather lengthy expression, and the authors wish to refer to Schlamp *et al.*[36] for the complete expression. Originally, the work was intended to describe the effect beam misalignments have on the signal shape but as will be shown in the next section, the introduction of a known beam misalignment may prove helpful for velocimetry applications of LITA.

3.3 Theoretical Results

Fig. 3.1 shows computed traces from the theoretical model. Thermalization is assumed to be the predominant grating creation mechanism. The signals demonstrate how the signal shape changes in the presence of fluid velocities along the grating normal direction. The signal in the upper left-hand corner is the trace that is obtained for a fluid at rest with an optical setup in perfect alignment. Typical values were chosen for the experimental parameters such as driver beam half-width ($\omega = 500$ μm), source beam half-width ($\sigma = 500$ μm), driver beam crossing angle ($\theta = 0.8°$), and fluid properties (NO_2-seeded atmospheric air, $T = 293$ K). The speed of sound is encoded in the frequency of the oscillations in the early part of the signal (Brillouin frequency). The frequency is equal to the speed of sound divided by the spacing of the fringes in the grating which only depends on the wavelength of the driver beams and the driver beam crossing angle. The thermal diffusivity together with the finite

beam size effects govern the behavior of the decaying tail of the signal.

To the right of this reference trace we see signals with non-zero fluid velocities ranging in Mach numbers from 0.25 to sonic flow in the top right-hand corner. We see that the signals decay faster with increasing fluid velocities. To be precise, the effect of the fluid velocities is to accelerate the decay by a factor that scales like $exp(-(ut)^2)$, where u could be any velocity component. In the presence of noise, however, this effect will be hard to distinguish from a change in thermal diffusivity which is represented by a decay which scales like $exp(-D_T t - \Gamma t)$ where D_T is the thermal diffusivity and Γ is the acoustic damping rate. The accuracy is hence expected to be poor using this approach.

Furthermore, all three velocity components turn out to have this identical effect (with some scaling factor due to the different grating sizes in the three spatial directions). Only the velocity component along the grating normal has an additional effect that is coupled to beam misalignments. This effect is shown in the lower half of Fig. 3.1.

Here, we see traces with the same experimental parameters but now the source beam has an offset $\overline{\eta}$ such that it is directed at a position slightly downstream of the intersection point of the two driver beams (Fig. 3.2). We see that the influence of the fluid velocity on the resulting signal is dramatically different from the effect a change in thermal diffusivity would have. Notice especially the shape change from $M = 0$ to $M = 0.5$. The effect that a change in thermal diffusivity has on the signal has been temporally decoupled from the contribution of a bulk velocity. Mathematically, we see an $exp(-(\overline{\eta} - (c_s \pm v)t)^2)$ dependence. Instead of detecting fluid velocities by the decay of the signal tail, we essentially measure the "time-of-flight" of the density gratings. Also note that the signals in the lower half of Fig. 3.1 still contain oscillations at the Brillouin frequency that let us determine the speed of sound. The frequency of these oscillations is unaffected by the convective motion of the grating.

The signal amplitudes in Fig. 3.1 are normalized w.r.t. the reference trace in the

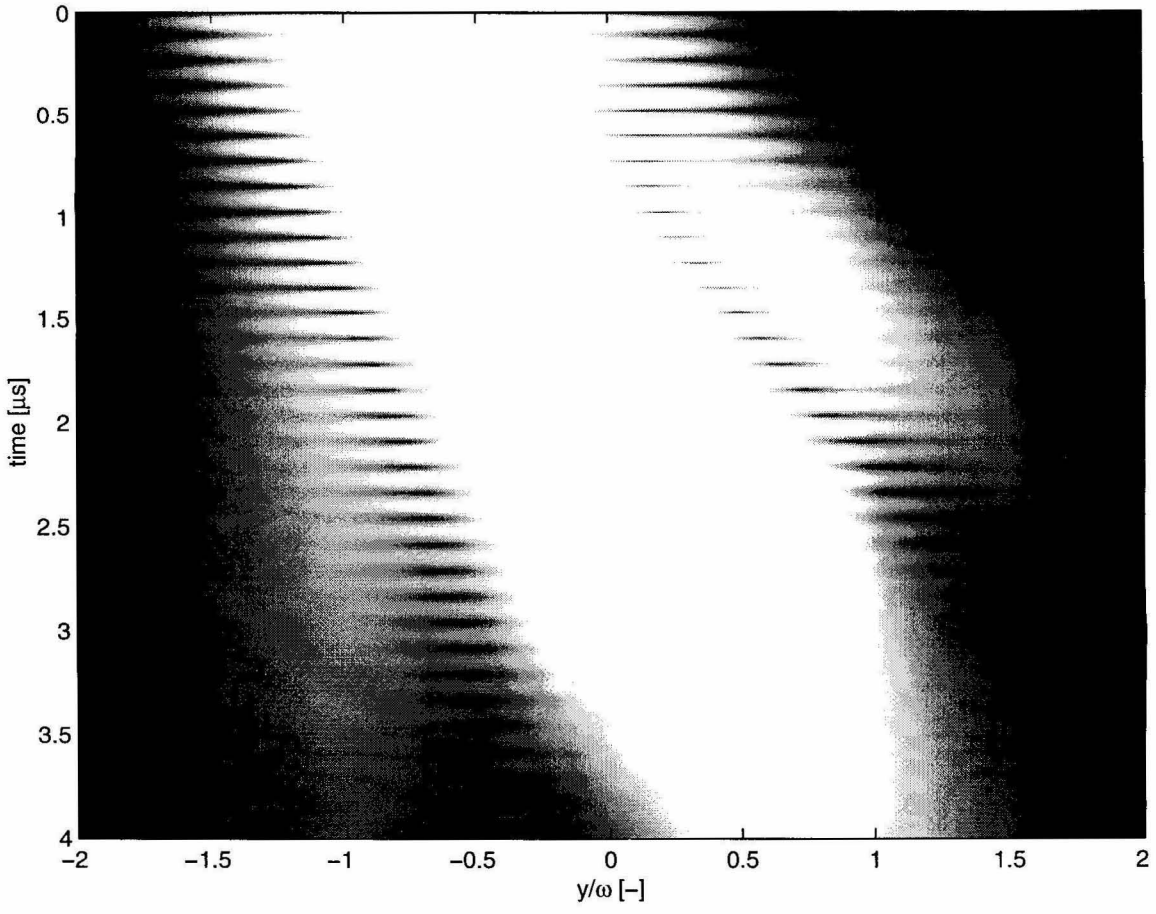

Figure 3.3: Computed cross section through signal beam in the presence of high-speed flow and with driver beam offset. Corresponds to case in Fig. 3.1i. Brightnesses are adjusted as to make weaker acoustic waves visible. Bright colors correspond to high intensities.

upper left-hand corner whose peak amplitude is set to 100. We see that with the beam misalignments the signal intensity is significantly lower. In previous experiments, however, the signal intensities with and without beam misalignments were high enough to make this loss acceptable. Furthermore, notice that the signal intensity increases with increasing Mach number in Fig. 3.1f-k. This is because the strong thermal grating is convected towards the source beam faster than it decays due to thermal diffusion (Fig. 3.3).

For the same experimental parameters, fluid conditions, source beam offset, and

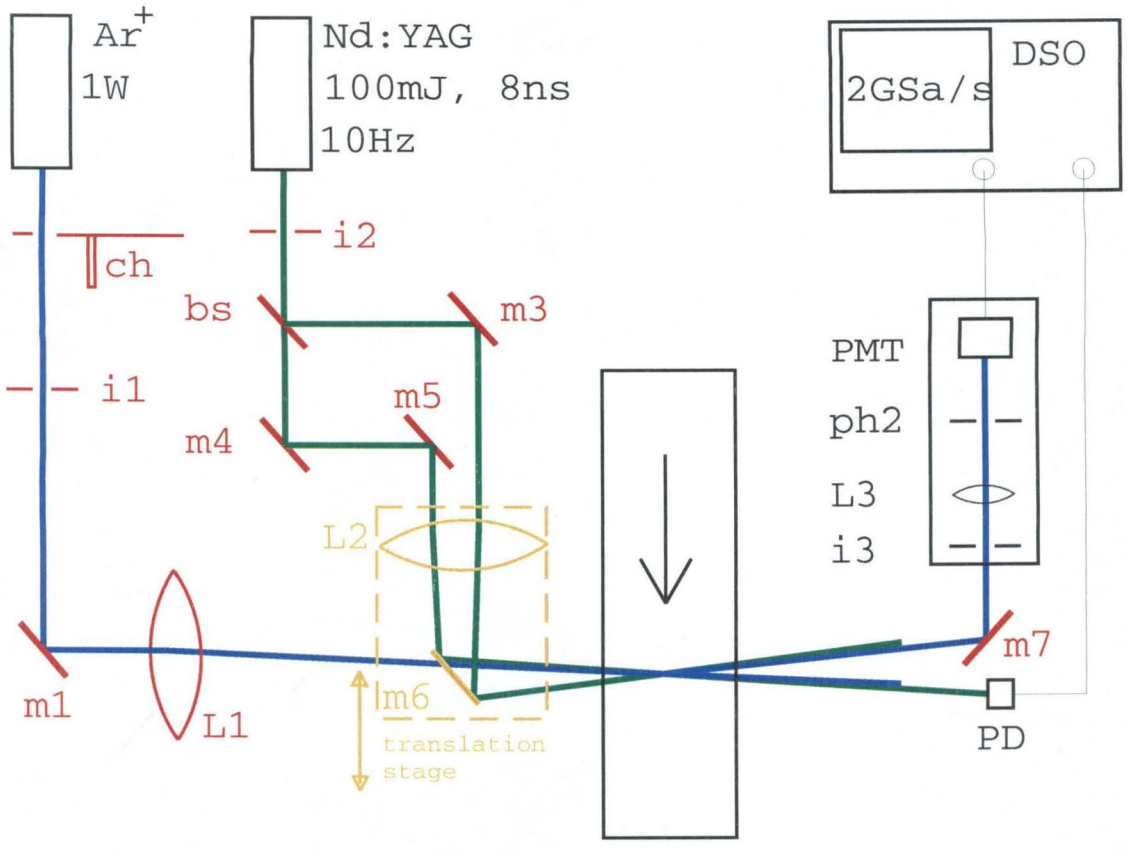

Figure 3.4: Experimental setup.

$M = 0.75$, Fig. 3.3 shows the evolution of a signal beam cross section over time. The flow is from left to right, the source beam is centered at $y/\omega = 0$ (where ω is the Gaussian driver beam half-width and y is the Cartesian coordinate along the grating normal), and the center of the driver beams are at $y/\omega = -1$. Plotted is the intensity of the overlap of the density grating modulation depth and the source beam intensity, which is proportional to the local signal beam intensity. Bright colors represent high intensities, darker colors low intensities. The color scale is chosen to make the weaker moving acoustic waves visible. The horizontal axis represents a cross section through the signal beam at a given time. Going down the vertical axis corresponds to marching forward in time. In experiments, the receiver would integrate along horizontal lines and doing so with Fig. 3.3 results in the trace in Fig. 3.1i.

The oscillations at the Brillouin frequency originate from the constructive and

destructive interference of three acoustic waves that are formed by the driver laser. The brightest streak in Fig. 3.3 represents the stationary acoustic wave which is the equilibrium solution for the induced temperature grating. It convects with the surrounding fluid to the right. It decays together with the temperature grating due to thermal diffusion. The driver laser pulse is too short for bulk fluid movements to occur. Hence, initially, the density has to remain constant. This is accomplished by two additional acoustic waves that initially cancel the stationary wave. They travel with the speed of sound (relative to the surrounding fluid) in opposite directions and show as weaker streaks symmetrically around the center streak. The hump visible in Figs. 3.1f and g represents the event when the thermal grating arrives and passes over the region of the source beam.

This velocimetry approach is expected to work for high-speed sub- and supersonic flows. Depending on the expected flow velocity and the beam diameters, crossing angle, and wavelengths, a suitable value for the offset $\overline{\eta}$ can be chosen. If the offset is chosen too small, the hump in Fig. 3.1f&g will be hidden within the early parts of the LITA signal and we expect poor accuracy. If the offset is too large, then the density gratings will have completely decayed by the time it would pass over the source beam.

3.4 Experimental Setup and Procedure

Measurements were performed in a converging-diverging, 10 mm deep 2-D nozzle. The throat cross section is 10×3 mm^2. The cross section at the exit is 10×9 mm^2 which results theoretically to a flow Mach number of $M = 2.7$ at the exit. Windows give optical access on both sides along the nozzle center line, both in the sub- and supersonic flow regime.

Fig. 3.4 shows the optical setup. A Q-switched, frequency-doubled Nd:YAG laser (Spectra Physics, GCR150-10) with a folded-BOXCARS forward phase-matching[54] optical setup is used to produce the two driver beams. Lens $L2$ ($f = 500$ mm) focuses

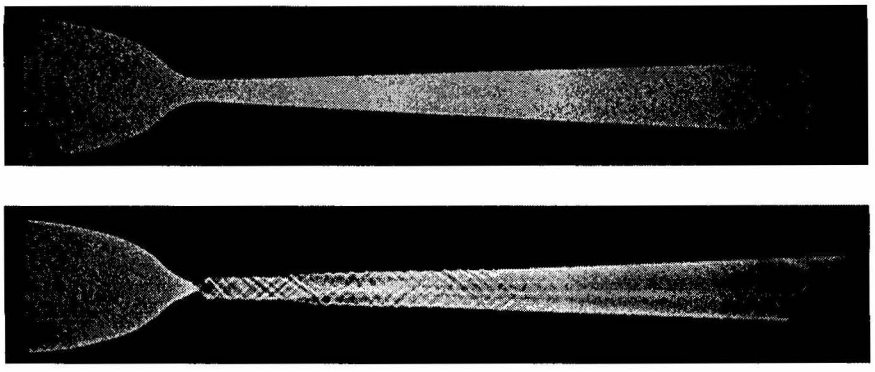

Figure 3.5: Shadowgraph of supersonic nozzle before start of flow (top) and with flow (bottom). The flow is from left to right. Mach waves of changing Mach angle indicate the presence of accelerated supersonic flow.

the parallel beams so that they intersect in the center of the nozzle cross section.

A CW Argon-Ion laser (Spectra Physics, Model 165) at 488 nm is used as interrogation laser. An offset $\overline{\eta}$ between the focus of the driver beams and the focus of the interrogation beam can be introduced by means of a micrometer-driven translation stage. The signal beam is detected by a photo-multiplier tube (Hamamatsu Model OPTO-8) and recorded on a digital storage oscilloscope (Tektronix TDS 640A). From there it is transferred to a personal computer for storage and data analysis.

The nozzle is operated as a blow down nozzle which was fed by a reservoir filled with NO_2-seeded nitrogen at 4 MPa. Running times were approx. 45 s for each run during which time single-shot measurements were taken at a rate of 3 Hz.* Fig. 3.5 shows shadowgraphs of nozzle without (top) and with (bottom) flow. We see Mach waves of decreasing Mach angle behind the throat in the bottom picture, which are typical for two-dimensional nozzles and which indicate the presence of supersonic flow. The apparent discontinuity of the nozzle contour in the throat region is due to the high density gradients around this location. Before each blow-down run the values for the driver beam crossing angle and the driver and source beam diameters

*The driver laser repetition rate is 10 Hz but the data transfer from the oscilloscope to the computer limits the data rate.

are determined by static calibration measurements.

For a fixed value of the beam misalignment $\overline{\eta} = -750$ μm measurements are performed at different positions x along the nozzle centerline. We measure x as location of the source beam. Note that due to the offset of the driver beams the grating will be created slightly upstream (lower value of x) of this position. The flow velocity will change between these two positions. This is significant for the subsonic part where the fluid accelerates from $M = 0.25$ to sonic over a distance of only 4 mm.

The Levenberg-Marquardt scheme[49] is used for a nonlinear least-squares fitting of the theoretical model described in Section 3.2 to the experimental signals. The speed of sound and the flow velocity are fitting parameters during this procedure. To limit the number of fitting parameters, other experimental parameters such as the beam crossing angles and beam diameters are determined in a calibration measurement in nearly quiescent fluid in the entry region of the nozzle (Fig. 3.6a).

3.5 Experimental Results

Fig. 3.6 shows some of the recorded LITA signals (black) and the fitted theoretical model (red). The depicted signals have been averaged over 16 individual measurements to reduce the noise levels. The signal intensities are satisfactory. It must be said, however, that the flow was heavily seeded with NO_2 (approx. 1 part in ten thousand). The signals are normalized with respect to their peak value. Similar as in Fig. 3.1 we see the tendency for the hump in the signal to move towards earlier times with increasing flow velocity, *i.e.*, the further downstream we take the measurement. Table 3.1 lists the values for the speed of sound and the flow velocities after the fitting technique has converged to a final value.

Table 3.1: Theoretical and measured c_s and u_y in supersonic nozzle.

x [mm]	M	c_s th./meas. [m/s]	u_y th./meas. [m/s]
-24	0.1	345/345 (calib.)	0/0 (calib.)
$\pm$0	1.0	317/325	317/384
+14	1.75	269/264	471/455
+23	2.0	257/259	516/467
+45	2.33	239/235	560/-

3.6 Conclusions

The values for the speed of sound in Table 3.1 agree very well with what quasi-1d flow theory predicts. Errors are only approximately 2%. The accuracy for the velocity measurements is not as good.

The 2D-nozzle is only 10 mm deep. Towards the nozzle exit the boundary layers on the windows are about 3 mm thick on both sides. This leaves only about 4 mm of undisturbed flow in between the windows. Considering that the length of the sample volume is approximately 5 mm, it is likely that parts of the sample volume reach into the boundary layer. This could explain some of the distortions in the data in Fig. 3.6 and also the large errors for the flow velocities. In particular, we expect the hump to be fairly narrow. Its shape is governed by the driver beam profile. A spreading indicates the presence of a range of velocities within the sample volume.

The current nozzle design was limited by the available mass flow rate at densities that allow good signal levels in the supersonic part of the nozzle. The signal intensity scales with the square of the density. Still, we observe phenomenological agreement between theory and experiment.

Another source of uncertainty, as mentioned, will be that the flow velocity changes along the flight path of the grating. In the present experimental setup this is particularly important near the throat where the flow accelerates from $M = 0.25$ to sonic within a distance of only 4 mm. To minimize this effect we prefer small values for the beam offset $\overline{\eta}$. But the best temporal separation of the early signal parts

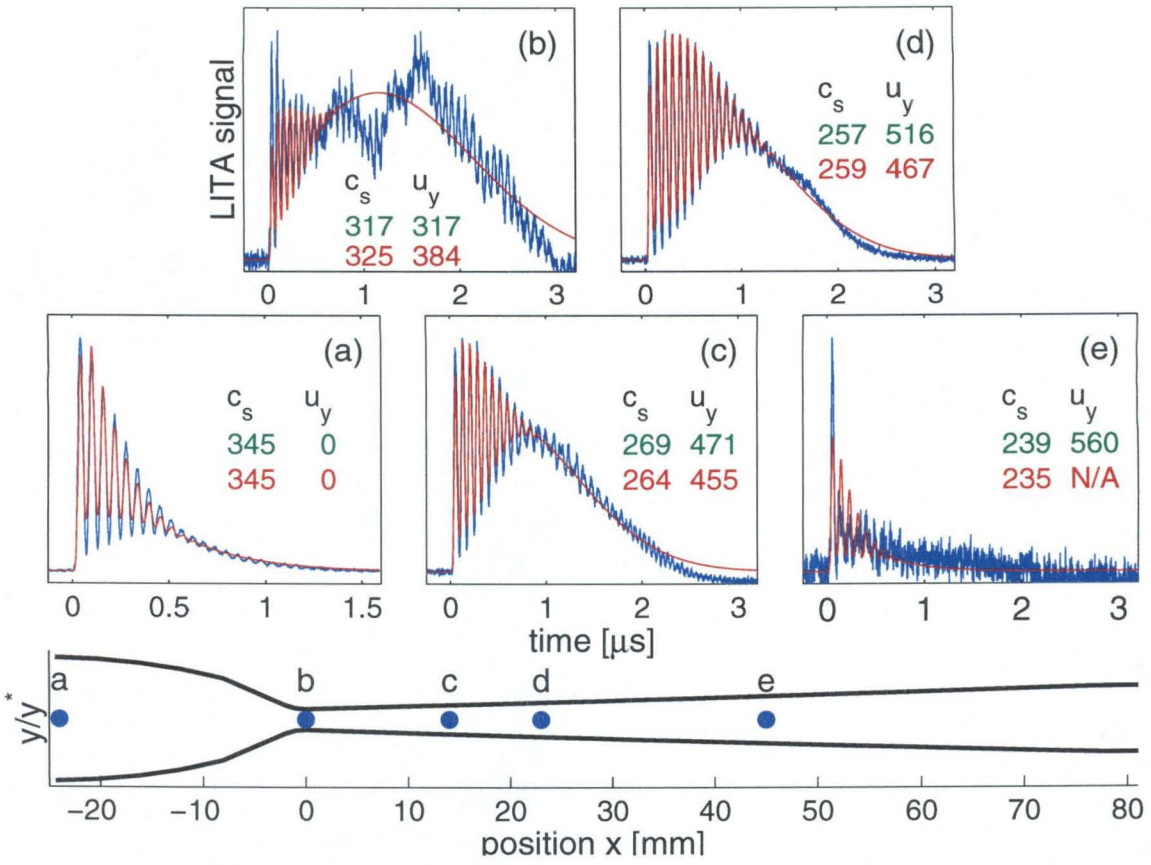

Figure 3.6: LITA signals for $\overline{\eta} = -750$ μm at different locations along nozzle centerline. Experimental data is plotted blue, fitted theoretical model is in red. The green numbers are the results from quasi-one-dimensional isentropic flow theory, the red number are the results of the data analysis. The other experimental parameters are: driver beam crossing angle $\theta = 1.48°$, driver beam half-width $\omega = 240$ μm, source beam diameter $\sigma = 1,500$ μm. The flow Mach number ranges from $M \approx 0.1$ ($x = -24$ mm) to $M = 2.33$ ($x = +45$ mm).

from the passing of the thermal grating for large $\overline{\eta}$. For applications of this technique in situations with lower velocity gradients in flow directions, this effect might be neglected.

It has been demonstrated theoretically and experimentally how Laser-Induced Thermal Acoustics can be used to simultaneously measure the speed of sound and one velocity component. The Mach number follows directly and with prior knowledge of the fluid composition, the temperature can be obtained. Still, this technique is non-intrusive (temperature perturbations of less than 1 K), remote, and instantaneous

($\approx$ 2 μs). The measurement uses only homodyne detection, which should simplify the experimental setup. The technique can be used for sub- or supersonic high speed flows. For a given set of experimental conditions (beam sizes, crossing angles, *etc.*) and range of fluid velocities, a suitable driver beam offset can be found that maximizes the effect of the fluid velocity on the signal shape and hence maximizes the accuracy of the technique. Heterodyne detection LITA velocimetry encounters problems around sonic conditions. In this case, the Doppler shift is equal to the Brillouin frequency and the two frequencies cannot be separated.[†] Homodyne detection LITA velocimetry can be used in this range. Further measurements in a larger continuous flow supersonic flow facility will yield quantitative results of this technique.

[†]If the gratings result from electrostriction then this happens at $M = 2$.

Chapter 4

LITA Velocimetry Using Heterodyne Detection

4.1 Introduction

Laser-induced thermal acoustics (or Laser-induced grating thermometry) is a four-wave mixing technique that has been successfully used for remote, non-intrusive, and instantaneous measurements of the speed of sound, the thermal diffusivity, and the fluid velocity. LITA is used by a number of laboratories for thermometry purposes,[42–44,50,55] and for velocimetry applications with electrostrictive gratings,[51] and using thermal gratings.[45] A theoretical treatment of LITA can be found in Cummings.[29] Schlamp *et al.*[36] extends the theory to include the effect of fluid velocities on homodyne-detected signals.

Heterodyne LITA velocimetry has been proposed[29] as an alternative to laser Doppler anemometry for velocity measurements in luminous flows, flows with poor optical access, and flows with poor or no control of particulates. We report on the successful application of heterodyne LITA velocimetry with $\sim 0.5\%$ uncertainty in the sound speed and velocity at Mach 0.1 from single-shot signals.

In LITA, two coherent intersecting pulsed laser beams create by thermalization and/or electrostriction a density grating in the sample volume that evolves over time. A third, continuous laser beam, directed at the Bragg angle onto the sample volume, is scattered into a coherent signal beam whose intensity depends on the instantaneous density grating modulation depth. Convective motion of the laser-induced perturba-

tions normal to the grating produces a Doppler shift in the signal that is proportional to the velocity. Heterodyne signal detection is employed to recover the Doppler shift. In this study, phase-sensitive detection is accomplished by superimposing the signal beam and a reference beam on a photomultiplier tube.

Experimental results are presented from heterodyne velocity measurements in a low speed wind tunnel using thermal gratings in NO_2 seeded air for a Mach number range $M = 0 \ldots 0.1$. Measurements were extracted from signals via optimal nonlinear filtering. The optimal nonlinear filter consists of a least-squares fit between a theoretical and experimental signal.[29] The theoretical signal used in the filter is an extension of the analysis in Schlamp *et al.*[36] for heterodyne detection with a finite frequency shift between the source and reference beams. While not used in these experiments, such a shift (*e.g.*, via a Bragg cell) could eliminate velocity ambiguity and improve the performance of the technique at low speeds.

4.2 Experimental Setup and Procedure

Experiments were conducted in a closed-circuit wind tunnel with a test section cross section of 5 cm. The tunnel was powered by a propeller mounted on an air-driven motor (350 W at 600 kPa) whose air supply and exhaust piped through the wind tunnel wall to allow closed-circuit tunnel operation. The test gas was NO_2-seeded air at atmospheric conditions.

The motor was driven by pressurized air from a blow-down reservoir that started at 600 kPa. Run times were approximately 60 s with speeds starting at $\sim$40 m/s and decreasing with the reservoir pressure. Data was taken continuously during runs at the driver laser pulse-repetition rate of 15 Hz.

A standard forward-scattering focused-beam four-wave mixing geometry was employed. The optical setup consisted of a frequency-doubled, Q-switched Nd:YAG laser (Continuum, Minilite II, 25 mJ/pulse, $3 - 5$ ns pulse duration) as driver laser. Its

beam is split in halves by a 50/50 beam splitter. An arrangement of mirrors on kinematic mounts and translation stages direct the two beams with equal optical path length parallel onto a transmitter lens ($f = 500$ mm) which focused the beams onto an intersection point in the center of the test section. The beam crossing angle was $\sim 1.3°$.

A CW Argon ion laser (Spectra Physics, Stabilite 2017 at 488 nm) produces the interrogation beam. A chopper wheel (Scitech Instruments, Optical Chopper) produces 20 μs pulses at sixty times the driver-laser pulse repetition rate. The short duration of these pulses extends the linear operating range of the detector photomultiplier tube. The timing and coordination of the lasers, data acquisition, and experiment is handled using a programmable logic and timing controller with 25-ns resolution (Labsmith LC880). A 99/1 beam splitter divides the beam into the interrogation and reference beams. A variable neutral density filter provides intensity adjustments of the reference beam. Both beams are directed parallel and path-length matched onto the transmitter lens, which focuses them on the sample volume. The distance between the beams is adjusted for optimal phase-matching. These beams intersect the plane of the two driver beams at an angle of $\sim 1.5°$.

A small fraction $< 0.01\%$ of the interrogation beam scatters off the grating into a coherent signal beam. The reference beam is carefully aligned to follow the same path as the signal beam.

In the receiver, the signal/reference beam pass through an interference filter and are focused by a 40-mm-f.l. lens through a 200 μm-diameter pinhole to suppress incoherently scattered and ambient light. A photomultiplier tube (Hamamatsu, H5783-03, 0.65 ns response time) detects the signal which is recorded onto a digital storage oscilloscope (Hewlett Packard, Infinium, 4 channels, 500 MHz, 2 GSa/s) and transferred to a Pentium II-based computer for storage and data analysis.

Each signal consists of a sequence of $1,024$ 12-bit samples recorded at a sampling rate of 250 MHz. During each wind tunnel run, $1,000$ single-shot signals were

recorded at 15 Hz. The experimental traces were optimally filtered using a Levenberg-Marquardt-based[49] least-squares fit to theory where the flow velocity, the speed of sound, and the phase shift between the reference and signal beams were fitting parameters. Other parameters, such as the beam diameters and driver beam crossing angle were determined in static calibration measurements.

4.3 Results

Fig. 4.1 shows examples of experimental heterodyne LITA signals and the best-fit theoretical signals. The theoretical signals are plotted with an offset for clarity. The agreement with theory is exceptionally good. Fig. 4.1a was obtained before turning on the wind tunnel, Fig. 4.1b represents approximately the maximum velocity. The velocity decreases gradually from Fig. 4.1b to Fig. 4.1f. The second frequency component in the data from the Doppler shift of the signal beam is clearly evident.

Fig. 4.2 shows velocity measurements (top trace) and sound-speed measurements (bottom trace) during a 60-s blow-down run of the wind tunnel. The inferred flow velocity before the wind tunnel is turned on non-zero because of signal distortion produced by small detector gain nonlinearities. This problem can be eliminated by the use of a frequency offset between the reference and interrogation beams. The standard deviation of the velocity measurements is ~ 0.2 m/s. The standard deviation in the sound speed measurements is 0.5%.

In Fig. 4.3 the scatter around a linear regression (dashed line in top graph of Fig. 4.2) to the flow velocity for $t \geq 3$ s is plotted as a function of the flow velocity which can be used as an estimate for the uncertainty. Data for $t < 3$ s the wind tunnel might have been influenced by startup velocity fluctuations. We see that the uncertainty is inversely proportional to the flow velocity, *i.e.*, Doppler shift.

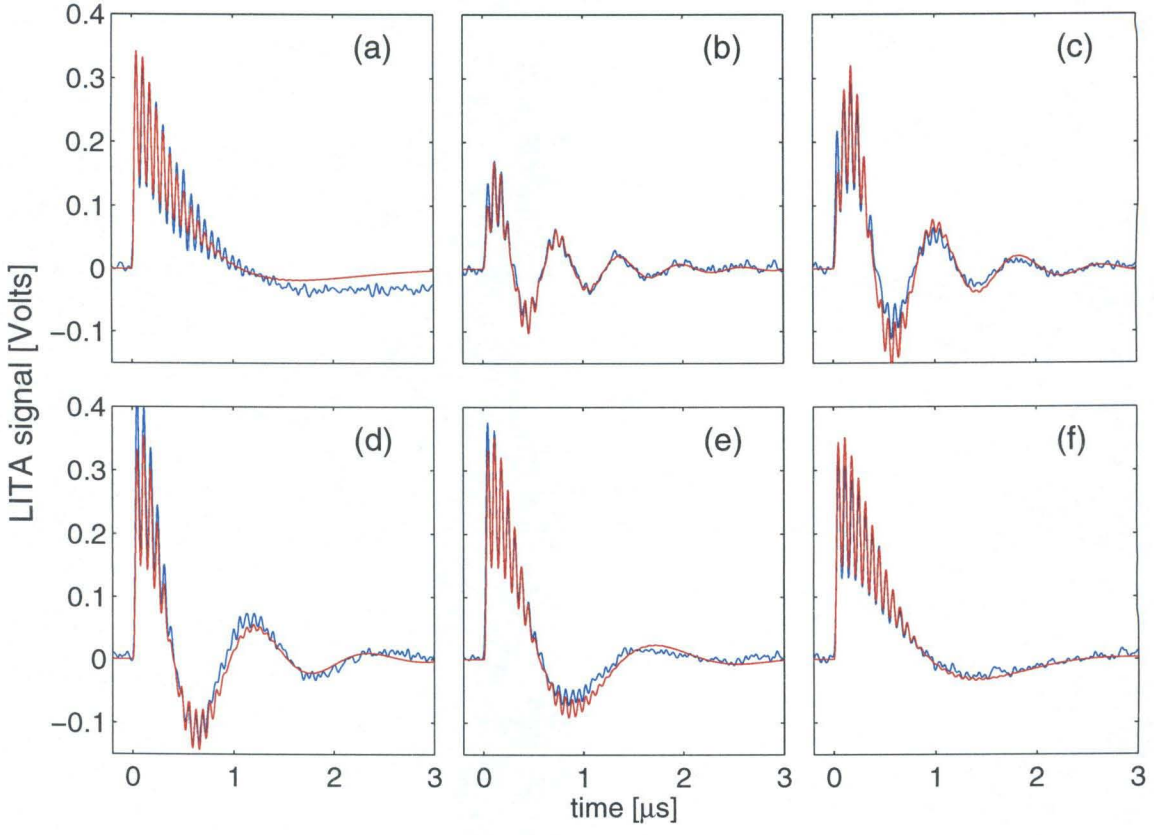

Figure 4.1: Experimental (blue) and theoretical (red) heterodyne LITA signals from Eqn. 5.6 for thermal gratings in atmospheric air. a) $M = 0.00$; b) $M = 0.11$; c) $M = 0.08$; d) $M = 0.06$; e) $M = 0.04$; f) $M = 0.02$.

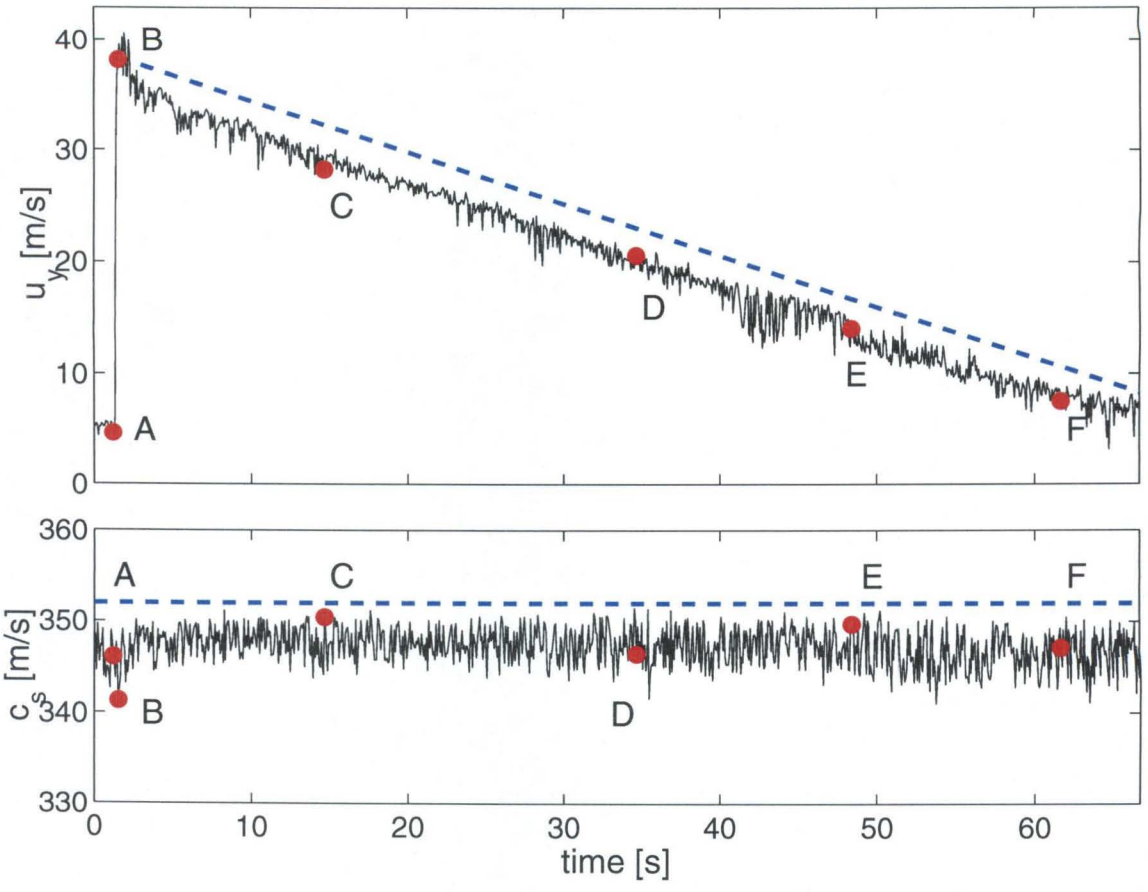

Figure 4.2: Measured flow velocities during blow-down experiment (top) and values for the speed of sound (bottom). The points labeled A-F correspond to the data in Fig. 4.1a-f. The dashed lines are linear regressions of the data that are shifted for clarity. They are used to estimate the measurement uncertainty.

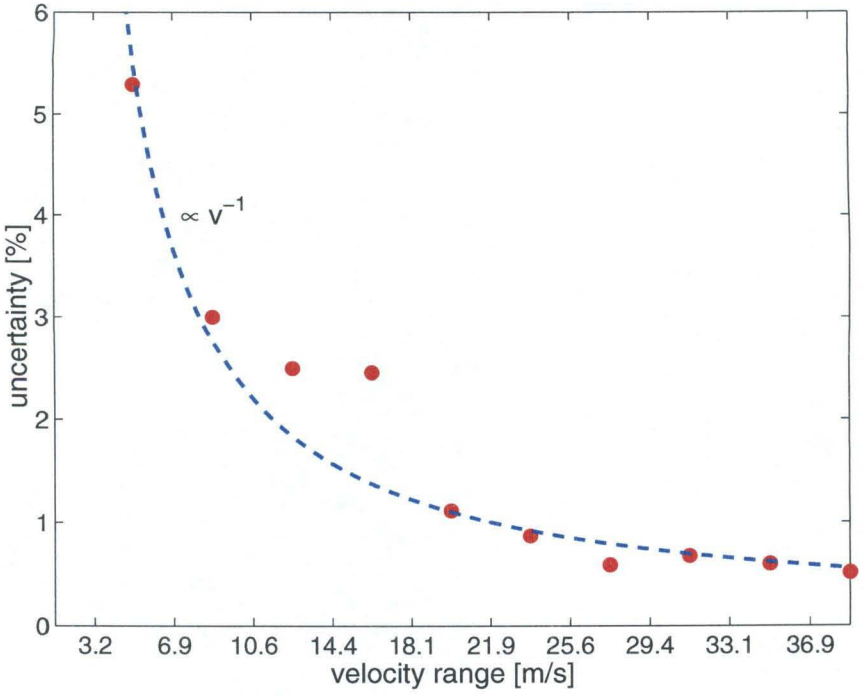

Figure 4.3: Uncertainty of velocity measurement *vs.* velocity.

4.4 Discussion and Conclusions

Single-shot heterodyne LITA signals have been recorded in a wind tunnel. The theory based upon linear hydrodynamics and scattering agrees well with the experimental signals. From these signals, the sound speed and flow velocity were inferred simultaneously with ~ 0.2 m/s and 0.5% repeatability, respectively. The signal lifetime sets a lower limit on the flow velocity that can be measured accurately. For example, in Fig. 4.1f, the period of the Doppler shift is about the same as the signal life time. For the highest flow velocities measured (~ 40 m/s), the accuracy of the measurements was $\sim 0.5\%$. At low velocities, gain variations in the PMT over the lifetime of the signals produced a large (consistent) velocity error of ~ 5 m/s. This error could be mitigated by characterizing the PMT response and removing the defects as best as possible from the signals. However, many effects produce low-frequency variations in a detected signal. Untreated, these effects produce flicker or $1/f$ noise. Because of the practical impossibility of correcting for all these effects, we propose to use a

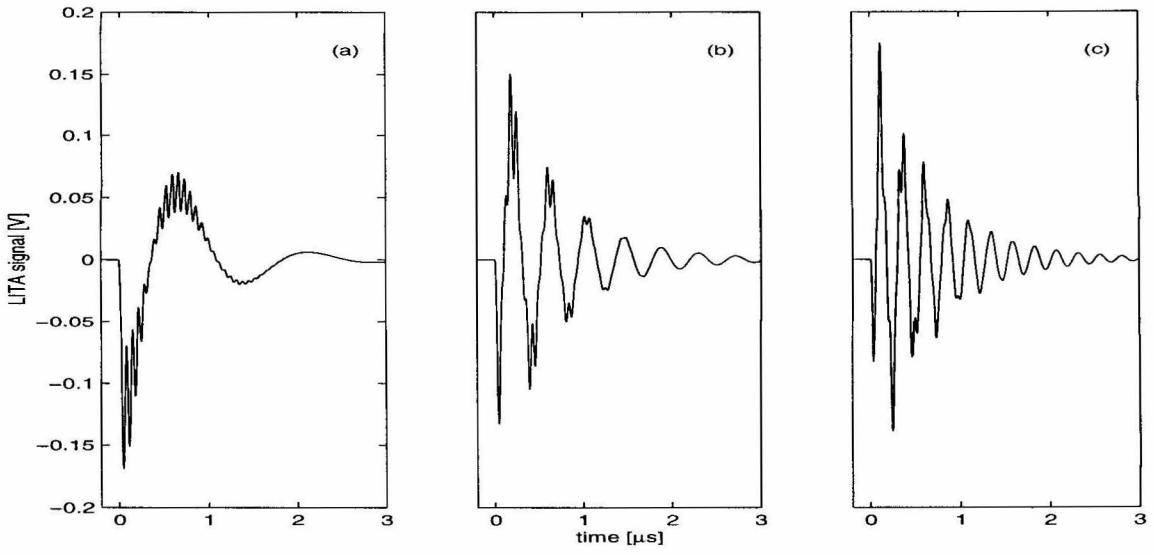

Figure 4.4: Theoretical traces for varying velocities with frequency shift $\Delta f_{ref} = -15$ MHz. a) $v = -40$ m/s; b) $v = 0$ m/s; c) $v = +40$ m/s.

Bragg cell in the path of the reference beam to shift its frequency by $O(100$ MHz) (c.f. typical LDA implementations). This frequency offset will appear in the signal, up- or down-shifted by the Doppler frequency, depending upon the direction of the motion of the fluid. By this up-conversion of the Doppler frequency, reduces the $1/f$ noise significantly for all practical velocities, eliminating large velocity errors at low speeds. The up-conversion also removes ambiguity in the sign of the velocity measurement. Fig. 4.4 demonstrates this approach. It is equivalent to the use of a rotating mirror in Particle-Image Velocimetry.[56]

Heterodyne LITA velocimetry should be applicable well into the hypersonic range of velocities. It has advantages over LDA when optical access is limited, the flow is luminous, particulate content is not easily controlled, particle lag is excessive, and where additional simultaneous information about the flow is desired, such as the sound speed, thermal diffusivity, or their derived quantities, the temperature and density. LITA velocimetry also produces measurements with microsecond temporal resolution, a factor in pulsed or highly unsteady flows. The disadvantages of the technique over LDA are the additional complexity and the need for more powerful lasers.

Chapter 5

Neural Network Data Analysis for LITA

5.1 Introduction

While other laser-diagnostic techniques such as Particle Image Velocimetry and Laser Doppler Anemometry are commercially available as packages systems, this is not true for Laser-Induced Thermal Acoustics (LITA). One of the reasons is the complexity of the optical setup and alignment for LITA. Secondly, the characteristic advantages of LITA (short test times, high signal levels, non-intrusiveness) only play a significant role for a small number of specialized applications. Finally, the data analysis can be cumbersome and requires user input, interaction, and expertise to ensure the integrity of the results. Latter point is the focus of this paper. We seek a method that performs the data analysis accurately, computationally efficiently, robust, and autonomously. We propose and demonstrate the use of a feed-forward neural network for this task.

Laser-induced thermal acoustics (or Laser-induced grating thermometry) is a four-wave mixing technique that has been successfully used for remote, non-intrusive, and instantaneous measurements of the speed of sound,[42] the thermal diffusivity,[42] and the flow velocity of gases.[37,38,45,51] If the gas composition is known, the temperature can be obtained from the speed of sound.[44,50,51,57]

Two coherent intersecting pulsed laser beams (excitation beams) create by thermalization and/or electrostriction a density and consequently a refractive index grating in the sample volume that evolves over time. A third, continuous laser beam (interrogation beam), directed at the Bragg angle onto the sample volume, is scattered into a coherent signal beam whose intensity depends on the instantaneous modulation

depth of the refractive index grating.

Two detection approaches can be used. In homodyne detection, only the signal beam intensity is recorded over time. In heterodyne detection, the superposition of the signal beam and a reference beam is recorded. Since the signal beam has a Doppler shift proportional to the fluid velocity component along the grating normal direction, the latter approach makes this Doppler shift visible in the recorded signal.

Given the time-resolved heterodyne or homodyne signal, one of three methods is currently employed to obtain the speed of sound and, in the case of heterodyne detection, the fluid velocity.

- One can use a technique where a signal obtained from a theoretical model is used for a nonlinear least-squares fit to the experimental data. The speed of sound and flow velocity are floating parameters during the fitting. This technique requires a theoretical model. Cummings *et al.*[29] and Schlamp *et al.*[36] provide such a model. The theory in those references assumes, however, homodyne detection.

- Pronys method[50,58] is a simpler version of the fitting technique above. A linear combination of damped complex potentials is fitted to the data. No theoretical method is needed.

- From the location of the peaks in the power spectrum, one can infer the Brillouin frequency and the Doppler frequency. The speed of sound and the flow velocity can be deduced.

Previous research[29,42] has shown that LITA can also be used to measure the thermal diffusivity. The thermal diffusivity governs the exponential decay of the LITA signal. Hence, from the decay time constant of the LITA signal, the thermal diffusivity can be calculated. But the last two methods can only extract frequencies from the data. Only the first method is capable of extracting signal parameters other than frequencies from signals. While the full fitting technique is computationally expensive ($\mathcal{O}(n^3)$, where

n is the number of data points in a signal), it is more accurate than the frequency decomposition technique as it represents an optimal filter for the noisy data under the assumption that the theoretical model is a correct representation of the experimental signal. The frequency decomposition technique is computationally cheap ($\mathcal{O}(n \log n)$) and can be performed in real-time at driver laser frequencies of $\mathcal{O}(10$ Hz).

Artificial neural networks are heavily used for all sorts of classification problems,[59,60] robot control,[61,62] speech recognition,[63,64] and image processing[65] but less extensively for data analysis in engineering problems. This is mostly due to a lack of familiarity of the engineering community with the concepts of neural networks. Secondly, the lack of analytical tools for an a priori prediction of the network performance, optimal learning algorithms, amount of training necessary, or for guiding in the design of the network architecture is another point of dissatisfaction. Finally, while it is possible that a trained neural network gives accurate results for all inputs tested, it is impossible to *prove* that this will be the case for all inputs.

We use only very basic neural network concepts to achieve the results presented in Section 2.9. This demonstrates that even simple neural network implementations can yield very satisfactory results. Excessive empirical trial-and-error with network architecture and learning scheme can potentially improve the network performance and accelerate the training process, but this is not necessary to arrive at satisfactory results. The disadvantage of the neural network implementation presented in this paper is the requirement to train the neural network prior to its use. Without advanced numerical schemes this can take considerable time. It should be pointed out that the trained network performs the data analysis fully autonomously. The neural network outputs are direct functions of the network inputs so that numerical instability or poor convergence behavior do not pose a problem.

In Section 5.2 we will present the theoretical framework for LITA using either heterodyne or homodyne detection. It is an extension of the work presented in Cummings *et al.*[29] and Schlamp *et al.*[36] The solution will be used to create a set of LITA

traces which are used to train a neural network and to test its performance. In Section 5.3 we will present a summary of the basic theory of feed-forward neural networks and the back-propagation learning rule. This section should provide just enough information for the reader who is unfamiliar with neural networks to follow this paper. For more background information, the interested reader is directed to Hertz *et al.*,[66] Bishop,[67] and Haykin.[68] Section 5.4 shows how the theory of feed-forward networks can be implemented for the LITA data analysis. Section 5.5 gives some results of the theoretical derivation from Section 5.2 and will show the performance of the neural network data analysis.

5.2 LITA Theory

The electric field of the scattered LITA signal beam in Fourier space is[36]

$$\frac{\mathsf{E}_s(\vec{q},\vec{R},t)}{P_0(t)} = -\frac{k_s^2\omega^2}{4\pi R}\chi(f_0)\exp\left\{i\left(\vec{k}_s\cdot\vec{R}-f_0t\right)\right\} \circ \Re\left[A_{P1}\Phi_{P1}^{(d,0)}+A_{P2}\Phi_{P2}^{(d,0)}+A_T\Phi_T^{(d,0)}+A_D\Phi_D^{(d,0)}\right]. \quad (5.1)$$

$A_{P1,P2,T,D}$ are the relative amplitudes of the acoustic waves, thermal grating, and finite driving-time terms. $\Phi_{P1,P2,T,D}$ contain the temporal and spatial profiles of these terms. $\circ$ represents a temporal convolution. Eqn. 5.1 contains the effects of finite beam sizes, single-rate thermalization, and electrostriction. For a more detailed explanation of the terms in Eqn. 5.1, the reader is directed to Cummings *et al.*[29] and Schlamp *et al.*[36]

We superimpose a reference beam with the same Gaussian geometry and direction

as the signal beam of the form

$$\mathsf{E}_{ref} = \mathsf{E}_r + \mathsf{E}_r^* \tag{5.2a}$$

$$\mathsf{E}_r = \frac{A}{2} \exp\left\{i\vec{k}_s \cdot \vec{R} - i(f_0 - \Delta f_{ref})t + i\tilde{\phi}\right\} \exp\left\{-\left|\frac{\hat{e}_0 \otimes \vec{r}}{\sigma}\right|^2\right\} \tag{5.2b}$$

to the signal beam. f_0 is the interrogation beam frequency, σ its diameter, and k_s its wave vector magnitude. $\otimes$ and $()^*$ denote the vector cross product and the complex conjugate, respectively. $\tilde{\phi}$ is used to model a phase shift between the reference beam and the signal beam. In the final result (Eqn. 5.6), $\tilde{\phi}$ produces a phase shift between the Brillouin frequency and the Doppler frequency component in the signal (Fig. 5.5). This effect was observed experimentally[38] where $\tilde{\phi}$ took random values for every signal. This is caused by small time-varying perturbations (*e.g.*, vibrations) in the optical setup. The frequency of the reference beam is assumed to be shifted by Δf_{ref} from that of the interrogation beam. In experiments, this frequency shift could be introduced by a Bragg cell in the beam path. Its purpose is to improve the accuracy for low speed velocity measurements and to remove the direction ambiguity from the velocity measurements.

For the time being, we do not specify the (temporally constant) intensity of the reference beam relative to the signal beam and use the prefactor A to keep Eqn. 5.2 general. Furthermore, we will absorb any multiplicative constants that will show up along the way into A. For $A = 0$, *i.e.*, zero reference beam intensity, we expect to recover the result for homodyne detection.

Since the Fourier transform is a linear operation, we can superimpose the Fourier transform of Eqn. 5.2a directly with Eqn. 5.1. The Fourier transform of Eqn. 5.2a is:

$$\mathsf{E}_{ref}(\vec{q}, t) = A_{ref}\Phi_{ref} \exp\left\{i(\vec{k_s} \cdot R - f_0 t)\right\} \tag{5.3a}$$

where

$$A_{ref} = A \exp\left\{i\tilde{\phi}\right\} \tag{5.3b}$$

$$\Phi_{ref} = \Sigma_{ref}\Psi_{ref} \tag{5.3c}$$

$$\Psi_{ref} = \exp\left\{-\frac{\sigma_y^2}{4}\left(q_y - q_\psi\right)^2 - \frac{\sigma_z^2}{4}q_z^2\right\} \tag{5.3d}$$

$$\Sigma_{ref} = \exp\left\{i\Delta f_{ref} t\right\} \tag{5.3e}$$

$$\sigma_y = \frac{\sigma}{\sin\psi} \qquad \sigma_z = \sigma \tag{5.3f}$$

and where q_ψ is the phase-matched scattering or grating vector. Note that in Eqn. 5.3d we neglected a second lobe centered at $q_y = -q_\psi$ as well as any variations in x-direction. The latter is justified by the fact that for small driver beam crossing angles, the spatial extent of the grating will be much larger in the x-direction than in the y- or z-directions.

Now we can superimpose signal and reference beam by including Eqn. 5.3a in Eqn. 5.1 as follows:

$$\frac{\mathsf{E}_s(\vec{q},\vec{R},t)}{P_0(t)} = -\frac{k_s^2\omega^2}{4\pi R}\chi(f_0)\exp\left\{i\left(\vec{k}_s\cdot\vec{R} - f_0 t\right)\right\} \circ \Re\left[A_{P1}\Phi_{P1}^{(d,0)} + A_{P2}\Phi_{P2}^{(d,0)} + A_T\Phi_T^{(d,0)} + A_D\Phi_D^{(d,0)} + A_{ref}\Phi_{ref}\right] \tag{5.4}$$

Detectors measure the intensity of the electric field, *i.e.*, the square of the modulus of Eqn. 5.4. Also, at this point we assume that the driver laser pulse is short compared to all other time scales and that we can approximate it by a Dirac delta function. This simplifies the temporal convolution into a simple multiplication.

Hence, the signal intensity using heterodyne detection is then

$$\mathcal{L}_{het} \propto \left(A_{P1}\Phi_{P1}^{(d,0)} + A_{P2}\Phi_{P2}^{(d,0)} + A_T\Phi_T^{(d,0)} + A_D\Phi_D^{(d,0)} + A_{ref}\Phi_{ref}\right) \times \left(A_{P1}^*\Phi_{P1}^{(d,0)*} + A_{P2}^*\Phi_{P2}^{(d,0)*} + A_T\Phi_T^{(d,0)*} + A_D\Phi_D^{(d,0)*} + A_{ref}^*\Phi_{ref}^*\right) \tag{5.5}$$

Finally, we have to integrate Eqn. 5.5 over the detector area. In the limit of a small detector, we can multiply Eqn. 5.5 by the detector area. In the limit of a large detector we can use infinite spatial integrals of Eqn. 5.5. In the latter case, the result is

$$\begin{aligned}
\mathcal{L}_{het} \propto \Bigg[& \exp\left\{-\frac{8\sigma_y^2}{Y^2\left(Y^2+2\sigma_y^2\right)}\left(\frac{c_s t}{2}\right)^2\right\}\left[(P_1+P_2)(T^*+D^*)+(P_1^*+P_2^*)(T+D)\right] \\
& + \exp\left\{-\frac{8\sigma_y^2}{Y^2\left(Y^2+2\sigma_y^2\right)}\left(c_s t\right)^2\right\}\left(P_1P_2^*+P_1^*P_2\right) \\
& + \exp\left\{-\frac{8\sigma_y^2}{\left(Y^2+2\sigma_y^2\right)\left(Y^2+\sigma_y^2\right)}\left(\frac{\overline{\eta}+vt}{2}\right)^2\right\}\left[\left(T+D\right)R^*+\left(T^*+D^*\right)R\right] \\
& + \exp\left\{-\frac{8\sigma_y^2}{\left(Y^2+2\sigma_y^2\right)\left(Y^2+\sigma_y^2\right)}\left(\frac{\overline{\eta}+(v+c_s)t}{2}\right)^2\right\}\left(P_1R^*+P_1^*R\right) \\
& + \exp\left\{-\frac{8\sigma_y^2}{\left(Y^2+2\sigma_y^2\right)\left(Y^2+\sigma_y^2\right)}\left(\frac{\overline{\eta}+(v-c_s)t}{2}\right)^2\right\}\left(P_2R^*+P_2^*R\right) \\
& + \left(P_1P_1^*+P_2P_2^*+TT^*+TD^*+T^*D+DD^*+RR^*\right)\Bigg] \qquad (5.6)
\end{aligned}$$

where $P_1 = A_{P1}\Sigma_{P1}$, $T^* = A_T^*\Sigma_T^*$, $R = A_{ref}\Sigma_{ref}$, *etc.* The term RR^* at the very end of Eqn. 5.6 represents the constant reference beam intensity in the form of a DC offset. We see that for $A = 0$ ($A_{ref} = 0$), the solution collapses onto the solution for homodyne detection.[36] Since we do not attempt to find an expression for the *absolute* LITA signal intensity we, as in Eqn. 5.5, neglect multiplicative constants.

5.3 Neural Network Formulation

Multi-layer feed-forward networks were first studied by Rosenblatt in the late 1950s[69] but, owing to the absence of a training algorithm for multi-layer networks, interest subsided until the reporting of the back-propagation learning rule in 1986.[35] Back-propagation has actually been independently discovered at least three other

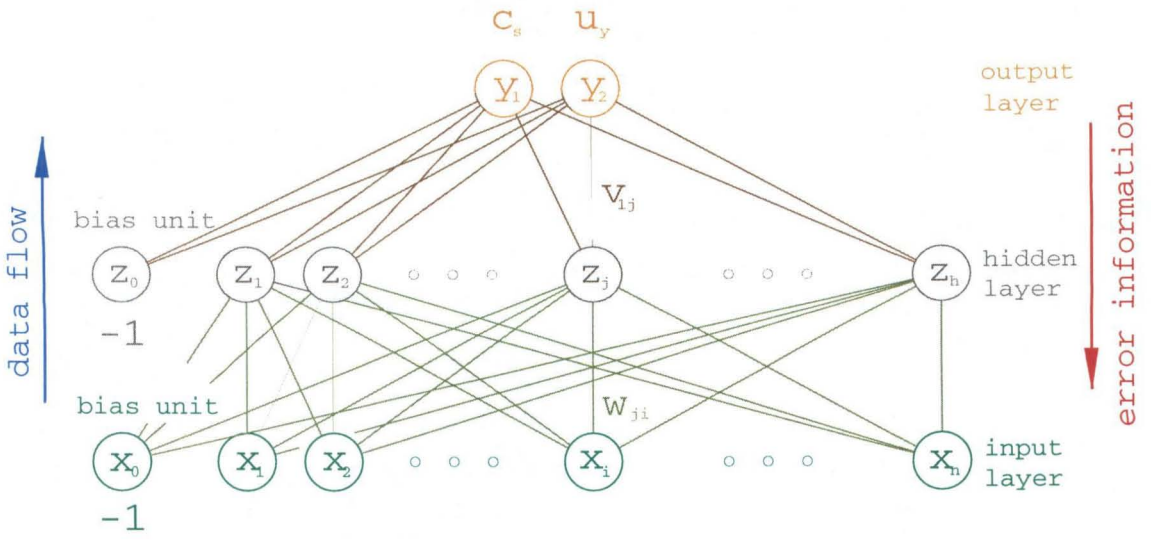

Figure 5.1: Layout of a one-hidden-layer feed-forward neural network illustrated for the case of $m = 2$ output units.

times.[32–34,70] Bryson *et al.*[32] refers to work done, on a related problem, in the early 1950s.[71]

The network we are considering (Fig. 5.1) has n input units x_i, $i = 0 \ldots n$, h units z_j in the hidden layer, $j = 1 \ldots h$, and m output units y_k, $k = 1 \ldots m$. Each unit is connected to every unit in the next higher layer. A weight is assigned to each such connection. A normalized, time-discretized LITA signal $\mathcal{L}(t_i)$ will be used as input. So, n will be chosen to be the number of points in the signal trace.

The values z_j of the units in the hidden layer are determined by the values of the input units, the weights w_{ji} (from input unit i to hidden unit j), and an activation function $\sigma(.)$ by

$$z_j = \sigma\left(\sum_{i=0}^{n} w_{ji} x_i\right). \tag{5.7}$$

Note that the index counts from zero to n and we define $x_0 = -1$ and call it a bias unit. Its significance Hertz *et al.*[66] lies in its mathematical and algorithmic

convenience. It allows an affine transformation of the inputs (*i.e.*, one involving a linear combination of inputs $a_1x_1 + a_2x_2 + \ldots$ plus an offset a_0) to be treated as a linear combination; thus, all weights, including a_0, may be treated uniformly, rather than requiring separate treatment for a_0.

Similarly, the values of the output units are given by

$$y_k = \sigma\left(\sum_{j=0}^{h} v_{kj} z_j\right), \tag{5.8}$$

where $\sigma(.)$ is the same activation function as before, $z_0 = -1$, and v_{kj} is the weight from hidden unit j to output unit k. The only requirements for the activation function $\sigma(.)$ are that it is nonlinear, differentiable and bounded. Hidden layers do not expand the network's capabilities if the activation function is linear. This is because any linear combination of linear functions is again only a linear function. The requirement that $\sigma(.)$ is differentiable is due to the back-propagation learning rule. The boundedness of $\sigma(.)$ is not a strict requirement but it is helpful in avoiding overflows. We use

$$\sigma(x) = \frac{1}{1 + \exp(-x)}, \tag{5.9}$$

but other choices such as $\sigma(x) = \tanh(x)$ are possible.

Each output unit represents one parameter that we want to filter from the LITA signal in the input. By the choice of the activation function (Eqn. 5.9), the output units can only have values in the range $0 \ldots 1$ and we must therefore scale the outputs to fall in the range of the target values, *i.e.*, speed of sound and flow velocity (see Eqns. 5.16a & b).

We see that, given the proper weights w_{ji} and v_{kj}, and a LITA signal as input, the y_k's can easily be found. The problem is to find the correct weights that perform the filtering correctly. This process is referred to as training of the neural network.

Assume we have a number $\mu = 1 \ldots N$ of LITA signals (training set) with known

correct output values η_k^μ (called target values) but the network with incorrect weights returns values at the output units y_k^μ. One possibility to define an error measure is by

$$E = \frac{1}{2} \sum_{\mu=1}^{N} \sum_{k=1}^{m} \left(y_k^\mu - \eta_k^\mu\right)^2 . \tag{5.10}$$

This represents the sum of the squares of all individual errors. E is zero if and only if $y_k^\mu = \eta_k^\mu$ for all k and μ. By using Eqns. 5.8 and 5.9 in Eqn. 5.10 we can differentiate with respect to the weights v_{kj} and obtain

$$\frac{\partial E}{\partial v_{kj}} = \sum_{\mu=1}^{N} \left(y_k^\mu - \eta_k^\mu\right) y_k^\mu \left(1 - y_k^\mu\right) z_j^\mu . \tag{5.11}$$

The choice of the activation function in Eqn. 5.9 allows us to express $d\sigma/dx$ by $\sigma(x)$ itself,

$$\frac{d\sigma(x)}{dx} = \sigma(x)(1 - \sigma(x)). \tag{5.12}$$

This has the advantage that we do not have to compute $\sigma\prime$ during the training.

We can continue, use Eqn. 5.7 in Eqn. 5.11, and differentiate with respect to the weights w_{ji}. The result is

$$\frac{\partial E}{\partial w_{ji}} = \sum_{\mu=1}^{N} x_i^\mu \sum_{l=1}^{m} v_{lj} z_j^\mu \left(1 - z_j^\mu\right) \left(y_l^\mu - \eta_l^\mu\right) y_l^\mu \left(1 - y_l^\mu\right) . \tag{5.13}$$

This gives us all the tools we need. By updating the weights according to

$$\begin{aligned} \Delta w_{ji} &= -\eta \frac{\partial E}{\partial w_{ji}} \\ \Delta v_{kj} &= -\eta \frac{\partial E}{\partial v_{kj}} \end{aligned} \tag{5.14}$$

where η is called the learning rate, the error measure E can be reduced iteratively

provided η is sufficiently small. Eqn. 5.14 represents the method of steepest descent. More sophisticated updating rules than the one shown in Eqn. 5.14 can be used which show faster convergence, *e.g.*by introducing a "momentum" term[66]

$$\Delta w_{ji}(t+1) = -\eta \left.\frac{\partial E}{\partial w_{ji}}\right|_t + \alpha \Delta w_{ji}(t-1)$$
$$\Delta v_{kj}(t+1) = -\eta \left.\frac{\partial E}{\partial v_{kj}}\right|_t + \alpha \Delta v_{kj}(t-1). \tag{5.15}$$

α must be between 0 and 1. Commonly a value of 0.9 is chosen.

Some authors[66,72–75] have proposed an adaptive scheme of adjusting the parameters α and η during the training to further improve the convergence behavior. In most adaptive schemes η is increased by a small additive constant if the cost function E decreases monotonically over a number of iterations. An increase of E during the training, on the other hand, normally indicates that the minimization algorithm overshot the minimum and a reduction in step size is appropriate. Hence, if E increases over one training iteration, η is decreased geometrically (*i.e.*, multiplied by a constant between zero and one).

As stated in Section 2.7, however, we change the training set slightly after every iteration to prevent the network from over-training. This introduces noise which in turn prevents us from using such an easy adaptive scheme. Due to the high number of connections (50,000+), we cannot use a more efficient (but memory demanding) minimization scheme, such as the Levenberg-Marquardt algorithm.

Hence, we know what values to use for n, m, x_i, how to calculate y_k, and how to find appropriate weights. The number of hidden units required cannot be precisely determined a priori but has to be found empirically. It can be shown[76,77] that given a sufficient number of hidden units, a one-hidden-layer feed-forward network is capable of approximating a function to arbitrary accuracy either if the function consists of a finite collection of points or if it is continuous and defined on a compact domain.*

*Similarly, a two-hidden-layer feed-forward neural network is capable of approximating *any*

From the derivation in Section 5.2 we can conclude that such a continuous function exists and that hence a one-hidden-layer network architecture is sufficient. A rule of thumb applicable to many problems is the geometric pyramid rule. According to this rule, the number of units follows a pyramid shape, with the number decreasing from the input towards the output. For a one-hidden layer network with n input units and m output units, the number of hidden units would be $\sqrt{mn}$. In practice, one should try first with a small number of hidden units and increase the number until the neural network performance is acceptable. While a two-hidden-layer network could still be used, practice shows that learning slows dramatically when more hidden layers are used.[78] The reasons for this are that the gradient becomes more unstable and that the number of local minima increases dramatically.

Two kinds of errors can be defined. The "bias" is the part of the error which is due to deficiencies in the network architecture, *i.e.*, insufficient number of layers or of hidden units. If the number of hidden units h is too large on the other hand, the network will learn the task "too" well, meaning that it will specialize on the training set but will perform poorly on data that was not used in the training phase. This is referred to as over-training. The "variance" is the part of the error that is due to the fact that the training set does not cover the entire space of inputs.

5.4 Setup

If for a given application the range of target values for c_s and u_y is known ($\tilde{\phi} = 0 \ldots 2\pi$ always), we can create a training set by using uniformly distributed random values for these parameters in Eqn. 5.6. Fig. 5.2 shows a typical trace as it was used in a training set. Each trace consists of $1,000$ equally spaced time-discretized points. As only a preprocessing step, all signals are normalized to a (positive) peak value of unity. The training set has to consist of a sufficient number of traces in order to cover

function.

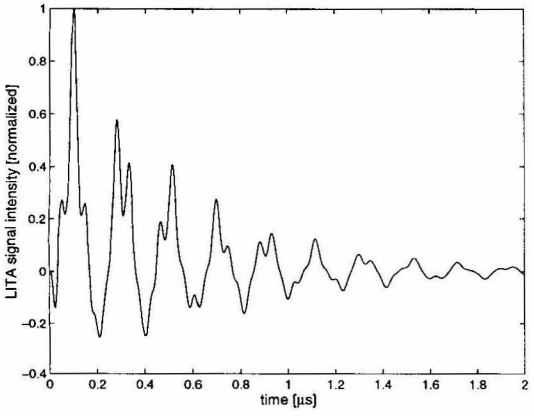

Figure 5.2: Typical theoretical trace as used in the training and validation set for $c_s = 340$ m/s and $u_y = 100$ m/s.

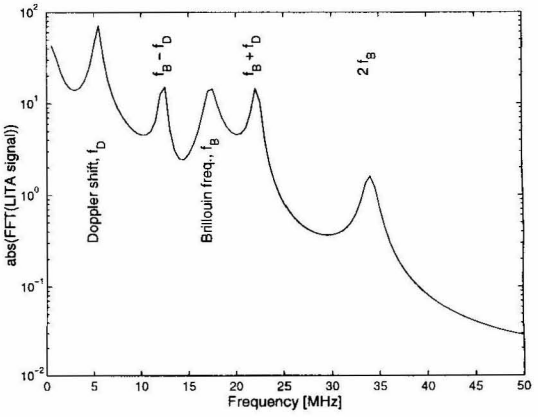

Figure 5.3: Frequency decomposition of LITA signal from Fig. 5.2.

the parameter space well (*i.e.*, to reduce the variance) and to avoid over-training of the network. In general the number of training signals should be much larger than the number of units in the hidden layer. To avoid an excessively large training set, the authors chose to vary the training set over the course of the training. After each updating of the weights, one randomly picked trace from the training set was replaced by a new trace with new random values for u_y and c_s. This procedure ensures good coverage of the input parameter space while limiting the size of the training set at any one time. In addition, this scheme introduces noise into the minimization procedure. This helps to prevent the minimization from converging to a local minimum rather than to the global minimum.

As a test case, we consider atmospheric air at rest which is accelerated isentropically to $M = 0.9$. Hence, we would expect to measure sound speeds in the range $c_s = 320 \ldots 345$ m/s, and flow velocities $u_y = 0 \ldots 288$ m/s. The phase shift $\tilde{\phi}$ is a random variable out of the range $0 \ldots 2\pi$. The experimental parameters in Eqn. 5.6 such as laser wavelengths, excitation beam crossing angle, and beam half-widths are set to typical values. Instead of using c_s and u_y directly as values for η_k^μ, these values have to be scaled to fall into the range $0 \ldots 1$. This is necessary because the range of outputs of the neural network is limited by the choice of the activation function to

be $0 \ldots 1$, where 0 and 1 are approached asymptotically. By using the scaling

$$\eta_1^\mu = \frac{1}{2}\left(\frac{c_s^\mu - 320}{345 - 320} + \frac{1}{2}\right) = 0.25 \ldots 0.75 \tag{5.16a}$$

$$\eta_2^\mu = \frac{1}{2}\left(\frac{u_y^\mu}{288 - 0} + \frac{1}{2}\right) = 0.25 \ldots 0.75 \tag{5.16b}$$

we retain comparable network sensitivities over the full range of sound speeds and flow velocities. Furthermore, since the error measure in Eqn. 5.10 minimizes the sum of the total errors rather than the sum of the relative errors, the difference between these two error measures is reduced. It would be possible to adjust Eqn. 5.10 such that the relative errors are minimized but, as we will show later, minimizing for absolute errors avoids problems with the Fourier limit at very low flow speeds. The scaling also avoids favoring output variables with larger variability which would otherwise dominate the error sum. Finally, by scaling all output variables to a fixed range, the scaling of the weights will be comparable for both output variables. In practice, this has numerical advantages.[78]

The representation of the inputs can have a significant effect on the network.[66] *E.g.*, assume we have a preprocessor that computes the correct speed of sound and flow velocity which are then used as network inputs. Instead of this trivial case, it is conceivable to use the power spectrum of the LITA signal as input, or to apply a noise filter on the data first. Each of these preprocessors can change the network performance and the number of required hidden units. We chose to use the time-discretized LITA signal as network input directly. As only preprocessing step, all signals were normalized to a positive peak value of unity.

The training was performed over up to $1.5 \cdot 10^6$ iterations with a fixed learning rate of $\eta = 0.0075$ and $\alpha = 0.9$. The training was stopped when E stopped decreasing. The number of hidden units was set to the values $h = 5, 10, 20, 50$.[†] The weights w_{ji} and v_{kj} were set to uniformly distributed random values in the range $[-1, +1]$.

[†]The geometric pyramid rule mentioned in Section 5.3 suggests using 45 hidden units.

The training set consisted of $N = 250$ traces with random values for c_s, u_y, and $\tilde{\phi}$ out of the range specified above. Each trace consists of 1,000 data points, *i.e.*, $n = 1,000$. After each iteration, a random trace from the training set is replaced by a new trace with random u_y, c_s, and $\tilde{\phi}$ to reduce over-training. A validation set of 250 traces which are not used for the training is also created. The validation set remains unchanged during the training. It is used to check for over-training.

5.5 Results

First, look at some results of the expanded theoretical model from Section 5.2. Figs. 5.4 and 5.5 show heterodyne LITA signals from thermal gratings calculated from Eqn. 5.6. The speed of sound is represented by the Brillouin frequency (high-frequency component in signals), and the flow velocity is represented by its Doppler shift (low-frequency component). At $M = 1$, these frequencies match. All traces depicted have $M = 0.11$, $c_s = 345$ m/s.

Fig. 5.4 shows the influence of the reference beam intensity on the signal. The reference beam intensity increases by a factor of ten between each plot in Fig. 5.4b-f. The signal shape does not change for even stronger reference beams than in Fig. 5.4f. Even though it seems that the signal becomes stronger, one has to remember that the DC offset caused by the reference beam has been subtracted in Figs. 5.4 and 5.5. The offset grows like A^2 whereas the signal excluding the offset grows linearly with A. Hence, the signal amplitude relative to the DC offset actually decreases in Fig. 5.4b-f. All traces used for the neural network training and validation were chosen to be in the limit of a strong reference beam.

Fig. 5.5 shows the same trace with varying phase shifts $\tilde{\phi}$. All signals would correspond to the same flow velocity, speed of sound, *etc.* , and we expect the neural network to be uninfluenced by different values for $\tilde{\phi}$.

Fig. 5.6 shows how the error measure E as given by Eqn. 5.10 decreases during the

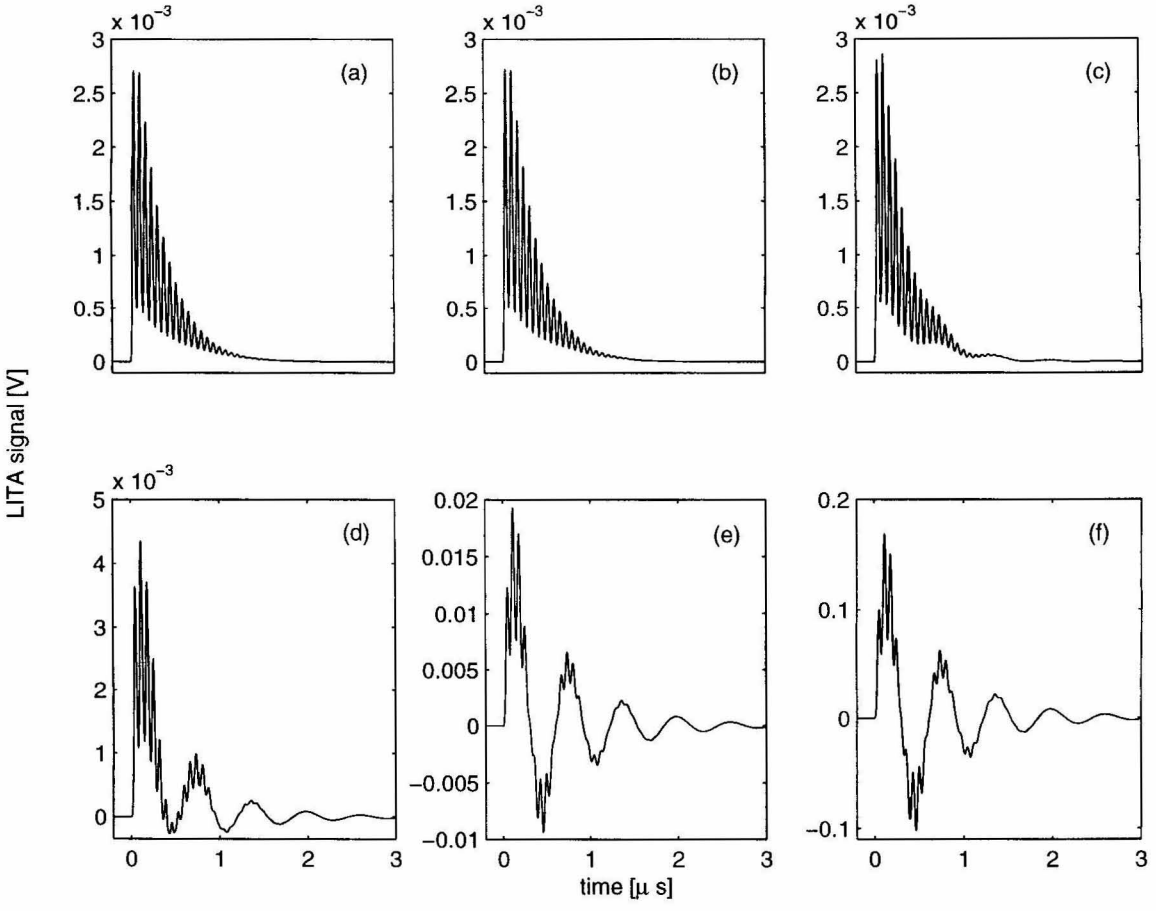

Figure 5.4: Theoretical heterodyne LITA signals for atmospheric air at $M = 0.11$ from Eqn. 5.6 for different reference beam intensities. a) $A = 0$ (homodyne signal); b) $A = 0.0001$; c) $A = 0.001$; d) $A = 0.01$; e) $A = .1$; f) $A = 1$.

training. Depicted are the cases with the most ($h = 50$) and the least hidden units ($h = 5$). The solid curves show E calculated using the training set, the symbols plot E for the validation set. The difference between the two curves indicates the amount by which the network has "specialized" to the training set. If the top curve was to level off while E for the training set continued to decrease, the performance limit of the network would be reached and any additional training would only represent over-training. *E.g.*, we see in Fig. 5.6 that both curves for $h = 50$ move parallel and that E has not reached an asymptotic value by the time the training is stopped. Continued training could improve the performance further. For the case $h = 5$, in contrast, the

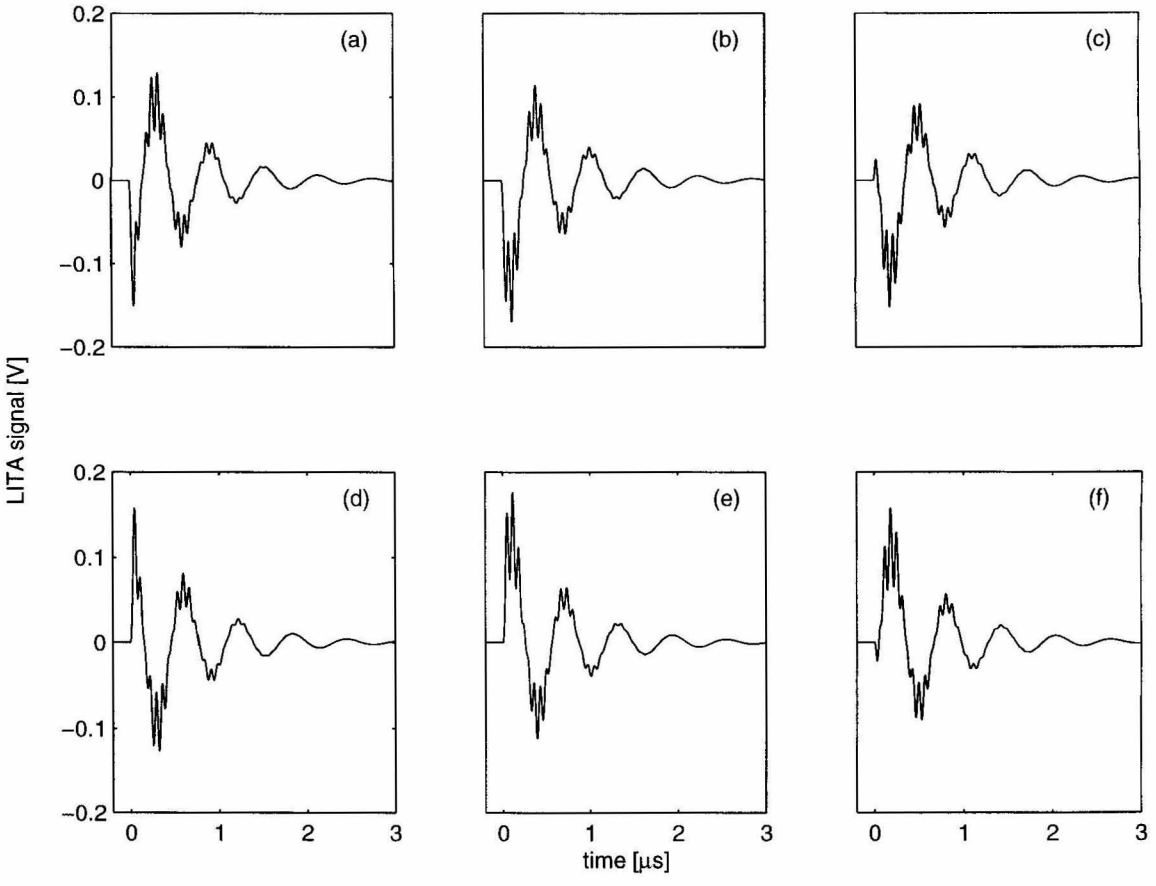

Figure 5.5: Theoretical trace in the limit of a strong reference beam and for the same flow conditions as in Fig. 5.4 but with different phase shifts between the Brillouin frequency and the Doppler shift. a) $\tilde{\phi} = 0°$; b) $\tilde{\phi} = 60°$; c) $\tilde{\phi} = 120°$; d) $\tilde{\phi} = 180°$; e) $\tilde{\phi} = 240°$; f) $\tilde{\phi} = 300°$.

errors for both the training set and the validation set have asymptotically reached minima. The curves for $h = 10, 20$ are not plotted in Fig. 5.6, but we can summarize that the minimum value of E decreases with increasing h.

Fig. 5.7 gives a direct comparison between the neural network outputs and the target values for a subsample of the validation set. We see very good agreement even for the derived Mach number ($M = u_y/c_s$). To check the robustness of the neural network data analysis approach with respect to noise, we added varying degrees of Gaussian noise to to the validation set (see examples in Fig. 5.8). Fig. 5.9 shows the

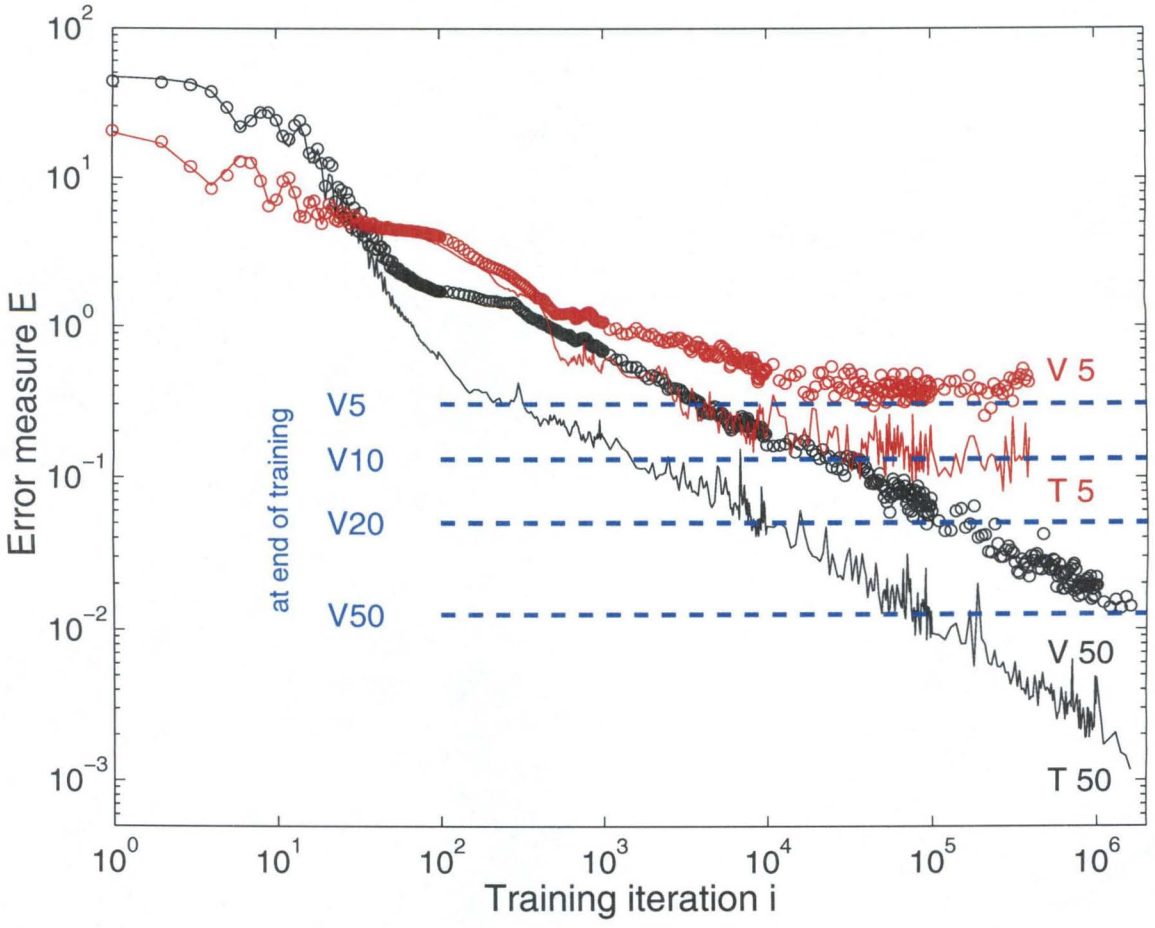

Figure 5.6: Error measure E from Eqn. 5.10 during the training phase calculated using the training set (solid curves, T50 & T5) and the validation set (symbols, V50 & V5) for 50 hidden units (V50, T50) and 5 hidden units (V5, T5). The horizontal lines mark the states at the end of the training.

RMS error of the neural network output for c_s and u_y *vs.* the signal-to-noise ratio (SNR). The errors increase slowly with the SNR. The more hidden units are used, the lower the error levels are. In the limit for zero noise, the errors for the speed of sound are 0.25 m/s ($h = 50$) and 1 m/s ($h = 5$). For the velocity measurements, the performance also depends strongly on the number of hidden units. The errors in the same limit are 2 m/s ($h = 50$) and 20 m/s ($h = 5$). For very low SNRs, the errors are large and independent of the number of hidden units. They correspond to mostly random network outputs.

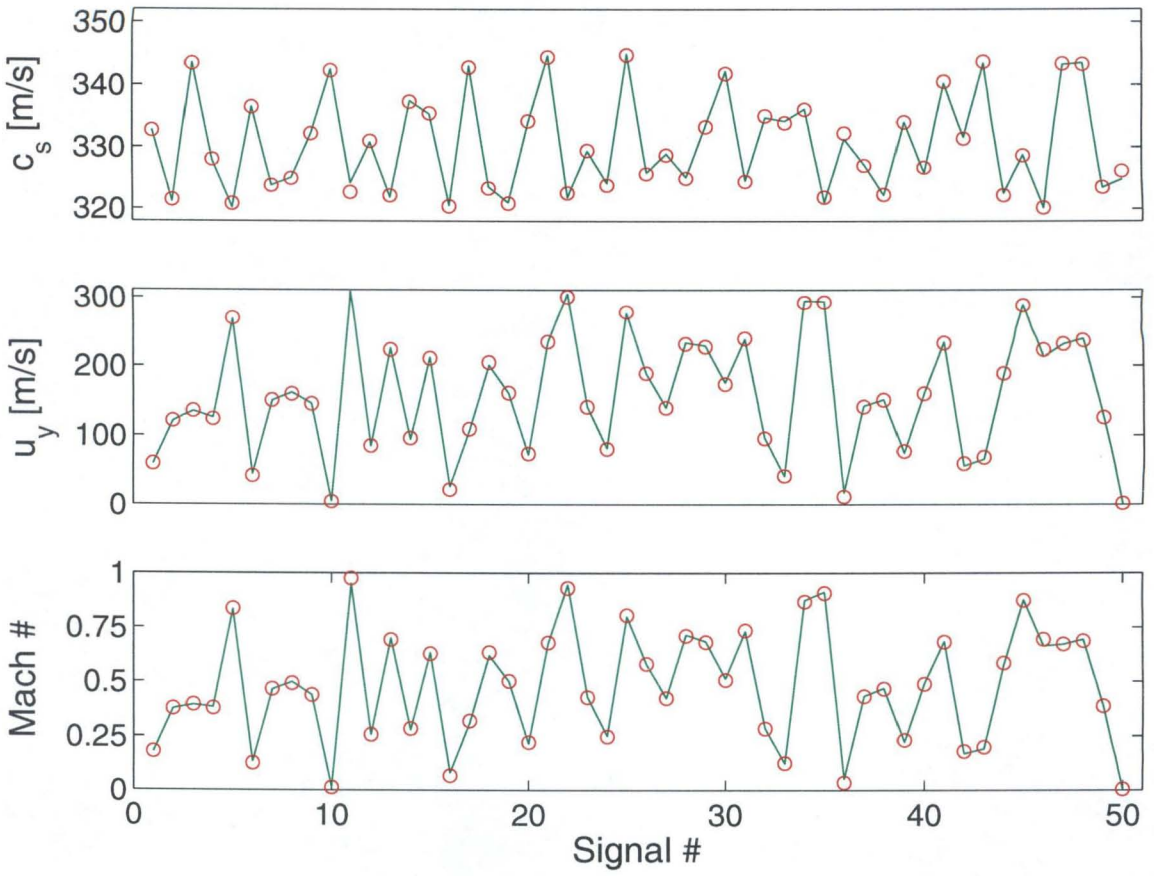

Figure 5.7: Direct comparison between neural network output and correct values for speed of sound (top), flow velocity (center), and Mach number (bottom) with $h = 50$. A set of LITA signals using 100 random c_s-u_y combinations was created and used as NN input. The green lines connect correct parameter values, the red circles mark the actual NN outputs.

Besides the bias and the variance there is a third error source for this particular application. The Doppler shift is proportional to the flow velocity. But the signal lifetime is limited by diffusion and the finite-size laser beams. Hence, at very low frequencies there will be only a fraction of a cycle within a signal, making accurate frequency measurements impossible. This so-called Fourier limit represents a theoretical limit to all data analysis techniques. Fig. 5.10 shows the uncertainty of the neural network output for c_s and u_y *vs.* the flow velocity u_y. Note that the absolute uncertainty of u_y is almost constant except for low flow velocities. It increases by one

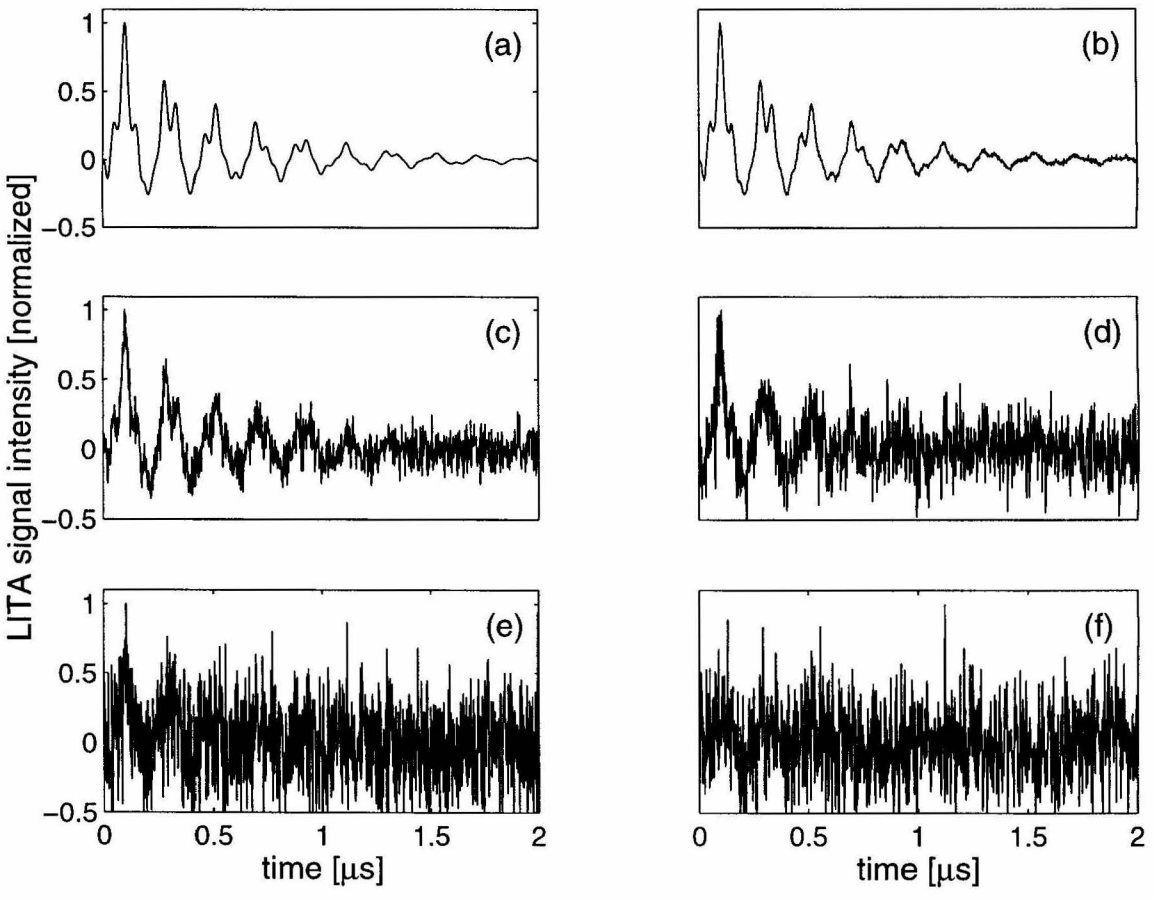

Figure 5.8: LITA traces with various SNRs. a) ∞ (no noise), b) 100 c) 10 d) 5 e) 2 f) 1.

order of magnitude for flow speeds below 30 m/s. For flow velocities close to zero, the errors become independent of the number of hidden units.

In Fig. 5.11 c_s-u_y combinations, covering the whole range of parameters that the network was trained on, are used to create signals that are used as inputs to the neural network with 50 hidden units. Correct (input) values are plotted as circles. The actual network outputs are plotted as x's. The errors are very small for the most part of the parameter space. Only for small flow velocities and in some other regions do we observe noticeable errors.

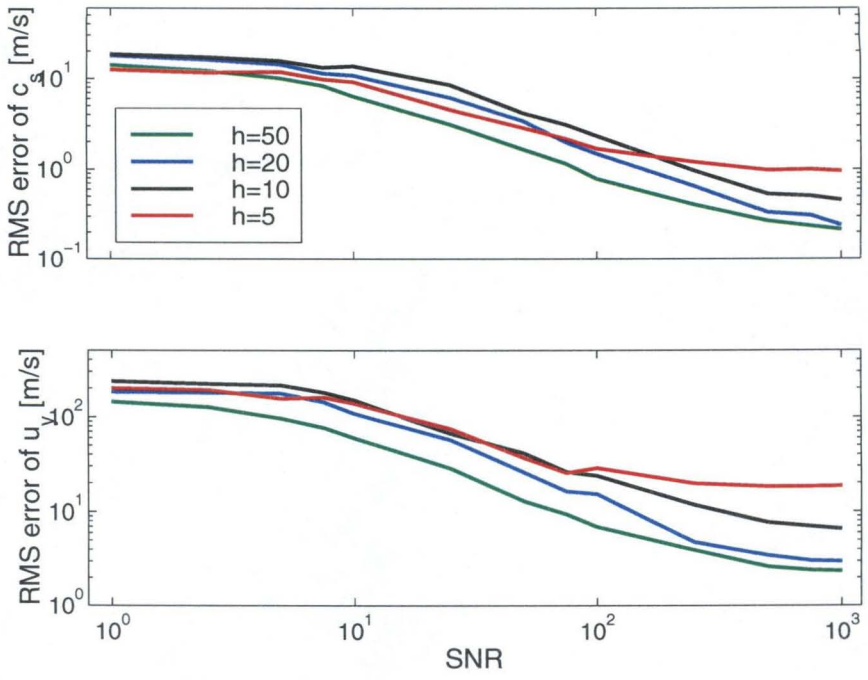

Figure 5.9: RMS error for c_s (top) and u_y (bottom) as a function of the signal-to-noise ratio SNR.

5.6 Discussion and Conclusions

A general expression for LITA signals from thermal or electrostrictive gratings and using homodyne or heterodyne detection has been derived which shows good agreement with experiments.[38] The shape of heterodyne LITA signals approaches a limit for strong reference beams. Experiments have shown that there is a phase shift between the oscillations at the Brillouin frequency and the Doppler frequency. This phase shift is due to vibrations in the optical components, temperature variations, and other non-predictable effects. It varies randomly from signal to signal. The theory presented takes this effect into account.

We implemented a one-hidden-layer feed-forward neural network algorithm for the data analysis. Its accuracy was very good with the exception of the regime of flow speeds below 50m/s. This is well before the Fourier limit should become significant.

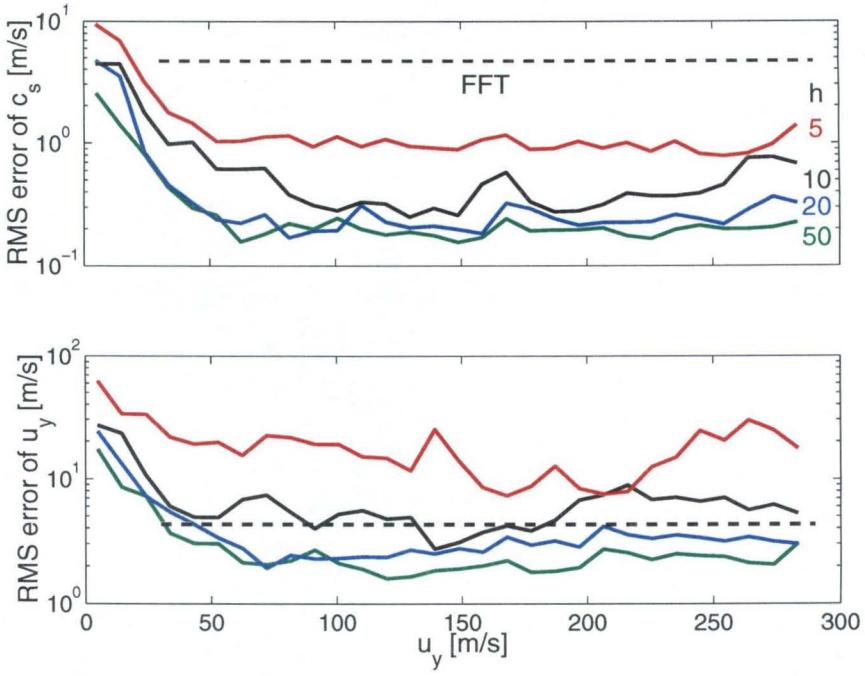

Figure 5.10: RMS error of c_s and u_y as function of u_y. The color scheme is the same as in Fig. 5.9. The dashed lines represent uncertainties using a frequency decomposition technique on the same data.

In fact, experimental results with the fitting technique show much better results in this velocity regime.[38] Also, this theoretical limit should only affect the velocity measurements but not the sound speed result. Using more than 50 hidden units could possibly mitigate this problem. In addition, we see in Fig. 5.6 that E is still decreasing for the case of $h = 50$ when the training is stopped. This means that the accuracy could be further improved by prolonging the training phase. An optimized learning rule replacing Eqns. 5.15 will reduce the number of training iteration by increasing the convergence rate of E. The fact that the errors for low SNRs and very low flow velocities are nearly independent of the number of hidden units suggests that we face a theoretical limit that we cannot overcome by increasing h.

The error for the flow velocity is fairly constant over the range of u_y. This means that the percentage errors are large at low flow velocities. This, however, is not due

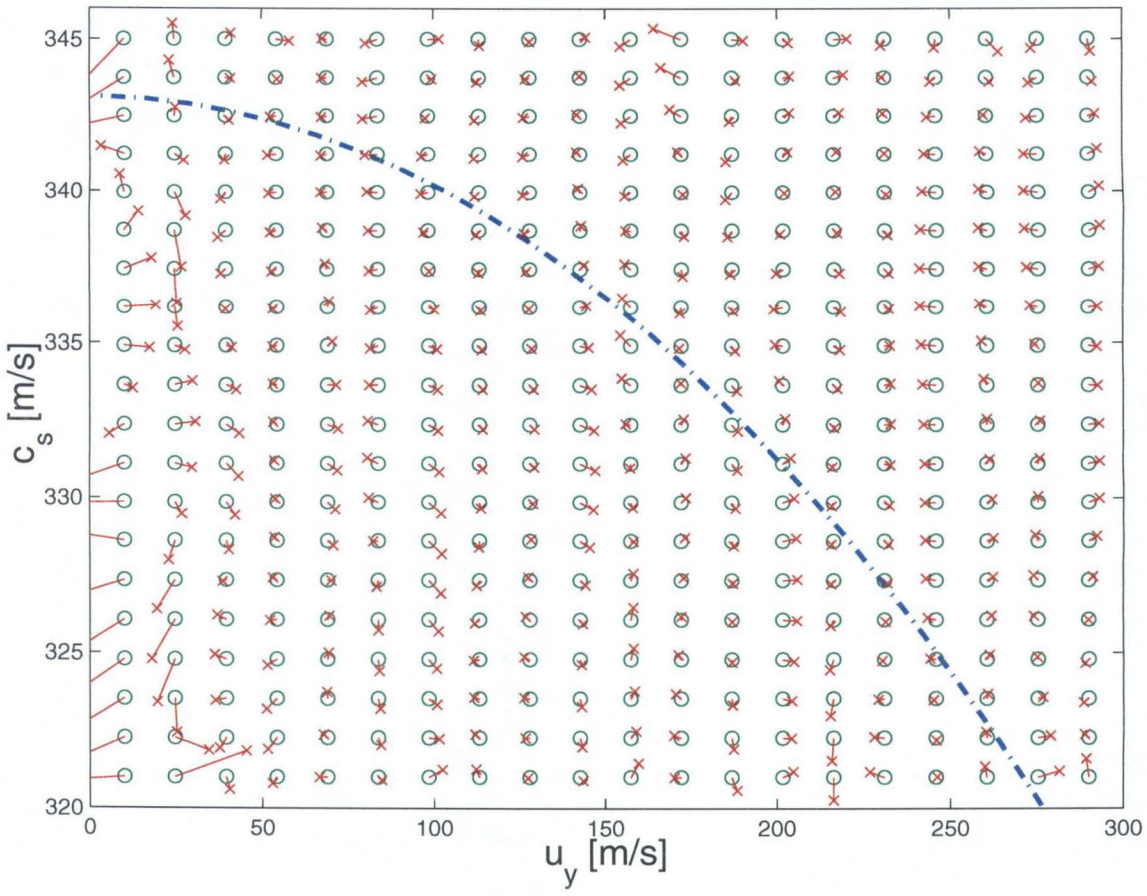

Figure 5.11: Neural network outputs (red crosses) *vs.* correct values (green circles) over a whole array of u_y-c_s combinations that the neural network was trained for. The dashed line represents the isentropic expansion of air ($T_t = 293$ K) to $M = 0.9$.

to the neural network but is governed by the Fourier limit which no data analysis method can escape. We showed that the neural network is robust with respect to noise. The performance worsens gradually in the presence of noise in the data. The phase between Brillouin frequency and Doppler shift $\tilde{\phi}$ has, as required, no influence on the data analysis.

This indicates that internally, the network performs a frequency decomposition. It does not only look for the location of the peaks in the spectrum but uses all available information in the processing. This would be equivalent to applying the fitting technique to the FFT of the experimental data. Fig. 5.3 shows the frequency decom-

position of the signal plotted in Fig. 5.4. We see that besides the two fundamental frequencies, the spectrum also contains some mixtures and harmonics of those two. For different flow velocities, the arrangement of the peaks will vary. Without prior knowledge it is non-trivial to determine which peaks correspond to the Brillouin frequency and the Doppler shift. The neural network is apparently capable of learning this task. Furthermore, note that in the case of Fig. 5.3 ($u_y = 50$ m/s), the peak for the Doppler shift is at 5.5 MHz. The resolution of the spectrum is 0.5 MHz which corresponds to flow or sound speeds of 10 m/s. This uncertainty does not include the effect that close by peaks might have for different values for u_y or the effect of noise. If we use the peak at twice the Brillouin frequency for the speed of sound determination, the uncertainty is cut in half. Similarly, by using the distance between the peaks corresponding to $f_B - f_D$ and $f_B + f_D$ in the spectrum (second and fourth peak in Fig. 5.3) we can cut the uncertainty for the flow velocity in half. Using the same input data as the neural network, the dashed lines in Fig. 5.10 mark the average uncertainty levels obtained using such an FFT peak detect scheme. The neural network performance with $h = 50$ is significantly better than that of the frequency decomposition technique.

Once the proper weights w_{ji} and v_{kj} are found in the training phase, the neural network scheme is computationally very cheap. It requires only approximately $\mathcal{O}(n \times h + h \times m)$ operations to obtain a parameter estimate from a given input. The Levenberg-Marquardt scheme, in comparison, requires the inversion of the Hessian matrix in every iteration ($\mathcal{O}(n^3)$) in addition to other calculations. Besides being computationally expensive, it also tends to be unstable if the Hessian matrix is near-singular.

We conclude that the accuracy of the neural network method presented lies in between the pure frequency decomposition technique and the nonlinear fitting technique. The computational cost is comparable to the fast frequency decomposition technique. An additional advantage of the neural network technique is its robustness.

Especially the Levenberg-Marquardt fitting scheme as described in Cummings *et al.*[29] is numerically very unstable. Lacking good initial estimates for the fitting parameters, it often does not converge to the correct solution. A combination of the neural network technique with the Levenberg-Marquardt scheme, where the neural network outputs are used as initial guesses for the Levenberg-Marquardt scheme, could be used if very accurate results are required. With good initial guesses, the Levenberg-Marquardt will be more stable and converge faster. While the neural network was only used to extract c_s and u_y, additional units in the output layer could be added, *e.g.*, to extract the thermal diffusivity or the phase shift.

It must be pointed out that the training takes considerable time. This, however, can be done in advance. In the actual experiment the data analysis can then be performed in real-time at a rate of thousands of signals per second allowing the possibility of real-time data analysis even for multi-point measurements. Currently, the LITA data analysis requires user expertise and input which is unacceptable for a user-friendly and packaged LITA system. Either on its own or in combination with the Levenberg-Marquardt algorithm, the neural network approach can provide significant advantages for this application.

Chapter 6

Summary and Conclusions

Beam misalignments pose challenges in Laser-Induced Thermal Acoustics. Their presence is not easily detected and the subtle changes they cause to the signal can lead to significant errors in the data analysis. The fitting technique is an optimum filter for the data only if the theoretical model is a correct representation of the physics of the problem. If beam misalignments are neglected then this is assumption is violated. Bulk fluid velocities of the test gas have a similar effect.

Ideally, careful alignment of the optical setup avoids beam misalignments entirely. In some applications, however, beam misalignments cannot be avoided, *e.g.*, in turbulent flow situations where fluctuating density gradients cause varying misalignments from shot to shot due to beam steering effects. The theoretical treatment in Chapter 2 provides a possible solution for such cases. While some forms of beam misalignments only affect the signal amplitude, others also change the signal shape. It was demonstrated experimentally that the magnitude of beam misalignments can be extracted from the signal quantitatively with very good accuracy. Errors for small beam misalignments can be attributed to non-Gaussian shaped beam profiles. Using the misalignment information as input to motorized optical mounts such a LITA system could perform the initial alignment almost autonomously. It could also react to slowly varying sources for beam misalignments such as thermal expansion of optics and windows. Slight misalignments that could not be detected accurately have been shown to have no influence on the accuracy or the uncertainty of the measurements. If beam misalignments are inevitable, the extended theory can be used to properly take them into account.

As byproduct of the derivation in Chapter 2 it was postulated that LITA velocimetry is possible using homodyne detection. Experiments presented in Chapter 3 confirm the postulate. An offset between the excitation beams and the interrogation beam can be used to decouple the effects of a bulk fluid velocity on the signal shape from that of other parameters. Simultaneous measurements of the speed of sound and the flow velocity were conducted in a supersonic 2D nozzle at Mach number up to $M = 2.7$ with NO_2-seeded nitrogen as test gas. The error for the speed of sound and the flow velocity was 2% and 20%, respectively. Boundary layer effects were responsible for the large errors of the velocimetry data. They should not be experienced in larger facilities.

A second approach for LITA velocimetry is used in Chapter 4 for a similar set of measurements in a low-speed wind tunnel and NO_2-seeded air as test gas. Errors here were 0.2 m/s and 0.5% for the flow velocity and the speed of sound, respectively. With heterodyne detection, the flow velocity is encoded in the signal by an additional frequency component, the Doppler shift. The Doppler shift is proportional to the flow velocity. Because the signal lifetime is finite, the accuracy for measuring low frequencies worsens ("1/f noise"). The introduction of a fixed and known frequency shift to either the signal or the reference beam, *e.g.*, by a Bragg cell, can therefore improve the accuracy for low-speed velocimetry applications and it also removes the direction ambiguity. Normally, heterodyne LITA velocimetry will fail near sonic conditions because the Doppler shift and the Brillouin frequency are identical at $M = 1$.* The two frequencies cannot be determined independently of each other. A Bragg cell also helps in this situation by moving the Doppler frequency away from the Brillouin frequency.

While homodyne LITA velocimetry is only expected to work in high-speed flows, heterodyne LITA velocimetry can be used over the entire range of flow speeds. It does, however, require an additional laser beam which makes the alignment substantially

*For electrostrictive gratings, this occurs at $M = 2$.

more cumbersome. Since velocity and speed of sound are represented by frequencies in the case of heterodyne LITA velocimetry, the use of a frequency decomposition technique for the data analysis is conceivable. Homodyne LITA velocimetry must involve the more general fitting technique.

All measurements discussed so far were resonant, *i.e.*, the excitation beam frequency fell on an absorption band of the test or seed gas. In general, resonant LITA provides stronger signals at a given excitation laser energy. The signal level can be controlled by the seed concentration. As discussed in Chapter 1, seeding is not always possible or desirable. In these cases an excitation laser frequency can be chosen that falls on an absorption line or band of the test gas. For air or nitrogen, this would require a wavelength in the UV range. The necessary frequency doublers or mixers make powerful, pulsed UV lasers very expensive.

Another possibility for LITA without seeding and using lasers in the IR or visible range is to use electrostrictive gratings. If the quality of the laser beams is good, electrostrictive gratings can result in comparable signal levels. Appendix B describes a set of experiments which were conducted in unseeded air and with a standard frequency-doubled Nd:YAG lasers. Intuitively, we expect the accuracy to be improved for higher signal (*i.e.*, lower noise) levels. If the excitation beam pulse energy is used to increase the signal strength, then the expected trend is reversed above a certain pump energy. This is because the disturbances can no longer be treated as acoustic waves of infinitesimal strength. Instead, they are finite-strength waves, which are not covered in the theoretical treatment. Hence, other ways to increase the signal level such as increasing the interrogation beam power, increasing the gain of the detector, *etc.* , have to be preferred. These results should also be valid for the case of LITA using gratings from thermalization.

A novel approach for LITA data analysis involving artificial neural networks was introduced and successfully tested. After an extensive training period in which the neural network "learns" the task of extracting the speed of sound and the flow velocity

from heterodyne LITA signals from a set of examples, the network outperforms classical frequency decomposition techniques with respect to accuracy. The computational cost is very low so that real-time data analysis is possible. The method is also robust w.r.t. noise in the signal and lacks any numerical instability that the more accurate, but slow, fitting technique experiences. The neural network algorithm could be either used as the only method of data analysis or it can be used as a preprocessing step where it provides the fitting routine with initial guesses for the fitting parameters.

Several technique improvements have been treated both theoretically and experimentally with very good agreement. The results involving beam misalignments can lead to more user-friendly "turn-key" LITA systems. Previously, LITA's main application was in quiescent gases, *e.g.*, to determine gas properties with very high accuracy. Adding velocimetry to the capabilities of LITA makes it a very promising technique for flow diagnostics. As optical technique, it is non-intrusive and remote which is of particular interest for supersonic measurements. As nonlinear technique it can be used in hostile flow environments (particles, luminosity, short test times).[†]

[†]LITA was demonstrated in the region behind a reflected shock wave created by a combustion-driven shock tube (unpublished work).

Chapter 7

Outlook and Future Work

7.1 Two-component velocimetry

Adding the capability of measuring an additional velocity component is conceivable. The approach would be similar to the multi-component LDV techniques. Fig. 7.1 shows schematically an optical setup where four excitation beams create a two-dimensional electric field intensity grating as plotted in Fig. 7.2. Driver beams labeled D1 and D1' create the horizontal grating, and driver beams D2 and D2' produce the vertical grating. Interrogation beam I1 lies in the vertical plane and is scattered off the horizontal fringes into signal beam S1, while interrogation beam I2 lies in the horizontal plane and is scattered off the vertical fringes into signal beam S2. All beams but S1 and S2 are subsequently blocked by beam blocks. The Doppler shift of signal beam 1 is proportional to the velocity component in z-direction w, the Doppler shift of signal beam 2 is proportional the the velocity component in y-direction v. Since all disturbances are weak, linear behavior of the fluid and linear scattering is assumed. The second grating therefore does not influence the LITA processes in the first grating. Unlike in LDV, where the particles scatter incoherently, LITA results in coherent beams. Therefore, all excitation beams can be of the same wavelength. Also, interrogation beams can be of equal wavelength (but different from the excitation beam wavelength). To simplify the optical setup, fiber optics can provide the two reference beams. Chapter 4 mentioned the possibility of using a Bragg cell to shift the frequency of the reference beam slightly. Theoretically, this improves the accuracy for low flow velocities and removes direction ambiguity from the measurements. The

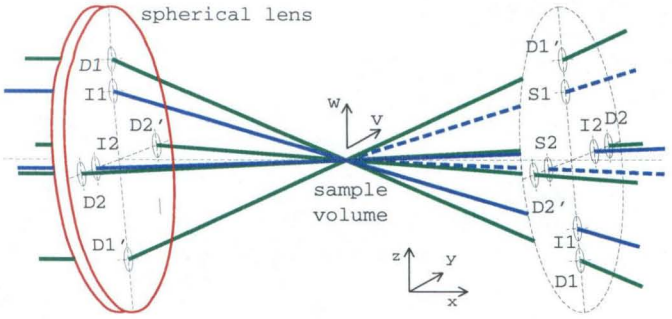

Figure 7.1: Schematic of optical setup for 2-component LITA velocimetry. The dashed disk on the right is for perspective purposes only.

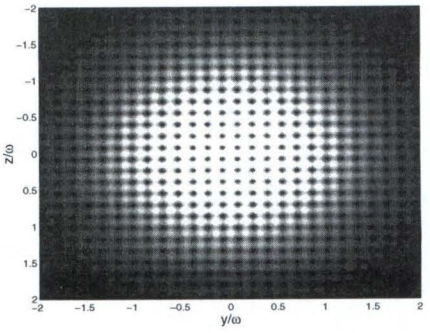

Figure 7.2: Two-dimensional electric field intensity grating from using optical setup in Fig. 7.1.

setup in Fig. 7.1 allows using different Bragg cells for the two velocity components. This is important in situations with mostly one-dimensional flow. The beam setup in Fig. 7.1 cannot be used very close to the sidewalls.

7.2 Multi-point measurements

LITA can be converted from a point-measurement technique to a line- or multi-point measurement technique. Several approaches are feasible, *e.g.*, scanning the laser beams, creating a number of distinct laser beams, or using laser sheets. Considering the high time-resolution and pointing-accuracy requirements, the scanning approach will be hard to accomplish. A set of individual laser beams could easily be created by diffractive optics. These, however, do not have a sufficient laser power damage threshold at this time. Working instead with a set of beam splitters poses the challenge to align each beam pair individually. For cases where the spatial extent of the measurement points is small, the technique involving intersecting laser sheets (Fig. 7.3) is most promising.

Using laser sheets instead of beams stretches the sample volume along a line, and given the capability of space- and time-resolved detection of the signal beam (sheet), LITA can be used as a multi-point or line-measurement technique. Work is under

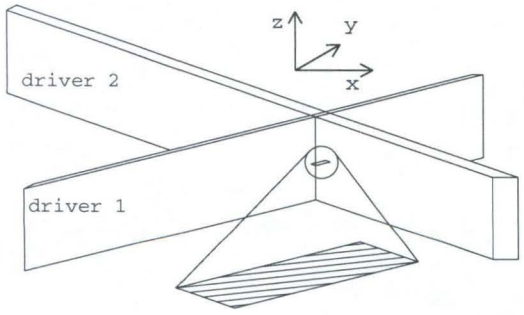

Figure 7.3: Intersecting laser sheets create an interference grating within a stretched region (sample volume).

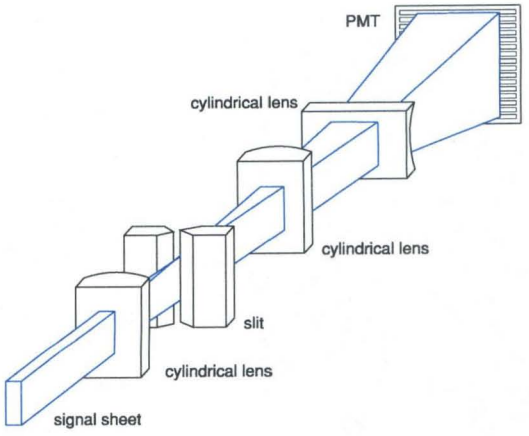

Figure 7.4: Layout of receiver unit for multi-point measurements.

way to demonstrate this principle using a commercially available 16-channel photo-multiplier tube (PMT) as detector where the sensitive regions corresponding to the 16 channels are arranged as parallel linear elements (Fig. 7.4).

The length of the sample volume can be increased to any desired value as can the number of channels per unit length. There is a trade-off, however, between signal intensity, spatial resolution, and extent of the sample volume. The signal intensity scales with the square of the driver beam energy density and linear with the interrogation beam energy density. Hence, given fixed laser powers, we obtain a cubic dependence of the signal intensity with the length of the sample volume. The second consideration is the number of channels per unit length. The more channels we have the weaker will be the signal contribution for each of the channels, but the better will be the spatial resolution. If multi-point measurements are desired with large spacings in between points, optical arrangements that yield a series of individual point measurements should be considered. A possible application of multi-point LITA are boundary layer measurements as LITA allows the simultaneous measurement of the speed of sound (temperature) and fluid velocity.

7.3 System integration

A flow diagnostic technique is needed that can be applied in unseeded, luminous, high-pressure, high-enthalpy flows. In Appendix B it is demonstrated that LITA does not require seeding with NO_2. Electrostrictive gratings yield similar scattering efficiencies but require a high beam quality. Considering beam-steering effects due to density gradients, it is questionable if this can be achieved in the test section of T5. Resonant excitation, *i.e.*, to use an excitation wavelength that falls on a natural absorption band of a species in the flow, can also replace seeding.

With signal lifetimes of $\mathcal{O}(1\ \mu s)$, 10^6 measurements per second are possible. YAG lasers with sufficient pulse energies currently achieve pulse repetition rates of 50 Hz. Using a copper-vapor laser with pulse repetition rates of up to 50 kHz range would be an interesting experiment well worth the effort. Pulse energies are typically only in the order of 1 mJ/pulse, pulse lengths are $\approx$ 20 ns.* The challenge would hence be either to lower the power requirements for LITA measurements considerably or to wait for advances in laser technology.

The foremost task is to integrate the various extensions, which were presented, in a single experiment. This means to use a multi-point LITA setup in a wind tunnel to measure the flow velocity and temperature simultaneously, say across a supersonic boundary layer, using electrostrictive gratings in unseeded flow and real-time data analysis with a trained neural network.

Preliminary experiments with a long-pulse Nd:YAG at its fundamental frequency of 1,064 nm as interrogation beam have shown encouraging results. Hence, a single laser cavity can provide the excitation and the interrogation beams. The high beam powers during the pulse resulted in very strong signals, detectable with a fast photodiode.

*Consider that a 50 kHz repetition rate with 20 mJ pulse energies would mean an average laser power of 1 kW.

7.4 Outlook

As with every new technique there is a considerable time-lag of many years between development in a laboratory setting and commercial applications. The time-lag is maintained between further improvements or extensions of the original technique and their commercial use. *E.g.*, while three-component PIV is on the verge of becoming common practice in research laboratories, it is currently not found in packaged systems.

PIV and LDV have already taken the step of becoming commercially available whereas LITA still has to embrace the marketplace. Science, in the meantime, has already started the process of building on the foundations. Even with today's off-the-shelf equipment there are undoubtedly many possible improvements and refinements of Laser-Induced Thermal Acoustics which will guarantee a lead of the latest scientific over commercial applications for years to come.

Bibliography

[1] H.G. Hornung. Performance data of the new free-piston shock tunnel at GALCIT. AIAA Paper 92-3943, 1992.

[2] E.B. Cummings. *Laser-Induced Thermal Acoustics.* PhD thesis, California Institute of Technology, 1995.

[3] C.F. Kaminski, J. Hult, and M. Alden. High repetition rate planar laser induced fluorescence of OH in a turbulent non-premixed flame. *Applied Physics B - Lasers and Optics*, 68:757–760, 1999.

[4] P.M. Danehy, P.C. Palma, R.R. Boyce, and A.F.P. Houwing. Numerical simulation of Laser-Induced Fluorescence imaging in shock layer flows. *AIAA Journal*, 37:715–722, 1999.

[5] J.L. Palmer and R.K. Hanson. Shock tunnel flow visualization using planar Laser-Induced Fluorescence imaging of NO and OH. *Shock Waves*, 4:313–323, 1995.

[6] P.C. Palma, T.J. McIntyre, and A.F.P. Houwing. PLIF thermometry in shock tunnel flows using a Raman-shifted tunable excimer laser. *Shock Waves*, 8:275–284, 1998.

[7] P.T. Tokumaru and P.E. Dimotakis. Image correlation velocimetry. *Experiments in Fluids*, 19:1–15, 1995.

[8] R.B. Miles, J. Connors, E. Markovitz, P. Howard, and G. Roth. Instantaneous supersonic velocity profiles in an underexpanded sonic air jet by oxygen flow tagging. *Physics of Fluids A - Fluid Dynamics*, 1:389–393, 1989.

[9] J.A. Wehrmeyer, L.A. Ribarov, D.A. Oguss, and R.W. Pitz. Flame flow tagging velocimetry with 193 nm H_2O photodissociation. *Applied Optics*, 38:6912–6917, 1999.

[10] C. Orlemann, C. Schulz, and J. Wolfrum. NO flow tagging by photodissociation of NO_2. A new approach for measuring small-scale flow structures. *Chemical Physics Letters*, 307:15–20, 1999.

[11] S. Kruger and G. Grunefeld. Stereoscopic flow-tagging velocimetry. *Applied Physics B - Lasers and Optics*, 69:509–512, 1999.

[12] P.F. Barker, A.M. Thomas, T.J. McIntyre, and H. Rubinsztein-Dunlop. Velocimetry and thermometry of supersonic flow around a cylindrical body. *AIAA Journal*, 36:1055–1060, 1998.

[13] P. Barker, A. Bishop, and H. Rubinsztein-Dunlop. Supersonic velocimetry in a shock tube using laser enhanced ionization and planar laser induced fluorescence. *Applied Physics B - Lasers and Optics*, 64:369–376, 1997.

[14] P. Lemieux. *The instability of shear layers produced by curved shocks.* PhD thesis, California Institute of Technology, 1999.

[15] A. Krothapalli, E. Rajkuperan, F. Alvi, and L. Lourenco. Flow field and noise characteristics of a supersonic impinging jet. *Journal of Fluid Mechanics*, 392:155–181, 1999.

[16] M. Raffel and F. Kost. Investigation of aerodynamic effects of coolant ejection at the trailing edge of a turbine blade model by piv and pressure measurements. *Experiments in Fluids*, 24:447–461, 1998.

[17] M.P. Arroyo and C.A. Greated. Stereoscopic particle image velocimetry. *Measurement Science and Technology*, 2:1181–1186, 1991.

[18] R.B. Miles and W.R. Lempert. Quantitative flow visualization in unseeded flows. *Annual Review of Fluid Mechanics*, 29:285–326, 1997.

[19] J.N. Forkey, W.R. Lempert, and R.B. Miles. Accuracy limits for planar measurements of flow field velocity, temperature and pressure using filtered Rayleigh scattering. *Experiments in Fluids*, 24:151–162, 1998.

[20] J.A. Lock, R.G. Seasholtz, and W.T. John. Rayleigh-Brillouin scattering to determine one-dimensional temperature and number density profiles of a gas flow field. *Applied Optics*, 31:2839–2848, 1992.

[21] R.G. Seasholtz. Instantaneous two-dimensional velocity and temperature measurements in high-speed flows based on spectrally-resolved molecular Rayleigh scattering. AIAA Paper 1995-0300, 1995.

[22] J.P. Bonnet, D. Gresillon, and J.P. Taran. Nonintrusive measurements for high-speed, supersonic, and hypersonic flows. *Annual review of Fluid Mechanics*, 30:231–273, 1998.

[23] S.R. Yang, J.R. Zhao, C.J. Sung, and G. Yu. Multiplex CARS measurements in supersonic H_2/air combustion. *Applied Physics B - Lasers and Optics*, 68:257–265, 1999.

[24] M. Pealat and M. Lefebvre. Temperature measurements by dual-line CARS in low-pressure flows. *Applied Physics B - Lasers and Optics*, 53:23–29, 1991.

[25] T.J. Anderson and A.C. Eckbreth. Simultaneous coherent anti-Stokes-Raman spectroscopy measurements in hydrogen-fueled supersonic combustion. *Journal of Propulsion and Power*, 8:7–15, 1992.

[26] C. Tropea. Laser Doppler Anemometry - recent developments and future challenges. *Measurement Science and Technology*, 6:605–619, 1995.

[27] D. Dopheide, V. Strunck, and H.J. Pfeifer. Miniaturized multi-component velocity measurements using high-frequency pulsed diode lasers and new electronic signal acquisition systems. *Experiments in Fluids*, 9:309–316, 1993.

[28] H. J. Eichler, P. Günther, and D. W. Phol. *Laser-Induced Dynamic Gratings.* Springer-Verlag, New York, 1986.

[29] E. B. Cummings, I. A. Leyva, and H. G. Hornung. Laser-Induced Thermal Acoustics (LITA) signals from finite beams. *Applied Optics*, 34(18):3290–3302, 1995.

[30] W.S. McCulloch and W. Pitts. A logical calculus of ideas immanent in nervous activity. *Bulletin of Mathematical Biophysics*, 5:115–133, 1943. Reprinted in Ref..[79]

[31] M.L. Minsky. *Computation: Finite and Infinite Machines.* Prentice-Hall, Englewood Cliffs, 1967.

[32] A.E. Bryson and Y.C. Ho. *Applied Optimal Control.* Blaisdell, New York, 1969.

[33] P. Werbos. *Beyond Regression: New Tools for Prediction and Analysis in the Behavioral Sciences.* PhD thesis, Harvard University, 1974.

[34] D.B. Parker. Learning logic. Technical Report TR-47, Center for Computational Research in Economics and Management Science, Massachusetts Institute of Technology, Cambridge/MA, 1985.

[35] D.E. Rumelhart, G.E. Hinton, and R.J. Williams. Learning representations by back-propagating errors. *Nature*, 323:533–536, 1986.

[36] S. Schlamp, E.B. Cummings, and H.G. Hornung. Beam misalignments and fluid velocities in Laser-Induced Thermal Acoustics (LITA). *Applied Optics*, 38(27):5724–5733, 1999.

[37] S. Schlamp and E. Allen-Bradley. Homodyne detection Laser-Induced Thermal Acoustics velocimetry. AIAA Paper 2000-0376, 2000.

[38] S. Schlamp, E.B. Cummings, and Th.H. Sobota. LITA velocimetry using heterodyne detection. *Optics Letters*, 25(4):224–226, 2000.

[39] S. Schlamp, H.G. Hornung, and E.B. Cummings. Neural network data analysis for Laser-Induced Thermal Acoustics. *Measurement Science and Technology*, 11:784–794, 2000.

[40] S. Schlamp and E. Camera. Multi-point measurements with Laser-Induced Thermal Acoustics (LITA). AIAA Paper 2000-2590, 2000.

[41] S. Schlamp, H.G. Hornung, Th.H. Sobota, and E.B. Cummings. Accuracy and uncertainty of single-shot, nonresonant Laser-Induced Thermal Acoustics. *Submitted to Applied Optics*, 2000.

[42] T.J. Butenhoff. Measurement of the thermal-diffusivity and speed of sound of hydrothermal solutions via the laser-induced grating technique. *International Journal of Thermophysics*, 16(1):1–9, 1995.

[43] B. Hemmerling and D.N. Kozlov. Generation and temporally resolved detection of laser-induced gratings by a single, pulsed Nd:YAG laser. *Applied Optics*, 38(6):1001–1007, 1999.

[44] M.S. Brown and W.L. Roberts. Single-point thermometry in high-pressure, sooting, premixed combustion environments. *Journal of Propulsion and Power*, 15(1):119–127, 1999.

[45] D.J.W. Walker, R.B. Williams, and P. Ewart. Thermal grating velocimetry. *Optics Letters*, 23(16):1316–1318, 1998.

[46] D.B. Brayton. Small particle signal characteristics of a dual-scatter laser velocimeter. *Applied Optics*, 13(10):2346–2351, 1974.

[47] A.E. Siegman. Bragg diffraction of a gaussian beam by a crossed-gaussian volume grating. *Journal of the Optical Society of America*, 67(4):545–550, 1977.

[48] B.J. Berne and R. Pecora. *Dynamic Light Scattering.* John Wiley & Sons, New York, 1976.

[49] W. H. Press. *Numerical Recipes in C: The Art of Scientific Computing.* Cambridge University Press, Cambridge, MA, 1988.

[50] R.C. Hart, R.J. Balla, and G.C. Herring. Nonresonant referenced Laser-Induced Thermal Acoustics thermometry in air. *Applied Optics*, 38(3):577–584, 1999.

[51] B. Hemmerling, D.N. Kozlov, and A. Stampanoni-Panariello. Measurement of gas flow velocities by electrostrictive laser-induced gratings. In *Book of abstracts, XVIII European CARS Workshop: CARS and related gas-phase diagnostics, C.R. ENEA, Frascati, Italy, March 21-23, 1999*, 1999.

[52] E.B. Cummings. Laser-Induced Thermal Acoustics: Simple accurate gas measurements. *Optics Letters*, 19(17):1361–1363, 1994.

[53] R.W. Boyd. *Nonlinear Optics.* Academic Press, San Diego, 1992.

[54] A.C. Eckbreth. *Laser Diagnostics for Combustion Species and Temperature.* Abacus Press, Cambridge, MA, 1988.

[55] S. Williams, L.A. Rahn, P.H. Paul, J.W. Forsman, and R.N. Zare. Laser-induced grating effects in flames. *Optics Letters*, 19(21):1681–1683, 1994.

[56] M. Raffel and J. Kompenhans. Theoretical and experimental aspects of image-shifting by means of a rotating mirror system for particle image velocimetry. *Measurement Science and Technology*, 6(6):795–808, 1995.

[57] P.F. Baker, J.H. Grinstead, and R.B. Miles. Single-pulse temperature measurement in supersonic air flow with predissociated laser-induced thermal gratings. *Optics Communications*, 168:177–182, 1999.

[58] S.L. Marple. *Digital Spectral Analysis with Applications.* Prentice-Hall, Englewood Cliffs, N.J., 1987.

[59] D.M. Scott and R.L. Waterland. Identification of plastic waste using spectroscopy and neural networks. *Polymer Engineering and Science*, 35(12):1011–1015, 1995.

[60] H.W. Balfoort, J. Snoek, J.R.M. Smits, and et al. Automatic identification of algae - neural network analysis of flow cytometric data. *Journal of Plankton Research*, 14(2):575–589, 1992.

[61] R. Safaric, K. Jezernik, and M. Pec. Neural network control for direct-drive robot mechanisms. *Engineering Applications of Artificial Intelligence*, 11(6):735–745, 1998.

[62] L.S. Woon, S.S. Ge, X.Q. Chen, and et al. Adaptive neural network control of coordinated manipulators. *Journal of Robotic Systems*, 16(4):195–211, 1999.

[63] R. Linggard, D.J. Myers, and C. Nightingale (editors). *Neural networks for vision, speech, and natural language.* Chapman & Hall, London, 1992.

[64] C.L. Giles and M. Gori, editors. *Adaptive processing of sequences and data structures: International Summer School on Neural Networks.* Springer, Berlin, 1998.

[65] C.T. Leondes, editor. *Neural network systems, techniques, and applications.* Academic Press, San Diego, 1998.

[66] J. Hertz, A. Krogh, and R.G. Palmer. *Introduction to the Theory of Neural Computation.* Addison-Wesley, New York, 1991.

[67] C.M. Bishop. *Neural Networks for Pattern Recognition.* Oxford University Press, Oxford, 1995.

[68] S. Haykin. *Neural Networks - A Comprehensive Foundation.* Prentice-Hall, Upper Saddle River, 1999.

[69] F. Rosenblatt. *Principles of Neurodynamics.* Spartan, New York, 1962.

[70] P.J. Werbos. *The Roots of Backpropagation.* John Wiley & Sons, New York, 1994. Reprinted and updated version of Ref..[33]

[71] H. Robbins and S. Monro. A stochastic approximation method. *Annals of Mathematical Statistics*, 22:400–407, 1951.

[72] J.P. Cater. Successfully using peak learning rates of 10 (and greater) in back-propagation networks with the heuristic learning algorithm. In M. Caudill and C. Butler, editors, *IEEE First International Conference on Neural Networks (San Diego 1987)*, volume II, pages 645–651, New York, 1987. IEEE.

[73] M.A. Franzini. Speech recognition with back propagation. In *Proceedings of the Ninth Annual Conference of the IEEE Engineering in Medicine and Biology Society (Boston 1987)*, pages 1702–1703, New York, 1987. IEEE.

[74] T.P. Vogl, J.K. Mangis, A.K. Rigler, W.T. Zink, and D.L. Alkon. Accelerating the convergence of the back-propagation method. *Biological Cybernetics*, 59:257–263, 1988.

[75] R.A. Jacobs. Increased rates of convergence through learning rate adaptation. *Neural Networks*, 1:295–307, 1988.

[76] G. Cybenko. Approximation by superpositions of a sigmoidal function. *Mathematics of Control, Signals, and Systems*, 2:337–341, 1989.

[77] K. Hornik, M. Stinchcombe, and H. White. Multilayer feed-forward networks are universal approximators. *Neural Networks*, 2:359–366, 1989.

[78] T. Masters. *Practical Neural Network Recipes in C++*. Academic Press, London, 1993.

[79] J.A. Anderson and E. Rosenfeld, editors. *Neurocomputing: Foundations of Research*. MIT Press, Cambridge, MA, 1988.

[80] A.H. Shapiro. *The Dynamics and Thermodynamics of Compressible Fluid Flow*, volume II. John-Wiley & Sons, New York, 1953.

[81] H.W. Liepmann and A. Roshko. *Elements of Gasdynamics*. John-Wiley & Sons, New York, 1957.

Appendices

Appendix A

Electric Field Intensity Terms Not Contributing to the LITA Signal

At this point, we want to briefly explain the reasoning for the simplification made in Eqn. 2.2. The full expression we have to examine is $(\mathsf{E}_{d1} + \mathsf{E}_{d2})(\mathsf{E}_{d1} + \mathsf{E}_{d2})^*$ with $\mathsf{E}_{d1} = \mathsf{E}_1 + \mathsf{E}_1^*$ and $\mathsf{E}_{d2} = \mathsf{E}_2 + \mathsf{E}_2^*$. Hence,

$$\begin{aligned}(\mathsf{E}_{d1} + \mathsf{E}_{d2})(\mathsf{E}_{d1} + \mathsf{E}_{d2}) = &\underbrace{(\mathsf{E}_1\mathsf{E}_1 + \mathsf{E}_2\mathsf{E}_2 + \mathsf{E}_1^*\mathsf{E}_1^* + \mathsf{E}_2^*\mathsf{E}_2^*)}_{\text{Term A}} \\ &+ 2\underbrace{(\mathsf{E}_1\mathsf{E}_1^* + \mathsf{E}_2\mathsf{E}_2^*)}_{\text{Term B}} \\ &+ 2\underbrace{(\mathsf{E}_1\mathsf{E}_2 + \mathsf{E}_1^*\mathsf{E}_2^*)}_{\text{Term C}} \\ &+ 2\underbrace{(\mathsf{E}_1\mathsf{E}_2^* + \mathsf{E}_1^*\mathsf{E}_2)}_{\text{Term D}} \end{aligned} \tag{A.1}$$

Look only at the time and y-dependencies of the individual terms:

$$\begin{aligned} \mathsf{E}_1 &\sim \exp\{+iy\sin\theta - if_d t\} & \mathsf{E}_1^* &\sim \exp\{-iy\sin\theta + if_d t\} \\ \mathsf{E}_2 &\sim \exp\{-iy\sin\theta - if_d t\} & \mathsf{E}_2^* &\sim \exp\{+iy\sin\theta + if_d t\} \end{aligned} \tag{A.2}$$

Substituting Eqns. A.2 into Eqns. A.1 we see that term A fluctuates with a frequency of $2f_d$. Term B shows the steady time behavior but the spatial grating has dropped out, *i.e.*, it represents a (spatially) constant background to the electric field intensity. Term C finally fluctuates at $2f_d$ and it also is not varying in space. Terms A-C will

have no contribution to the scattering of the source beam into the signal beam (see Section 2.5). Only term D shows the sought after behavior

$$\mathsf{E}_1\mathsf{E}_2^* \sim \exp\{2iy\sin\theta\} \qquad \mathsf{E}_1^*\mathsf{E}_2 \sim \exp\{-2iy\sin\theta\}\,, \tag{A.3}$$

i.e., they represent a steady grating. The introduction of the beam misalignments $\vec{r}_{1,2}$ does not change the previous explanation for terms A and C. But term B now is no longer constant. Instead, it has the shape of the superposition of two Gaussian distributions (similar to Fig. 2.2b) in space which does not constitute a good grating. Also note that the scattering of the source beam is only efficient if the incidence angle of the source beam on the grating is the Bragg angle.

Appendix B
Accuracy and Repeatability of Single-Shot LITA Measurements

B.1 Introduction

In the four-wave mixing technique Laser-Induced Thermal Acoustics, two pulsed laser beams (driver beams) intersect at a shallow angle in the test gas. There, interference creates an electric field grating. By the molecular mechanisms of electrostriction and/or thermalization the electric field grating results in a density perturbation and hence a refractive index grating. Thermalization is predominant for resonant pumping, whereas electrostrictive gratings dominate in the case of non-resonant pumping. If a continuous laser beam is directed at the Bragg angle at the density grating, part ($\mathcal{O}(0.01\%)$) of this interrogation beam is coherently scattered into a signal beam. Since the density grating evolves over time and the signal beam intensity is proportional to the instantaneous density grating modulation depth, the signal beam allows us to observe the grating evolution.

The speed of sound is encoded in the LITA signal as the Brillouin frequency, *i.e.*, the speed of sound divided by the fringe spacing of the density grating. The thermal diffusivity together with the Gaussian beam profiles causes the exponentially decaying tail of a LITA signal (Fig. B.1). To extract speed of sound and the thermal diffusivity from a LITA signal we use a theoretical model[29,36] and a nonlinear fitting procedure (Levenberg-Marquardt scheme,[49] that fits this model to the experimental data. The speed of sound and the thermal diffusivity are fitting parameters. A

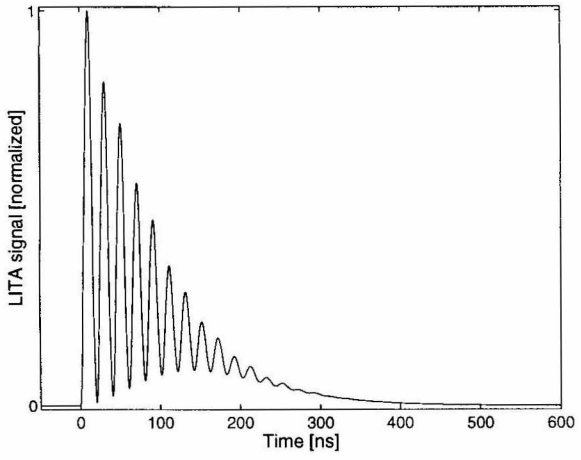

Figure B.1: Typical LITA signal from electrostrictive gratings in atmospheric air.

frequency decomposition technique to extract the Brillouin frequency from the signal is also possible[51] but it does not allow for measurements of the thermal diffusivity. The same is true for using Pronys method to extract the speed of sound.[50,58]

The accuracy (*i.e.*, the systematic error) and the uncertainty (*i.e.*, the statistical error) of this method depend on a number of parameters. The measurement of the Brillouin frequency will be improved if many oscillation cycles are recorded in the signal and if the time resolution is good. Similarly, we want the total signal recording time and sampling rate to be appropriate for the decay time constant of the signal tail. Besides this, the accuracy and uncertainty of LITA measurements is mostly limited by two factors: noise in the recorded signals and deviations of the theoretical model from reality. These latter two factors are examined here.

To raise the signal-to-noise ratio (SNR) at a fixed noise level, one can increase either the driver laser pulse energy or the interrogation beam power. Theoretically, the signal should be proportional to the source laser power and should scale quadratically with the driver laser pulse energy,[2] provided that all other experimental parameters are held constant (beam crossing angle, beam geometry, detector sensitivity, *etc.*).

The theory used in the fitting assumes that the density perturbations caused by the driver laser are small compared to the ambient density, *i.e.*, that the density grating

behaves like an acoustic wave. This approximation becomes worse with increasing driver laser pulse energies. We see that there will be a trade-off between the favorable influence of a stronger signal and the negative effects of nonlinear behavior of the waves. We want to study this trade-off and find the point of best accuracy and lowest uncertainty.

B.2 Experimental Setup and Procedure

A frequency-doubled, Q-switched Nd:YAG laser (Continuum Surelite I10, max. 250 mJ, 10 Hz) was used as driver laser. An arrangement of beam splitters and mirrors on kinematic mounts split the beam in halves and focuses them path-length matched on a point in the sample volume where they intersect at an angle of 2.175°. The Gaussian beam half-width in the sample volume is 180 μm as determined in a calibration measurement. Test gas was unseeded atmospheric air. The pulse energy was adjusted by varying the flashlamp voltage. The driver laser pulse energy at different flashlamp voltages was measured using a laser power meter (Scientech Astral AA30). Pulse energies ranged from 17 mJ to 110 mJ. The data acquisition was triggered by a photo detector (Thorlabs DET210, 1 ns response time) which detected the driver laser pulse.

A CW Argon-ion laser (Spectra Physics Stabilite 2017, max. 1.3 W at 488 nm) provides the interrogation beam. The signal beam that is coherently scattered off the density grating is detected by a photomultiplier tube (Hamamatsu, H5783-03, 0.65 ns response time) and recorded as 2,048 discrete points with 12-bit resolution on a digital storage oscilloscope (Hewlett Packard Infinium, 500 MHz) from where it it transferred to a personal computer for storage and data analysis.

Sets of 1,000 single-shot measurements each were recorded for a range of driver laser pump energies. These measurements were taken in random order to eliminate systematic errors, *e.g.*, due to variations in ambient temperature. The continuous

interrogation beam was operated at full power. Only to reduce the signal level further beyond the minimum driver laser pulse energy, the interrogation beam power was also reduced until the LITA signal was only barely visible. A pulse energy that resulted in gas breakdowns in more than 10% of the shots was taken as the upper limit. Shots in which a gas breakdown had occurred were discarded from the subsequent data analysis. The system was calibrated using 32-shot averaged signals. The calibration resulted in a beam crossing angle of $\theta = 2.17°$, a driver beam half-width of $\omega = 189\ \mu$m, and an interrogation beam half-width of $\sigma = 330\ \mu$m. The sound speed and the thermal diffusivity were determined for every trace using Levenberg-Marquardt fitting[49] of a theoretical model to the experimental data.[29,36] The deviation of the average sound speed (thermal diffusivity) over a set from the true value is used as systematic error. The standard deviation of the sound speed (thermal diffusivity) over each set is taken as the measure for the uncertainty (statistical error).

B.3 Results

Fig. B.2 shows the signal-to-noise ratio (SNR) versus the square of the driver laser pulse energy (E_d) times the interrogation beam power (P_0). We define the SNR as the peak signal intensity of a given signal divided by the standard deviation of the noise in the pretrigger part of the signal. As the theory predicts[2] the signal intensity is approximately proportional to the interrogation beam power and scales with the square of the driver laser pulse energy. For high driver beam energies, the signals are stronger than predicted. The calibration measurement stands out because it was obtained by averaging over 32 individual effects, resulting in an approximately 6 times higher SNR at a given driver laser pulse energy. Deviations from the dashed line are most likely due to errors in the measurement of P_0 and E_d.

Fig. B.3 illustrates how, at high pump energies, a gas breakdown can occur in the sample volume. It plots the likelihood of observed gas breakdowns versus the driver

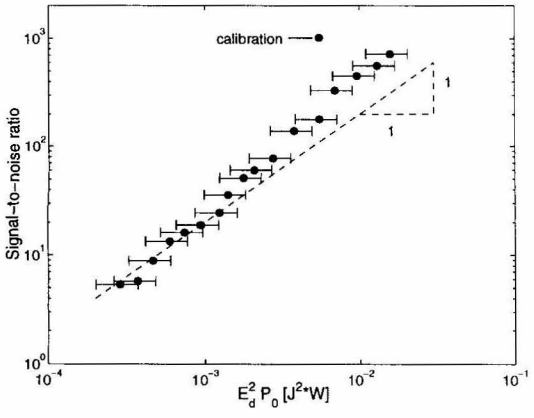

Figure B.2: Signal-noise-ratio *vs.* $E_d^2 P_0$ where E_d is the driver laser pulse energy and P_0 is the interrogation beam power.

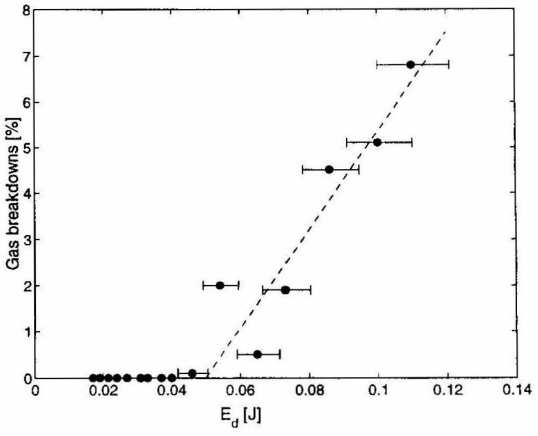

Figure B.3: Percentage of shots with gas breakdown in sample volume *vs.* driver laser pulse energy density.

laser energy in the sample volume. Below a critical pump energy no gas breakdowns are observed but their likelihood increases linearly for pump energies above that threshold. The relevant physical quantity for the gas breakdown is the electric field grating intensity. Hence the threshold value for the driver laser pump energy will be a function of the pulse duration, beam diameter and quality, beam crossing angle, and also of the test gas.

The accuracy and uncertainty of the sound speed measurements are plotted in Fig. B.4. Similarly, Fig. B.5 shows these results for the thermal diffusivity measurements. We see that the error for the sound speed measurements initially decreases with increasing SNR, but increases again after passing a minimum value of 0.03%. The uncertainty on the other hand does not have a minimum but decreases monotonically with increasing signal level. For low SNRs the measured sound speeds are too low and for SNRs above the optimum the measured sound speeds are too high. The error in the calibration signals is zero by construction.

The uncertainty for the thermal diffusivity measurements also decreases monotonically with increasing signal intensity. It is, however, approximately ten times higher than for the sound speed measurements at the same signal intensity. The trend for

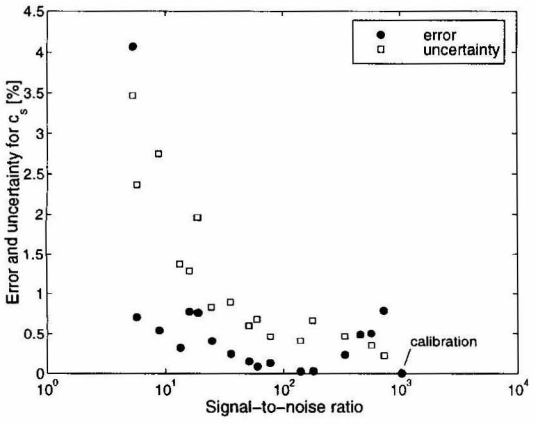

Figure B.4: Accuracy and uncertainty of the speed of sound *vs.* the signal-to-noise ratio.

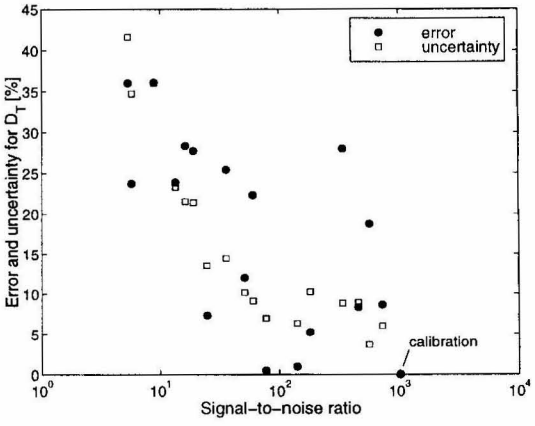

Figure B.5: Accuracy and uncertainty for the thermal diffusivity *vs.* the signal-to-noise ratio.

the accuracy for the thermal diffusivity is less pronounced but it appears to show the same behavior as the sound speed error with a minimum that coincides with the minimum for the sound speed measurements. The measured thermal diffusivity tends to be too high for SNRs above and below the optimum.

B.4 Discussion and Conclusions

The initial drop in the error and uncertainty with increasing laser power settings can be attributed to the increase in signal-to-noise ratio. The sign of the error will depend on the numerical scheme used for the data analysis. The increased error for high SNRs is due to high excitation beam pulse energies. The density waves for these conditions are out of the acoustic regime, which violates a basic assumption in the theoretical model that is used in the fitting routine. Instead, finite amplitude disturbances with changing wave shapes are created that travel faster than the local speed of sound of the undisturbed fluid,[80,81] resulting in measured speeds of sound that are above the correct value. This also causes the density perturbations (and hence the signal intensity) to be stronger than in the acoustic regime (Fig. B.2).

The optimum pulse energy in our case is only slightly below the critical value that

causes a gas breakdown. At this point we should have already left the acoustic regime but the benefits of the high SNR still prevails. This optimum point will depend on the experimental setup used. The errors for single-shot measurements at the optimum are 0.03% and 1% for the speed of sound and the thermal diffusivity, respectively. The uncertainties at this point of best accuracy are 0.5% and 10%, respectively.

Averaging over many driver laser shots offers the possibility of remaining in the acoustic limit while at the same time increasing the SNR (Fig. B.2). Similarly, high interrogation beam powers with lower driver laser pulse energies have to be preferred over the opposite case, *e.g.*, by using long-pulsed, high-intensity interrogation beams.[45] Also, photomultipliers with high quantum efficiencies will result in an increased signal level at a given driver laser pulse energy. These measures will move the point of minimal error towards lower driver laser energies.

The reason for the higher errors for the measurement of the thermal diffusivity are twofold. First, given a sufficient time resolution and number of cycles in the signal, we can measure a frequency much more precisely than a decay time constant. This is particularly true in the presence of noise. Secondly, to convert the measured Brillouin frequency into the speed of sound, only two parameters play a role: the driver beam wavelength and the driver beam crossing angle. The wavelength is fixed, constant, and precisely known. The bandwidth of the laser is negligible. The beam crossing angle is very stable. Depending on the optical setup, pointing instabilities of the driver laser will not change it. We can determine it in a calibration measurement within $\pm.01\%$. The conversion of the decay time constant into the thermal diffusivity requires the knowledge of the driver beam half-width and the interrogation beam half-width in the sample volume. Furthermore, the theory assumes Gaussian beam profiles and deviations therefrom will lead to errors. Each of these parameters carries an uncertainty and especially the beam geometries will vary due to thermal effects in the lasers.

The uncertainties are not influenced by the deviation of the theory from reality

as this represents a systematic rather than a statistical error. Hence, they decrease monotonically with increasing driver laser pulse energy (SNR). The results should also apply in similar fashion to the case of LITA using resonant pumping and to other techniques for the signal processing.[50,51]